

REPORT DOCUMENTATION PAGE

*Form Approved
OMB No. 0704-0188*

The public reporting burden for this collection of information is estimated to average 1 hour per response, including the time for reviewing instructions, searching existing data sources, gathering and maintaining the data needed, and completing and reviewing the collection of information. Send comments regarding this burden estimate or any other aspect of this collection of information, including suggestions for reducing the burden, to Department of Defense, Washington Headquarters Services, Directorate for Information Operations and Reports (0704-0188), 1215 Jefferson Davis Highway, Suite 1204, Arlington, VA 22202-4302. Respondents should be aware that notwithstanding any other provision of law, no person shall be subject to any penalty for failing to comply with a collection of information if it does not display a currently valid OMB control number.

PLEASE DO NOT RETURN YOUR FORM TO THE ABOVE ADDRESS.

1. REPORT DATE (DD-MM-YYYY) 14-11-2011	2. REPORT TYPE Final Report	3. DATES COVERED (From - To) 1 Dec 2009 to 30 Sep 2011
--	---------------------------------------	--

4. TITLE AND SUBTITLE Final Report: Analysis of Coherent Microwave Data Collected on the Ocean over Two Decades	5a. CONTRACT NUMBER
	5b. GRANT NUMBER N00014-10-1-0318
	5c. PROGRAM ELEMENT NUMBER

6. AUTHOR(S) William Plant, Gordon Farquharson, William Keller, Ken Hayes, Gene Chatham, Patricio Catalan, Merrick Haller, Rober Holman	5d. PROJECT NUMBER
	5e. TASK NUMBER
	5f. WORK UNIT NUMBER

7. PERFORMING ORGANIZATION NAME(S) AND ADDRESS(ES) Applied Physics Laboratory - University of Washington 1013 NE 40th Street Seattle, WA 98105-6698	8. PERFORMING ORGANIZATION REPORT NUMBER
---	---

9. SPONSORING/MONITORING AGENCY NAME(S) AND ADDRESS(ES) Office of Naval Research (ONR 322) 875 North Randolph Street Arlington, VA 22203-1995	10. SPONSOR/MONITOR'S ACRONYM(S) ONR
	11. SPONSOR/MONITOR'S REPORT NUMBER(S)

12. DISTRIBUTION/AVAILABILITY STATEMENT
Approved for Public Release; Distribution is Unlimited

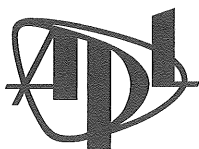
13. SUPPLEMENTARY NOTES
None

14. ABSTRACT
The objective of this project was to perform further analysis of data sets that had been collected over the past two decades. To this end the following data sets were further analyzed: the Airship data sets of 1993 and 1995, the SHOWEX data set of 1999, the NLIWI data set of 2005-2007, the Philippine data set of 2007, the Duck data set of 2008, and the Ship Guidance data set of 2008. Findings include, but are not limited to, the following: 1) VV backscatter agrees well with the multiscale composite surface model, 2) Breaking waves contribute more to HH than VV backscatter and can cause cross sections at HH to exceed those at VV in disagreement with composite surface theory, 3) Shadowing is not a factor in low-grazing-angle backscatter from the ocean, especially at VV polarization, and 4) Linear features in wavenumber-frequency spectra of ocean backscatter are primarily due to short gravity waves breaking at maxima of dominant-wave interference patterns

15. SUBJECT TERMS
sea clutter, microwave backscatter from the ocean, shadowing, wave breaking, model functions, internal waves

16. SECURITY CLASSIFICATION OF:			17. LIMITATION OF ABSTRACT UU	18. NUMBER OF PAGES 84	19a. NAME OF RESPONSIBLE PERSON William Plant
a. REPORT U	b. ABSTRACT U	c. THIS PAGE U			19b. TELEPHONE NUMBER (Include area code) 206-543-7836

Reset



Applied Physics Laboratory

University of Washington

1013 NE 40th Street
Box 355640
Seattle, WA 98105-6698

206-543-1300
FAX 206-543-6785
www.apl.washington.edu

14 November 2011

To: Dr. Scott Harper (ONR 322)
Office of Naval Research
875 North Randolph Street
Arlington, VA 22203-1995

From: Dr. William J. Plant

- Enclosures:
- (1) Plant, W. J., W. C. Keller, K. Hayes and G. Chatham, Normalized radar cross section of the sea for backscatter: 1. Mean levels, *J. of Geophysical Research*, **115**, C09032, doi:10.1029/2009JC006078
 - (2) Plant, W. J., W. C. Keller, K. Hayes, G. Chatham, and N. Lederer, Normalized radar cross section of the sea for backscatter: 2. Modulation by internal waves, *J. Geophysical Research*, **115**, C09033, doi:10.1029/2009JC006079
 - (3) P. A. Catalan, M. C. Haller, R. A. Holman, W. J. Plant, Optical and Microwave Detection of Wave Breaking in the Surf Zone, *IEEE Transaction on Geoscience and Remote Sensing*, **49**, doi:10.1109/TGRS.2010.2095864
 - (4) Plant, W. J., W. C. Keller, K. Hayes, G. Chatham, Characteristics of Internal Waves in the South China Sea Observed by a Shipboard Coherent Radar, *IEEE Journal of Oceanic Engineering*, **36**, doi: 10.1109/JOE:2011.2133030
 - (5) W. J. Plant, G. Farquharson, Wave Shadowing and Modulation of Microwave Backscatter from the Ocean, September 26, 2011.
 - (6) W. J. Plant, G. Farquharson, Origins of Features in Wavenumber-Frequency Spectra of Space-Time Images of the Ocean

Subject: FINAL REPORT: ONR GRANT N00014-10-1-0318

Enclosures (1) through (4) are four publications that resulted from the work funded under Office of Naval Research (ONR) Grant N00014-10-1-0318. Enclosures (5) and (6) are manuscripts that discuss the work under the ONR grant. They are in the process of being submitted for publication. Please accept enclosures (1) through (6) as the final report for ONR Grant N00014-10-1-0318.


William Plant

WJP:kaw

cc: ONR Administrative Grants Office, Seattle (without enclosure)
Director, Naval Research Laboratory (Code 5596) (w/ SF298)
Defense Technical Information Center (w/ SF298)
Office of Sponsored Programs, University of Washington (without enclosure)

Normalized radar cross section of the sea for backscatter:

1. Mean levels

William J. Plant,¹ William C. Keller,¹ Kenneth Hayes,¹ and Gene Chatham¹

Received 21 December 2009; revised 30 April 2010; accepted 25 May 2010; published 30 September 2010.

[1] The normalized radar cross section of the sea for backscatter, σ_o , is investigated for incidence angles between 0° and 89° using data collected over more than two decades. The most recent measurements were made from several ships using a coherent, dual-polarized, X band radar. These measurements show that vertically polarized transmit and receive signals, $\sigma_o(VV)$, at high incidence angles exhibit wind speed and azimuth angle dependence similar to those at lower incidence angles. They are nearly as large looking downwind as they are looking upwind and minimize near the crosswind direction. Horizontally polarized transmit and receive signals, $\sigma_o(HH)$, behave differently at high incidence angles. They are largest looking upwind and smallest looking downwind. Fits of the multiscale model of microwave backscatter from the ocean to these data along with data collected previously at lower incidence angles show that over the whole range of incidence angles from 0° to 89° , $\sigma_o(VV)$ is explained by the model, while measured $\sigma_o(HH)$ values are generally higher than the model predicts at incidence angles above about 45° . Thus scattering phenomena exist on the ocean surface that affect HH backscatter very strongly at the higher incidence angles while impacting VV-polarized backscatter only slightly. This conclusion is strengthened by our observation of high-incidence-angle backscatter from the ocean where mean $\sigma_o(HH)$ exceeds mean $\sigma_o(VV)$ by as much as 15 dB. We examine phenomena that might account for this behavior and suggest that multipath dihedral-type features are likely to be important scatterers since they produce large $\sigma_o(HH)/\sigma_o(VV)$ owing to Brewster damping of the first VV bounce.

Citation: Plant, W. J., W. C. Keller, K. Hayes, and G. Chatham (2010), Normalized radar cross section of the sea for backscatter: 1. Mean levels, *J. Geophys. Res.*, 115, C09032, doi:10.1029/2009JC006078.

1. Introduction

[2] While the normalized radar cross section (NRCS) of the sea, σ_o , for cross polarization can be illuminating, for instance, in detecting multiple scattering events, it is generally much smaller than copolarized cross sections [Wiltse *et al.*, 1957; Kalmykov and Pustovoytenko, 1976; Lee *et al.*, 1999]. For this reason, σ_o values obtained with the electric field of the radiation either vertical $\sigma_o(VV)$ or horizontal $\sigma_o(HH)$ on both transmission and reception are more useful modes and ones that have been studied much more than cross-polarized cross sections. In this series of two papers, we report our work on the copolarized normalized radar cross section of the sea for backscatter, σ_o . The present paper, part 1, concentrates on the behavior of the mean σ_o as a function of wind speed, incidence angle, and polarization. Part 2 [Plant *et al.*, 2010] documents our recent measurements on σ_o modulated by surface currents set up by internal waves in the ocean.

[3] Historically $\sigma_o(VV)$ has been known to be rather well explained by Bragg scattering augmented by a composite, or two-scale, sea surface over the range of incidence angles from approximately 20° to 60° and probably at even higher incidence angles, into the so-called low-grazing angle regime [Wright, 1968; Bass *et al.*, 1968]. $\sigma_o(HH)$, on the other hand, has been, and continues to be, more mysterious. It has appeared to be fairly well predicted by Bragg/composite-surface scattering from 20° to 45° incidence but exceeds the predictions at larger incidence angles. At lower incidence angles, specular scattering has been used to account for both $\sigma_o(VV)$ and $\sigma_o(HH)$, but requires an “effective” reflection coefficient. Matching specular and Bragg scattering near 20° incidence is a nontrivial exercise.

[4] In 2002, Plant developed a multiscale model and showed that by adding a third scale of the sea surface and using a Kirchhoff integral approach, which is well approximated by Bragg scattering for low wind speeds or moderate to large incidence angles, predictions in agreement with $\sigma_o(VV)$ and $\sigma_o(HH)$ measurements could be produced over the incidence angle range 0° to about 45° without invoking an arbitrary effective reflection coefficient [Plant, 2002]. Applying the theory beyond this incidence angle range was discouraged in that paper, however, because multiple

¹Applied Physics Laboratory, University of Washington, Seattle, Washington, USA.

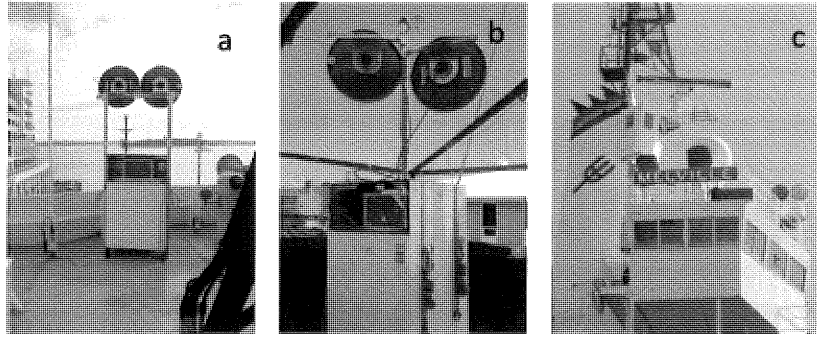


Figure 1. RiverRad mounted on the ships: (a) R/V *Revelle* in 2005, (b) R/V *Endeavor* in 2006, and (c) R/V *Melville* in 2007.

scattering and breaking waves are not included in the model.

[5] In this paper we show that this multiscale model in fact explains $\sigma_o(\text{VV})$ over the entire range of incidence angles from 0° to 89° if shadowing is included. $\sigma_o(\text{HH})$ remains unexplained by the model beyond an incidence angle of about 45° , however. We will investigate possible reasons for this behavior of $\sigma_o(\text{HH})$, including backscattering from spray and from surface features caused by breaking waves.

2. Low-Grazing Angle Backscatter From the Ocean

[6] An X band Doppler radar was operated on the R/V *Revelle* in the South China Sea in 2005, on the R/V *Endeavor* off the New Jersey coast in 2006, on the R/V *Melville* in the Philippine Sea in 2007. The radar transmitted a peak power of 10 W and used a pulse width of 15 m in 2005, 3.75 m in 2006, and 30 m in 2007. The radar is the RiverRad system that was developed for river surface velocity measurements and is described more fully by *Plant et al.* [2005]. It is shown mounted on the three ships in Figure 1.

[7] In all three years, we calibrated the sea return against that from a corner reflector so that fully calibrated normalized radar cross sections, σ_o , could be obtained. In 2005, only VV-polarized backscatter was obtained owing to a switch failure, and the antennas were fixed looking nearly toward the bow of the ship. In 2006, both HH and VV backscatter were collected. The antennas scanned through approximately 80° and were directed 35° apart in azimuth. In 2007, the antennas were again fixed but this time looking perpendicular to the heading of the ship; both HH and VV backscatter were collected. On all cruises, backscatter was collected both from seas disturbed only by the wind and from seas where internal waves were present.

[8] Figure 2 shows the angular dependence of $\sigma_o(\text{VV})$ observed in 2005 at an 89° incidence angle and at various wind speeds in the absence of internal waves. Note that $\sigma_o(\text{VV})$ exhibits the same second-harmonic dependence on azimuth angle that it does at lower incidence angles. This is not the case for the horizontally polarized cross section, $\sigma_o(\text{HH})$ shown in Figure 3 at nearly the same incidence angle. Here both $\sigma_o(\text{VV})$ and $\sigma_o(\text{HH})$ are shown as determined from the measurements of 2006. $\sigma_o(\text{HH})$ maximizes when the antenna looks into the wind and minimizes in the

opposite direction. These results agree with the uncalibrated, nearshore measurements of *Trizna and Carlson* [1996].

[9] Figures 4 and 5 show the wind speed dependences of these data and compare them to simple Bragg scattering predictions using the spectrum of *Elfouhaily et al.* [1997]. Clearly, the Bragg predictions are much too low and their increase with wind speed is too small. In fact, Bragg predictions for $\sigma_o(\text{HH})$ are below the bottom of the plot in Figure 5b.

[10] This underprediction can be overcome for $\sigma_o(\text{VV})$ by resorting to the multiscale model [*Plant, 2002*]. This model extended the standard composite surface model to include effects of waves that were intermediate between Bragg scattering waves and long, modulating waves. This model used results of the small slope approximation [*Voronovich, 1985*] and the integral expansion method [*Fung et al., 1992*] for backscatter to combine specular and Bragg scattering into a single Kirchhoff integral that covered incidence angles from nadir to midrange. The predictions of this model were shown to agree well with Ku band data obtained on an airship and with other data sets at C and Ka bands as

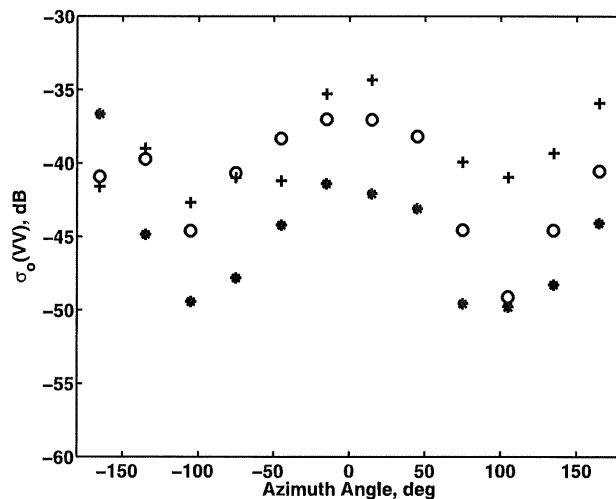


Figure 2. Angular dependence of $\sigma_o(\text{VV})$ at X band and an incidence angle of $89^\circ \pm 0.25^\circ$. These 2005 results are for the ocean surface disturbed only by wind. Symbols are for various wind speeds: asterisks, 4 m/s; circles, 6 m/s; pluses, 8 m/s.

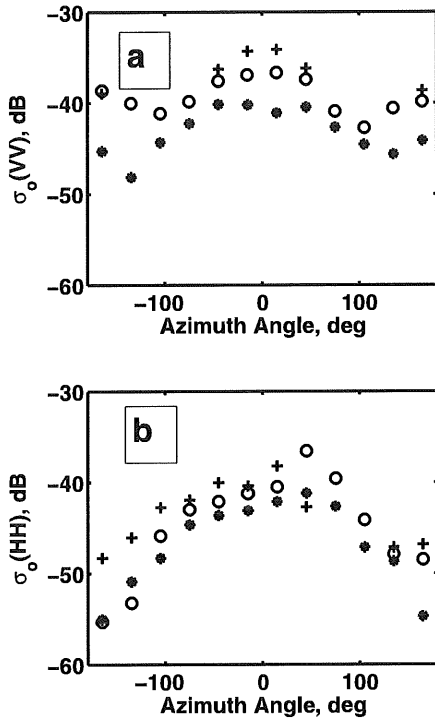


Figure 3. Angular dependence of the normalized radar cross section (NRCS) measured in 2006 for a sea surface disturbed only by wind. The incidence angle is $88.3^\circ \pm 0.1^\circ$: (a) angular dependence of $\sigma_0(VV)$ and (b) angular dependence of $\sigma_0(HH)$. Symbols are the same as those in Figure 2.

well as Ku band at nadir incidence. These comparisons, however, were only done for incidence angles up to 50° because breaking waves and spray were not included in the model, making it questionable above this incidence angle.

[11] The improved fit using this model is demonstrated in Figure 6, where the left plots show $\sigma_0(VV)$ versus wind speed for upwind, downwind, and crosswind looks. The squares in Figure 6 are results of the multiscale model modified to include simple geometric shadowing. Intermediate-scale facets were not included in the calculations if they could not be seen by the antenna. Interestingly, Bragg scattering predictions can also fit the data if a mean tilt of the illuminated parts of the surface given by $U/4$ is assumed, where tilt is in degrees and U is in m/s. This yields the lines in Figure 6.

[12] Figure 6 also shows similar data and models for $\sigma_0(HH)$ in the right plots. Here the measured values are much larger than either those predicted by the multiscale model or by tilted Bragg. This is true even when the antenna is directed down wind and wave. Since breaking wave effects are generally assumed to have little effect on backscatter with the antenna directed nearly down wave, we interpret these results to mean that a scattering mechanism exists at these grazing angles other than multiple scattering from breaking waves that affects $\sigma_0(HH)$ much more than $\sigma_0(VV)$. This is reasonable considering the much higher level of $\sigma_0(VV)$ shown in the downwind part of Figures 3 and 5. Thus we need an increase in the $\sigma_0(HH)$ values predicted by the multiscale model of about 10 dB in the

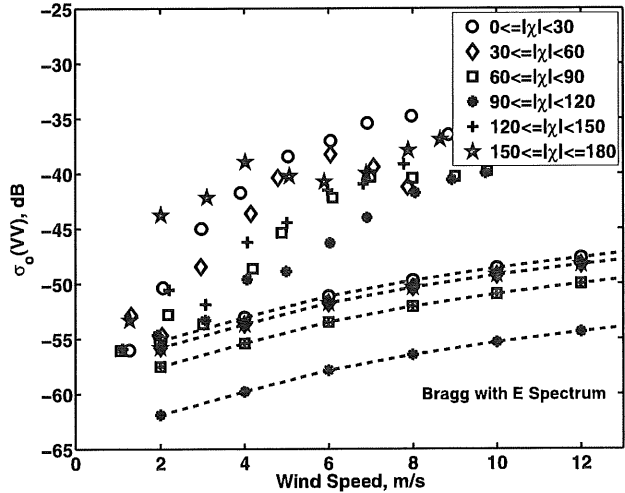


Figure 4. Wind speed dependence of $\sigma_0(VV)$ at various azimuth angles from the wind for the data of 2005. The χ is the angle between the antenna look direction and the direction from which the wind comes. Lines show simple Bragg scattering predictions using the wind wave spectrum of *Elfouhaily et al.* [1997].

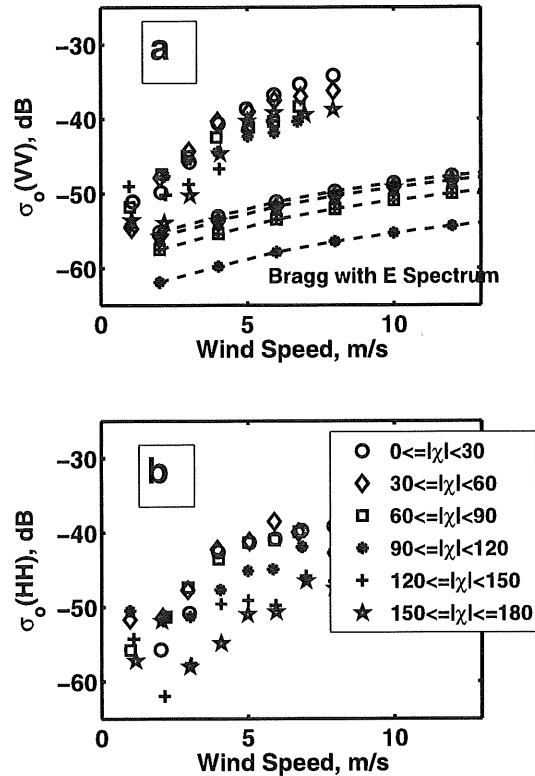


Figure 5. Wind speed dependence of σ_0 at various azimuth angles from the wind for the data of 2006: (a) $\sigma_0(VV)$ and (b) $\sigma_0(HH)$. Lines show simple Bragg scattering predictions for $\sigma_0(VV)$ using the wind wave spectrum of *Elfouhaily et al.* [1997]; $\sigma_0(HH)$ predicted by Bragg scattering is below the bottom of the graph in Figure 5b.

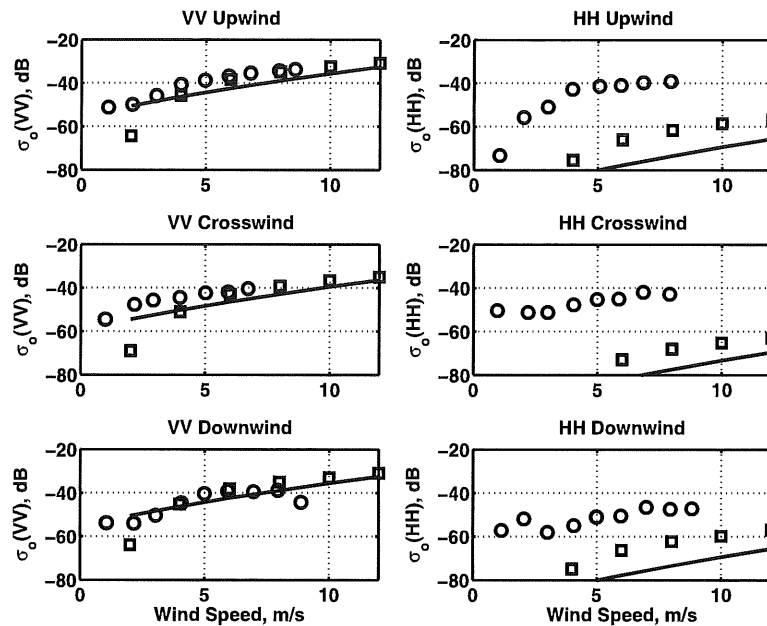


Figure 6. Fit of the multiscale model (squares) to the data of 2006 for upwind looks (circles). The lines are Bragg scattering predictions if the local grazing angle in degrees is larger than the nominal one by $U/4$, where U is wind speed in m/s. The incidence angle is 88° .

downwind direction and about 20 dB in the upwind direction in order to explain the data.

3. Fits to the Multiscale Model Over All Incidence Angles

[13] To check the predictions of the multiscale model further, we compared it with lower incidence data in addition to these high-incidence-angle measurements. Over the last two decades, we have collected a variety of $\sigma_0(\text{VV})$ and $\sigma_0(\text{HH})$ data at 14.0 GHz (Ku band) and 9.36 GHz (X band). These data were collected at many different incidence angles, wind speeds, and azimuth angles from platforms as varied as research platforms, airships, airplanes, and ships [Plant, 1997; Plant et al., 1998, 2005].

[14] Figures 7–10 show the comparison out to incidence angles higher than those shown by Plant [2002]. The predictions of the multiscale model for $\sigma_0(\text{VV})$ and $\sigma_0(\text{HH})$ are compared with the following data sets: Ku band collected on the German Research Platform Nordsee [Plant, 1997, 2003b], on the airship off the coast of Oregon [Plant et al., 1998], and the TOPEX/Poseidon satellite altimeter [Hwang et al., 1998]; X band data from a Twin Otter aircraft flown off the coast of North Carolina [Plant et al., 2005] and the ship data discussed above. We ran the model with various ocean wave spectra and for both X and Ku band. Figures 7–10 show the results for the spectrum that Plant [2002] calls the D-spectrum. Comparisons of predictions with other spectral models can change the model predictions somewhat.

[15] Figures 7–10 show predictions of the multiscale model at both Ku and X bands. They are very similar above the lowest wind speed, differing by 3 dB at most for a 4 m/s wind speed. The data at wind speeds of 8 m/s (Figure 8), 12 m/s (Figure 9) and 16 m/s (Figure 10) all indicate that the model predicts $\sigma_0(\text{VV})$ rather well over the whole range of

incidence angles from 0° to 89° for upwind, crosswind, and downwind antenna look directions. At 4 m/s (Figure 7), the fit is less good in places but wave spectra at this wind speed can vary widely owing to wind variability [Plant, 2000]. The fit is not as good for $\sigma_0(\text{HH})$. For this polarization, the predictions appear to be accurate up to an incidence angle of about 45° but fall significantly below the data for higher incidence angles. This is true for all three antenna look directions. In section 5, we will discuss possible reasons that the multiscale model might underpredict $\sigma_0(\text{HH})$ at high incidence angles.

4. Anomalous Low-Grazing Angle Backscatter From the Ocean

[16] Part 2 [Plant et al., 2010] shows that internal waves can sometimes generate surface conditions for which $\sigma_0(\text{HH}) > \sigma_0(\text{VV})$, which as shown above does not normally occur for ocean backscatter on large scales. However, we have observed an occurrence of mean $\sigma_0(\text{HH})$ larger than mean $\sigma_0(\text{VV})$ in 2007 when the RiverRad operated from the R/V Melville around the Philippine Islands. In the images collected, we observed many regions of high oceanic backscatter of unknown cause. An example is shown in Figure 11. A total of 15 images of similar quality were collected. Figure 11 shows $\sigma_0(\text{HH})$ and $\sigma_0(\text{VV})$ in dB with associated scatterer velocities in m/s. Also shown in Figure 11e are the wind speed, wind direction, ship speed, and ship heading. The antennas looked broadside to the ship on the starboard side and were 16.5 m above the water. The high cross section and velocity features cover more than 2 km in range and lasts for nearly 5 min as the ship goes by at 6 m/s. Thus the features are also about 2 km in the azimuth direction. $\sigma_0(\text{HH})$ is 5 to 15 dB larger than $\sigma_0(\text{VV})$ over most of this region.

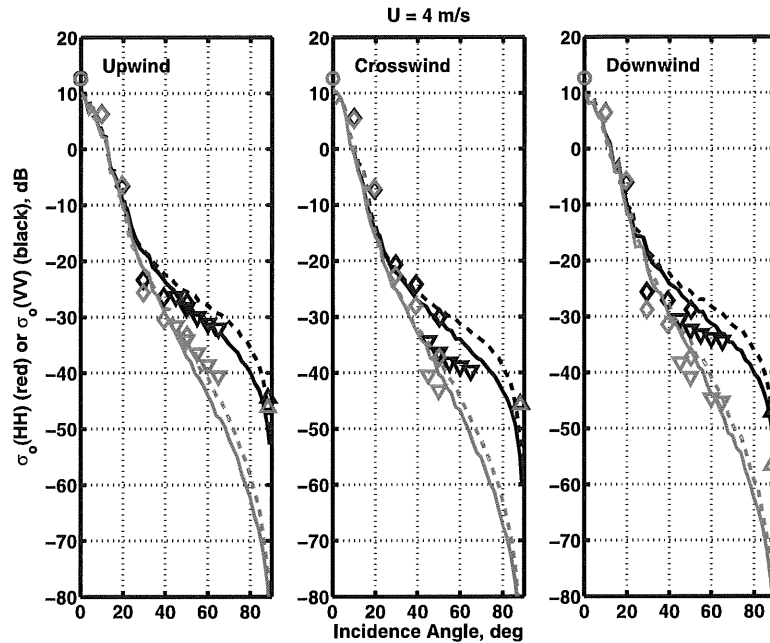


Figure 7. Comparison of predictions of the multiscale model with data for a wind speed of 4 m/s. The D-spectrum of *Plant* [2002] was used in the calculation. Solid lines are predictions at Ku band, while dashed lines are predictions at X band. Red always indicates $\sigma_0(\text{HH})$, while black indicates $\sigma_0(\text{VV})$. Symbols for the data are as follows: circles, Ku band data from the TOPEX/POSEIDEN altimeter; diamonds, Ku band from the airship [*Plant et al.*, 1998]; upside-down triangles, X band from the airplane [*Plant et al.*, 2005]; triangles, X band data from the ships discussed above.

[17] The large regions covered by this anomalous backscatter lead us to believe that it is not of man-made origin, for instance interference from other marine radars. This belief is strengthened by the fact that most of the high-

backscatter regions occur near the ship at the same time that shifts in wind speed or direction were measured by the ship's anemometer. We cannot rule out the involvement of rainfall in the occurrence of these features since precipita-

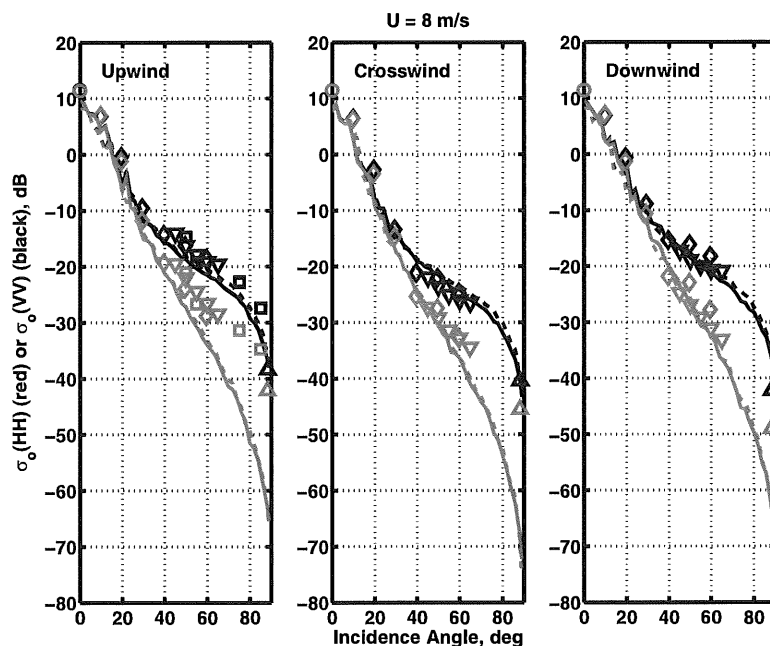


Figure 8. Same as Figure 7 but for a wind speed of 8 m/s. The squares are Ku band data from the Nordsee platform [*Plant*, 1997, 2003b].

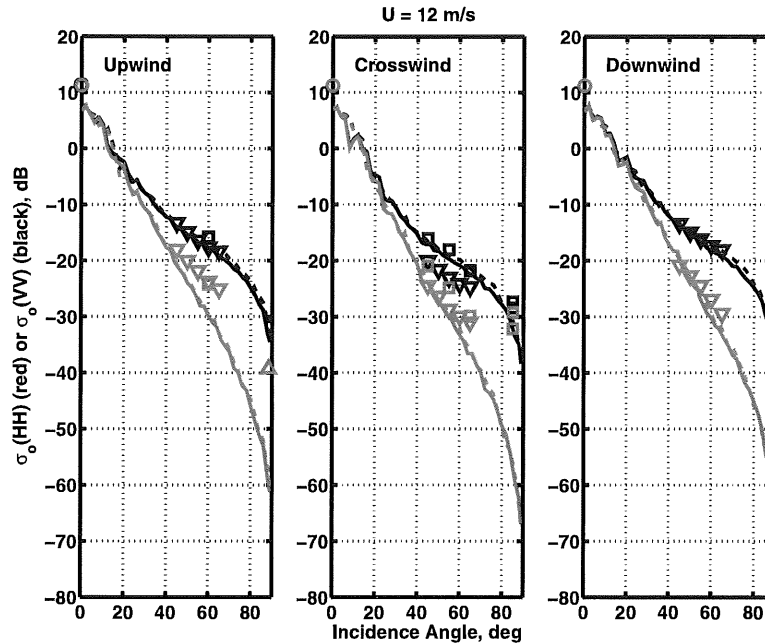


Figure 9. Same as Figures 7 and 8 but for a wind speed of 12 m/s.

tion measurements on the ship were not adequate to examine this possibility. In any case, it seems obvious that these features are a natural phenomenon associated with low-grazing angle backscatter from the sea surface.

[18] To document this further, and to assure that these results are not a product of faulty radar calibration, we show time series of $\sigma_o(\text{HH})$ and $\sigma_o(\text{VV})$ at an incidence angle of 88.75° for two different time periods near the Philippine

Islands in Figure 12. This incidence angle was chosen because it corresponds to the center of the beam from the 2 foot diameter parabolic antennas that were used to collect these data. This angle therefore corresponds to the largest signal-to-noise ratio. Figures 12a and 12c correspond to the image of Figure 11, while Figures 12b and 12d were obtained well away from any such anomalous backscattering features. Clearly, $\sigma_o(\text{HH})$ is smaller than $\sigma_o(\text{VV})$ when

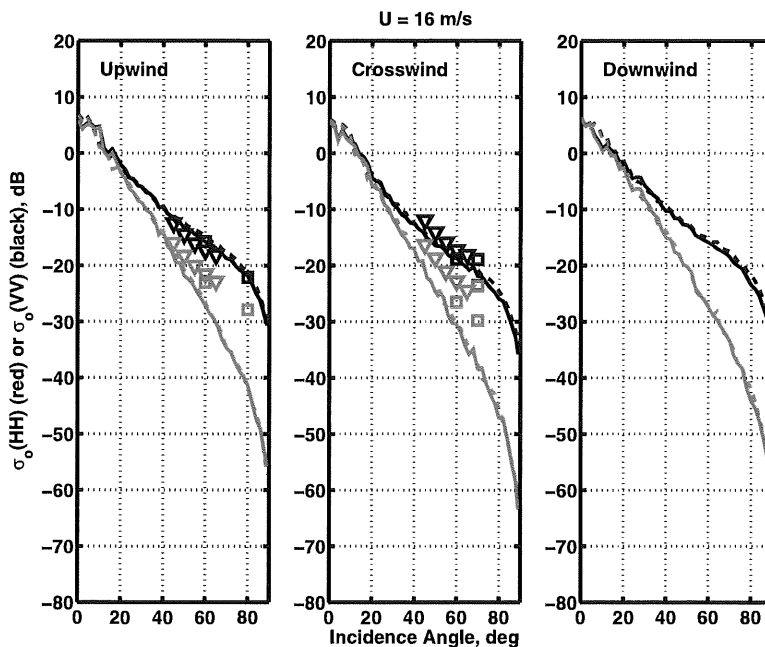


Figure 10. Same as Figures 7 and 8 but for a wind speed of 16 m/s.

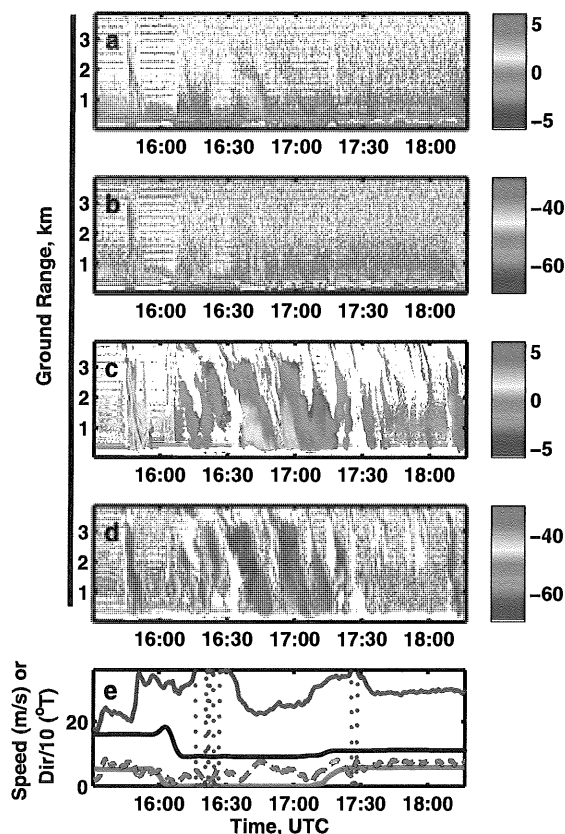


Figure 11. Space-time images of $\sigma_o(\text{HH})$ and $\sigma_o(\text{VV})$ along with their associated velocities, wind, and ship parameters collected on 7 June 2009. (a) Scatterer velocities from VV backscatter in m/s. (b) $\sigma_o(\text{VV})$ in decibels. (c) Scatterer velocities from HH backscatter in m/s. (d) $\sigma_o(\text{HH})$ in decibels. Note the dramatically larger cross section and velocities for HH polarization inside the pronounced features. (e) Ship and wind parameters. Red is ship speed, black is ship heading divided by 10, green is wind speed, and blue is wind direction divided by 10. White areas in Figures 11a–11d indicate that the signal was too low to calculate σ_o or velocity.

the ocean surface is disturbed only by the wind but becomes larger than $\sigma_o(\text{VV})$ in the anomalous region.

[19] Bragg scattering cannot account for the anomalous features since it always yields $\sigma_o(\text{VV})$ greater than $\sigma_o(\text{HH})$ on average. In section 5, we explore some ideas that have been put forward to explain these non-Bragg features and take the first steps toward a method for including the most important ones in the model.

5. Other Scattering Mechanisms

[20] The fact that the multiscale model does not predict the large values of $\sigma_o(\text{HH})$ that are observed at incidence angles above 45° in all look direction suggests that scattering processes other than the Bragg scattering processes described by the standard composite surface theory may be occurring at high incidence angles. This has been noted many times in the past by a variety of authors (see

Churyumov *et al.* [2002], for instance). In fact, the data suggest that more than one of these nonstandard scattering mechanisms may be at work. As discussed further below, many of the non-Bragg processes that have been proposed over the years involve breaking waves; Bragg scattering from bound, tilted waves proposed by Plant [1997] also require breaking, or at least crumpling, waves. However, the fact that $\sigma_o(\text{HH})$ is higher than predicted in the downwind look direction (see Figures 6–8) is difficult to explain using only a mechanism tied to breaking waves. Such wave-breaking regions exist primarily near wave crests or on the front face of waves and their effects should be much weaker when the antenna is looking downwind, especially at very high incidence angles.

[21] Many possibilities for the additional backscatter at HH polarization have been proposed over the years. These include bound, tilted waves due to the breaking of short gravity waves, specular backscatter, wedges, spray, and multipath scattering from steep features.

[22] Plant [1997] proposed that some features of HH backscatter at incidence angles greater than 45° can be explained by Bragg scattering but from the rough patches produced by breaking short gravity waves that travel with the gravity waves rather than from freely propagating centimetric surface waves. In particular, observations of larger Doppler shifts in HH than in VV backscatter and of low coherence between HH Doppler shifts and dominant ocean wave orbital velocities when looking into the wind at large incidence angles can be explained. The patches are assumed to be strongly tilted toward the antenna under these conditions and this tilt increases HH Bragg scattering more than VV. The existence of bound, tilted waves in wind-generated and breaking wave systems has been well substantiated by wave tank experiments [Plant *et al.*, 1999a, 1999b, 2004; Rozenberg *et al.*, 1999; Lee *et al.*, 1999]. The skewness of sea surface slope probability distributions can also be explained on the basis of such waves [Plant, 2003a]. Nevertheless, bound, tilted waves do not seem to account for all of the excess backscatter (over standard Bragg/composite) for HH polarization at high incidence angles. Bragg scattering from bound, tilted waves cannot account for large $\sigma_o(\text{HH})/\sigma_o(\text{VV})$ ratios except momentarily [Plant, 2003b]. It also cannot account for $\sigma_o(\text{HH})$ being too large in the downwind look direction. Furthermore, a limit exists on how strong the scattering from bound, tilted waves can be since their effects are not observed in VV backscatter. This limit is sufficiently low to ensure that bound, tilted waves cannot explain all of the excess backscatter even in the upwind direction.

[23] Specular backscatter has frequently been invoked as a means for increasing the $\sigma_o(\text{HH})/\sigma_o(\text{VV})$ polarization ratio at large incidence angles [Chubb *et al.*, 1999; Kudryavtsev *et al.*, 2005]. While the assumption that sufficient specular points exist nearly perpendicular to the high-incidence-angle incident field to produce significant backscatter is arguable, this mechanism clearly cannot produce polarization ratios much larger than one, as observed above.

[24] Wedge scattering, which is scattering from sharp crests of significant extent in the horizontal, has been suggested as a means of increasing high-incidence-angle backscatter at HH polarization [Lyzenga *et al.*, 1983]. Previous work on backscatter from these structures had been

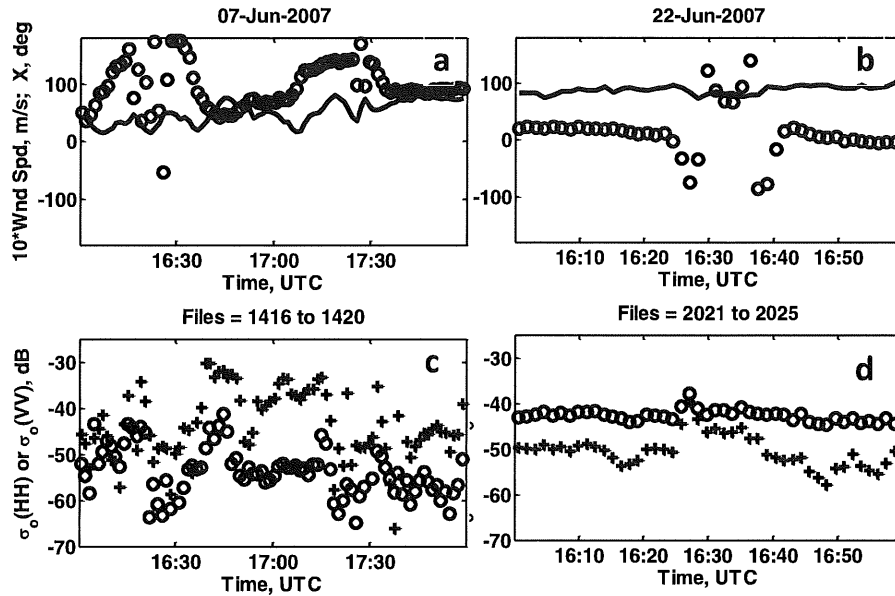


Figure 12. Documentation of variable polarization ratios at an incidence angle of $88.75^\circ \pm 0.25^\circ$. (a, b) Solid line is 10 times the wind speed; circles are azimuth angle with respect to the direction from which the wind comes, χ . (c, d) Measured $\sigma_0(\text{HH})$ (pluses) and $\sigma_0(\text{VV})$ (circles) at the times of Figures 12a and 12b. The data in Figures 12a and 12c were collected at the same time as those in Figure 11.

contradictory. *Kalmykov and Pustovoytenko* [1976] suggested that it produced a polarization ratio greater than one at high incidence angles, while *Lewis and Olin* [1980] said it produced polarization ratios less than one. *Lyzenga et al.* [1983] showed that the polarization ratio was above one at incidence angles lower than a level set by the wedge angle and below one for higher incidence angles. For a 195° wedge angle, the crossing point was at about 82° incidence. Thus, while these structures may contribute somewhat to the backscatter, they cannot explain our observations of $\sigma_0(\text{HH}) / \sigma_0(\text{VV}) > 1$ at very high incidence angles.

[25] One exception to this statement is for incident radiation that strikes the wedge from above, that is, perpendicular to its base. This configuration is most likely to occur for high incidence angles when the “wedge” is the tip of a plunging breaking wave. *Churyumov et al.* [2002] showed that under these conditions the backscatter may have a polarization ratio above one. Three-dimensional numerical calculations by *Li and West* [2006] indicated the same phenomenon. The density of plunging breakers on the open ocean is likely to be rather low under normal conditions, however, so this mechanism may contribute relatively little to the mean backscatter in most cases.

[26] Spray above the water surface that is produced by actively breaking waves is another possible source of backscatter. Bounces from the surface of the water to the spray droplets will serve to augment the direct backscatter from the drops. Both this and possible flattening of the drops could produce HH backscatter that is larger than VV backscatter. However, *Plant* [2003b] showed that if spray is to account for the increased backscatter at HH polarization and high incidence angles, it must increase with wind speed

much more slowly than is generally observed. On the other hand, *Plant et al.* [2006] later showed that while large Doppler shifts due to backscatter from spray can be observed in a wind-wave tank, the spray responsible for the backscatter is located too close to the surface to be measured with in situ instruments. Thus the question of the role of spray in high-incidence backscatter is still open.

[27] Multipath scattering from steep surface features is perhaps the most likely source of the observed high-polarization ratio. Backscatter from breaking waves has been studied for many years and clearly shows that $\sigma_0(\text{HH})$ can exceed $\sigma_0(\text{VV})$ during breaking [*Lee et al.*, 1998; *Fuchs et al.*, 1999; *Sletten et al.*, 2003]. Most researchers have invoked some type of multiple scattering phenomena to explain this behavior [*Wetzel*, 1986; *Trizna*, 1997; *Holliday et al.*, 1998; *West*, 1999, 2002; *Lee et al.*, 1997, 1998]. *Wetzel* [1986] seems to have been the first to suggest the importance of this type of scattering. He proposed that the backscatter resulted from a bounce of the incoming ray from the water surface in front of a borelike front resulting from breaking. He modeled this as a quarter cylinder rising out of a flat, tilted sea surface and multiplied the standard cylinder cross section by a “proximity factor” to account for the presence of the flat surface. His results, while including Brewster damping of vertically polarized rays at the first bounce, indicate that VV backscatter will be stronger than HH backscatter for large incidence angles.

[28] *Lee et al.* [1997] and *Trizna* [1997] both proposed that the structures producing backscatter during breaking could be better modeled by a dihedral in which two water surfaces at right angles produce a double-bounce backscatter. Both suggested that Brewster damping of VV-

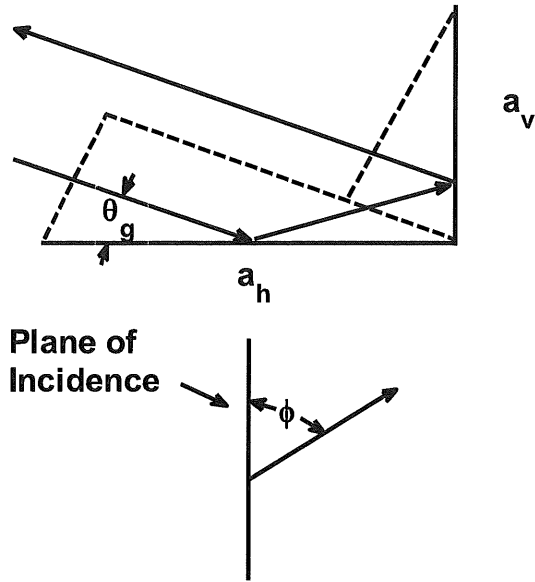


Figure 13. Diagram of the dihedral scattering geometry. Sides of the dihedral are a_v and a_h , θ_g is the grazing angle, and the electric field \mathbf{E} makes an angle ϕ with the plane of incidence.

polarized incident radiation at the initial bounce would reduce its backscatter level compared to that of HH polarization. *Lee et al.* [1997] carried out experiments that verified this. *Trizna* [1997] concentrated on the interference of the ray directly incident on the vertical surface and that reflected from the horizontal surface. Since both of these rays cannot be reflected to the antenna simultaneously, however, it is unclear why this interference is a concern.

[29] While dihedrals are clearly idealized scattering structures, numerical studies show that similar multiple scattering phenomena occur for a breaking wave at and immediately after breaking [*West*, 1999, 2002; *Fuchs et al.*, 1999]. These studies also show that the exact nature of this multiple scattering depends critically on the shape of the surface [*Lee et al.*, 1998; *Fuchs et al.*, 1999; *West*, 2002; *Sletten et al.*, 2003]. Furthermore, multiple scattering also occurs for strong breaking in the very turbulent region produced by breaking, as evidenced by the cross-polarized signal and $\sigma_o(\text{HH})$ greater than $\sigma_o(\text{VV})$ [*Lee et al.*, 1998]. Therefore, a statistical model of backscatter from breaking waves in which the scattering is due to multiple scattering from randomly oriented dihedrals has been proposed [*Lee et al.*, 1998] and may not be a bad approximation to reality.

6. Water Dihedrals

[30] As a first step in implementing this proposal, we calculate the backscattering cross section of dihedrals formed by two perpendicular water surfaces. The geometry is sketched in Figure 13. We will take a geometric optics approach and ignore diffraction except insofar as it enters into the determination of the cross section. Thus, we consider only incident and backscattered rays lying in the plane of incidence as shown in Figure 12. We will let the electric field vector lie at an angle ϕ to the plane of incidence.

[31] As usual for simple targets, the cross section σ is given by

$$\sigma = A_p |R|^2 D, \quad (1)$$

where A_p is the projected area, R is the reflectivity, and D is the directivity. We will let the width of the dihedral be b . Then

$$\begin{aligned} A_p &= b(a_1 \sin \theta_g + a_2 \cos \theta_g), \quad a_1 = \min(a_h, a_v \cot \theta_g); \\ a_2 &= \min(a_v, a_h \tan \theta_g), \\ R &= [R_v(\theta_g) \exp(-i\pi/2) \cos \phi + R_h(\theta_g) \sin \phi] \\ &\quad \cdot [R_v(\pi/2 - \theta_g) \exp(-i\pi/2) \cos \phi + R_h(\pi/2 - \theta_g) \sin \phi], \\ D &= 4\pi A_p / \lambda^2, \end{aligned} \quad (2)$$

where R_v and R_h are Fresnel reflection coefficients for vertical and horizontal polarization, respectively, λ is microwavelength, and a_v and a_h are the lengths of the vertical and horizontal planes of the dihedral. The factor $\exp(-i\pi/2)$ in the reflectivity accounts for the fact that R_v is a ratio of magnetic fields while R_h is a ratio of electric fields. For perfect reflectivity, $R_v = 1$ and $R_h = -1$ so the maximum cross section at $\theta_g = 45^\circ$ with $a_h = a_2 = a$ is

$$\sigma_{\max} = 8\pi a^2 b^2 / \lambda^2 \quad (3)$$

as required. The cross section for a water dihedral at X band ($\lambda = 3$ cm) is plotted versus grazing angle in Figure 14 for $b = 1$ cm and various values of a . To produce these curves, equation (1) has been convolved with a spreading function corresponding to the vertical beam width of the vertical surface:

$$f(\theta_g) = \exp\{-[4 \ln 2 \theta_g^2 a_v^2 / \lambda^2]\} / N, \quad (4)$$

where N is a normalizing factor to make the integral of f over θ_g be one.

[32] Several features of these plots are of interest. First, while the cross sections obviously increase with dihedral size at 45° , this is not true at the grazing angles of most interest to sea clutter. In particular, for grazing or incidence angles near 5° , cross sections do not monotonically increase with dihedral size. Nevertheless, these levels alone do not determine the magnitudes of backscattering cross sections since the temporal and spatial densities of the dihedrals will also affect the values. Second, peaks of the cross sections at 0° and 90° grazing angles are due to specular reflections from the vertical and horizontal planes of the dihedrals, respectively. They will clearly affect cross sections not only near grazing but also near nadir. The nadir cross sections may limit the densities of these types of scatterers that we can choose since backscattering at nadir is well understood. Third, note that the HH/VV polarization ratio is greater than one only at grazing angles above a few degrees. Since this is often higher than the nominal grazing angles used, for instance, from ships, observations of the polarization ratios will be affected by the tilting of the dihedrals by the long waves on which they ride. Finally, note that for grazing angles between about 5° and 20° , the polarization ratio increases with dihedral size. This effect will not be changed by summing over many such features. Thus we suspect that larger observed polarization ratios will correspond to larger

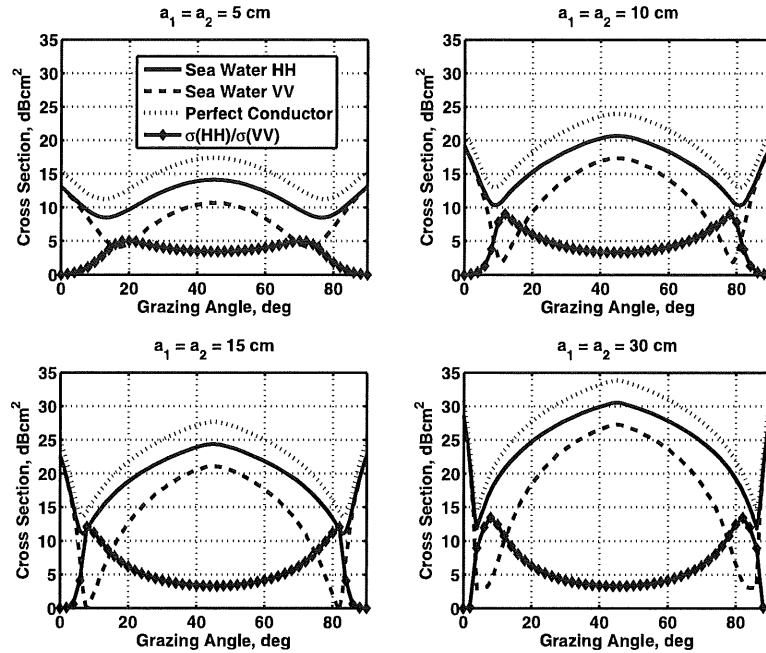


Figure 14. Cross sections of dihedral corner reflectors of various sizes as a function of grazing angle. The lines with diamonds are HH/VV polarization ratios in decibels. The width of the dihedral is 1 cm. The a_1 is the length of the horizontal plane, while a_2 is the length of the vertical plane.

dihedral features on the surface and therefore to more energetic breaking events.

7. Conclusion

[33] Measurements of the mean normalized radar cross section of the sea taken over many years, from many different platforms, and at many different incidence angles have shed light on possible backscattering mechanisms of the ocean surface. The measurements show that $\sigma_o(VV)$ for a sea surface disturbed only by wind is generally well explained by the multiscale model [Plant, 2002] over the entire range of incidence angles from 0° to 89° . This model is simply a slightly modified version of the standard composite surface theory of Wright [1968] and Bass *et al.* [1968]. $\sigma_o(HH)$, on the other hand, begins to be higher than predicted by this model at incidence angles above about 45° but remains below $\sigma_o(VV)$ under normal conditions. While at very high incidence angles, both cross sections increase with wind speed as in standard scatterometry and $\sigma_o(VV)$ displays the standard second-harmonic dependence on azimuth angle, $\sigma_o(HH)$ shows a very different azimuth angle dependence. It is highest looking into the wind and lowest looking downwind. In both cases the magnitude of $\sigma_o(HH)$ is larger than expected from the multiscale model.

[34] Observations of anomalous backscatter from the ocean that depart from this model have been obtained in the Philippine Sea. While the cause of this anomalous backscatter is unknown, it clearly shows that $\sigma_o(HH)$ can at times exceed $\sigma_o(VV)$ over large time and space scales for low-grazing-angle backscatter from the ocean. Taken together,

these observations show that other scatterers besides short wind-driven waves exist on the ocean surface. Several different types of these scatterers probably exist. They include bound, tilted waves from “crumpling” short gravity waves, jets from plunging breaking waves, spray, and multipath surfaces most conveniently described as water dihedrals. These types of scatterers begin to manifest themselves when their normalized radar cross section exceeds the standard Bragg scattering from wind waves. This most commonly occurs for HH polarization at high incidence angles but may also be caused or exaggerated by anomalous conditions such as current gradients, as is shown in part 2 [Plant *et al.*, 2010].

[35] Since multipath surfaces are likely to be the dominant types of these other scatterers at very high incidence angles, we derived a geometrical optics expression for their cross section versus grazing angle. This showed that such dihedrals must be tilted up toward the incoming signal in order to produce $\sigma_o(HH) / \sigma_o(VV)$ polarization ratios that exceed one. Still to be determined are the distribution of orientations of the dihedrals and their density on the ocean surface under different circumstances. A limitation on these variables will be the known density of specular scatterers at nadir.

[36] **Acknowledgments.** This work has been supported over many years by the Office of Naval Research, most recently under grants N00014-05-1-0244, N00014-07-1-0559, N00014-08-1-0977, and N00014-10-10318. The authors would like to thank the crews of the several airplanes and ships that have been used to collect these data. We especially thank the U.S./LTA corporation, who allowed us aboard our most unusual platform, the U.S./LTA Model 138S airship, and provided exemplary support for our measurements.

References

- Bass, F. G., I. M. Fuks, A. I. Kalmykov, I. E. Ostrovsky, and A. D. Rosenberg (1968), Very high frequency radiowave scattering by a disturbed sea surface. Part II: Scattering from an actual sea surface, *IEEE Trans. Antennas Propag.*, *16*(5), 560–568, doi:10.1109/TAP.1968.1139244.
- Chubb, S. R., A. L. Cooper, R. W. Jansen, R. A. Fusina, J.-S. Lee, and F. Askari (1999), Radar backscatter from breaking waves in Gulf Stream current convergence fronts, *IEEE Trans. Geosci. Remote Sens.*, *37*(4), 1951–1966, doi:10.1109/36.774707.
- Churyumov, A. N., Y. A. Kravtsov, O. Y. Lavrova, K. T. Litovchenko, M. I. Mityagina, and K. D. Sabinin (2002), Signatures of resonant and non-resonant scattering mechanisms on radar images of internal waves, *Int. J. Remote Sens.*, *23*(20), 4341–4355, doi:10.1080/0143160110107644.
- Elfouhaily, T., B. Chapron, K. Katsaros, and D. Vandemark (1997), A unified directional spectrum for long and short wind-driven waves, *J. Geophys. Res.*, *102*(C7), 15,781–15,796, doi:10.1029/97JC00467.
- Fuchs, J., D. Regas, T. Waseda, S. Welch, and M. P. Tulin (1999), Correlation of hydrodynamic features with LGA radar backscatter from breaking waves, *IEEE Trans. Geosci. Remote Sens.*, *37*(5), 2442–2460, doi:10.1109/36.789641.
- Fung, A. K., Z. Li, and K. S. Chen (1992), Backscattering from a randomly rough dielectric surface, *IEEE Trans. Geosci. Remote Sens.*, *30*(2), 356–369, doi:10.1109/36.134085.
- Holliday, D., L. L. DeRaad Jr., and G. J. St-Cyr (1998), Sea-spike backscatter from a steepening wave, *IEEE Trans. Antennas Propag.*, *46*(1), 108–113, doi:10.1109/8.655457.
- Hwang, P. A., W. J. Teague, G. A. Jacobs, and D. W. Wang (1998), A statistical comparison of wind speed, wave height, and wave period derived from satellite altimeters and ocean buoys in the Gulf of Mexico region, *J. Geophys. Res.*, *103*(C5), 10,451–10,468, doi:10.1029/98JC00197.
- Kalmykov, A. I., and V. V. Pustovoytenko (1976), On polarization features of radio signals scattered from the sea surface at small grazing angles, *J. Geophys. Res.*, *81*(12), 1960–1964, doi:10.1029/JC081i1012p01960.
- Kudryavtsev, V., D. Akimov, J. Johannessen, and B. Chapron (2005), On radar imaging of current features: 1. Model and comparison with observations, *J. Geophys. Res.*, *110*, C07016, doi:10.1029/2004JC002505.
- Lee, P. H. Y., J. D. Barter, K. L. Beach, C. L. Hindman, B. M. Lake, H. Rungaldier, H. R. Thompson Jr., and R. Yee (1997), Experiments on Bragg and non-Bragg scattering using single-frequency and chirped radars, *Radio Sci.*, *32*(5), 1725–1744, doi:10.1029/97RS01399.
- Lee, P. H. Y., J. D. Barter, K. L. Beach, B. M. Lake, H. Rungaldier, H. R. Thompson Jr., and R. Yee (1998), Scattering from breaking gravity waves without wind, *IEEE Trans. Antennas Propag.*, *46*(1), 14–26, doi:10.1109/8.655447.
- Lee, P. H. Y., J. D. Barter, K. L. Beach, B. M. Lake, H. Rungaldier, H. R. Thompson Jr., L. Wang, and R. Yee (1999), What are the mechanisms for non-Bragg scattering from water waves?, *Radio Sci.*, *34*(1), 123–138, doi:10.1029/1998RS900024.
- Lewis, B. L., and I. D. Olin (1980), Experimental study and theoretical model of high-resolution radar backscatter from the sea, *Radio Sci.*, *15*(4), 815–828, doi:10.1029/RS015i004p00815.
- Li, Y. Z., and J. C. West (2006), Low-grazing-angle scattering from 3-D breaking water wave crests, *IEEE Trans. Geosci. Remote Sens.*, *44*(8), 2093–2101, doi:10.1109/TGRS.2006.872129.
- Lyzenga, D. R., A. L. Maffett, and R. A. Shuchman (1983), The contribution of wedge scattering to the radar cross section of the ocean surface, *IEEE Trans. Geosci. Remote Sens.*, *21*(4), 502–505, doi:10.1109/TGRS.1983.350513.
- Plant, W. J. (1997), A model for microwave Doppler sea return at high incidence angles: Bragg scattering from bound, tilted waves, *J. Geophys. Res.*, *102*(C9), 21,131–21,146, doi:10.1029/97JC01225.
- Plant, W. J. (2000), Effects of wind variability on scatterometry at low wind speeds, *J. Geophys. Res.*, *105*(C7), 16,899–16,910, doi:10.1029/2000JC900043.
- Plant, W. J. (2002), A stochastic, multiscale model of microwave backscatter from the ocean, *J. Geophys. Res.*, *107*(C9), 3120, doi:10.1029/2001JC000909.
- Plant, W. J. (2003a), A new interpretation of sea-surface slope probability density functions, *J. Geophys. Res.*, *108*(C9), 3295, doi:10.1029/2003JC001870.
- Plant, W. J. (2003b), Microwave sea return at moderate to high incidence angles, *Waves Random Media*, *13*(4), 339–354, doi:10.1088/0959-7174/13/4/009.
- Plant, W. J., W. C. Keller, V. Hesany, and K. Hayes (1998), Measurements of the marine boundary layer from an airship, *J. Atmos. Oceanic Technol.*, *15*, 1433–1458, doi:10.1175/1520-0426(1998)015<1433:MOTMBL>2.0.CO;2.
- Plant, W. J., W. C. Keller, V. Hesany, T. Hara, E. Bock, and M. Donelan (1999a), Bound waves and Bragg scattering in a wind-wave tank, *J. Geophys. Res.*, *104*(C2), 3243–3263, doi:10.1029/1998JC900061.
- Plant, W. J., P. H. Dahl, and W. C. Keller (1999b), Microwave and acoustic scattering from parasitic capillary waves, *J. Geophys. Res.*, *104*(C11), 25,853–25,866, doi:10.1029/1999JC900168.
- Plant, W. J., P. H. Dahl, J. P. Giovanangeli, and H. Branger (2004), Bound and free surface waves in a large wind-wave tank, *J. Geophys. Res.*, *109*, C10002, doi:10.1029/2004JC002342.
- Plant, W. J., W. C. Keller, and K. Hayes (2005), Simultaneous measurement of ocean winds and waves with an airborne coherent real aperture radar, *J. Atmos. Oceanic Technol.*, *22*, 832–846, doi:10.1175/JTECH1724.1.
- Plant, W. J., W. C. Keller, and W. E. Asher (2006), Is sea spray a factor in microwave backscatter from the ocean?, *IEEE MicroRad Proc.*, *1*, 115–118, doi:10.1109/MICRAD.2006.1677050.
- Plant, W. J., W. C. Keller, K. Hayes, G. Chatham, and N. Lederer (2010), Normalized radar cross section of the sea for backscatter: 2. Modulation by internal waves, *J. Geophys. Res.*, *115*, C09033, doi:10.1029/2009JC006079.
- Rozenberg, A. D., M. J. Ritter, W. K. Melville, C. C. Gottschall, and A. V. Smirnov (1999), Free and bound capillary waves as microwave scatterers: Laboratory studies, *IEEE Trans. Geosci. Remote Sens.*, *37*(2), 1052–1065, doi:10.1109/36.752223.
- Sletten, M. A., J. C. West, X. Liu, and J. H. Duncan (2003), Radar investigations of breaking water waves at low grazing angles with simultaneous high-speed optical imagery, *Radio Sci.*, *38*(6), 1110, doi:10.1029/2002RS002716.
- Trizna, D. B. (1997), A model for Brewster angle damping and multipath effects on the microwave radar sea echo at low grazing angles, *IEEE Trans. Geosci. Remote Sens.*, *35*(5), 1232–1244, doi:10.1109/36.628790.
- Trizna, D. B., and D. J. Carlson (1996), Studies of dual polarized low grazing angle radar sea scatter in nearshore regions, *IEEE Trans. Geosci. Remote Sens.*, *34*(3), 747–757, doi:10.1109/36.499754.
- Voronovich, A. G. (1985), Small-slope approximation in wave scattering by rough surfaces, *Sov. Phys. JETP, Engl. Transl.*, *62*(1), 65–70.
- West, J. C. (1999), Ray analysis of low-grazing scattering from a breaking water wave, *IEEE Trans. Geosci. Remote Sens.*, *37*(6), 2725–2727, doi:10.1109/36.803420.
- West, J. C. (2002), Electromagnetic modeling of multipath scattering from breaking water waves with rough faces, *IEEE Trans. Geosci. Remote Sensing*, *40*(3), 583–592, doi:10.1109/TGRS.2002.1000318.
- Wetzel, L. (1986), On microwave scattering by breaking waves, in *Wave Dynamics and Radio Probing of the Ocean Surface*, edited by K. Hasselmann and O. M. Phillips, pp. 273–284, Plenum, New York.
- Wiltse, J. C., S. P. Schlesinger, and C. M. Johnson (1957), Backscattering characteristics of the sea in the region from 10 to 50 mKc, *Proc. IRE*, *45*, 220–228.
- Wright, J. W. (1968), A new model for sea clutter, *IEEE Trans. Antennas Propag.*, *16*(2), 217–223, doi:10.1109/TAP.1968.1139147.

G. Chatham, K. Hayes, W. C. Keller, and W. J. Plant, Applied Physics Laboratory, University of Washington, 1013 NE 40th St., Seattle, WA 98105-6698, USA. (plant@apl.washington.edu)

Normalized radar cross section of the sea for backscatter: 2. Modulation by internal waves

William J. Plant,¹ William C. Keller,¹ Kenneth Hayes,¹ Gene Chatham,¹
and Nicholas Lederer¹

Received 21 December 2009; revised 18 May 2010; accepted 26 May 2010; published 30 September 2010.

[1] We report measurements of microwave surface signatures of internal waves with dual-polarized, coherent, X band radars mounted on three ships and an airplane. In shipboard measurements in the South China Sea, internal waves generally increased the backscattering cross section near the peaks of the internal waves with little detectable decrease afterward. The peak of the cross-section signature shifted its location relative to the internal wave crest depending on the maximum strain rate of the internal wave. We show that a similar shift is produced in the modulation of short-gravity waves by internal waves. We suggest that this modulation of “intermediate-scale” waves causes small-scale radar scatterers to maximize at this location. In shipboard measurements off the New Jersey coast, the range resolution of the radar was sufficiently small to allow us to detect significant modulation of gravity waves on the order of 15–30 m long by the internal waves. At the high incidence angles of the shipboard measurements, the cross section for horizontally polarized transmit and receive signals, $\sigma_o(\text{HH})$, regularly exceeded that for vertically polarized transmit and receive signals, $\sigma_o(\text{VV})$, near the internal wave crest by 5–10 dB. At the more moderate incidence angles observed from the aircraft, maximum values of $\sigma_o(\text{HH})$ and $\sigma_o(\text{VV})$ are more nearly equal, with $\sigma_o(\text{HH})$ often being comparable to $\sigma_o(\text{VV})$ and only occasionally exceeding it. These observations suggest that roughness due to breaking short-gravity waves plays a significant role in producing microwave signatures of internal waves, even at moderate incidence angles where it competes with the modulation of wind-generated waves. The intensity of modulation of the cross section caused by internal waves observed from the plane depended little on the direction of observation. Internal wave surface signatures from the aircraft became less visible with increasing wind speed, being very difficult to observe at 9 m/s.

Citation: Plant, W. J., W. C. Keller, K. Hayes, G. Chatham, and N. Lederer (2010), Normalized radar cross section of the sea for backscatter: 2. Modulation by internal waves, *J. Geophys. Res.*, 115, C09033, doi:10.1029/2009JC006079.

1. Introduction

[2] When internal waves propagate on density interfaces below the ocean surface, they produce surface currents that modulate surface waves, thus producing detectable signatures in microwave backscatter from the surface. These signatures are easily observed by synthetic aperture radar and a very large number of images of internal wave surface signatures have been obtained from orbiting spacecraft [Apel, 2004; Liu *et al.*, 2008]. Recently, sea return to shipboard radars has begun to be recorded and internal wave surface signatures in this return have been examined [Liu *et al.*, 2008; Chang *et al.*, 2008].

[3] Studies aimed at understanding the mechanisms by which internal waves modulate surface waves to produce

microwave signatures have been carried out over many years. Among the experimental studies are the seminal observations of *Apel et al.* [1975] from the Earth Resources Technology satellite, the 1972 work of *Hughes and Grant* [1978], the 1983 Joint Canada-U.S. Ocean Wave Investigation Project (JOWIP, also called the Georgia Straits Experiment) [*Hughes and Dawson*, 1988], the 1984 SAR Internal Wave Signature Experiment (SARSEX) [*Hughes and Gasparovic*, 1988], the 1987 Loch Linnhe experiment [*Hogan et al.*, 1996], the 1995 Coastal Ocean Probing Experiment (COPE) [*Kropfli et al.*, 1999], and work near the Strait of Messina [*Alpers and Salusti*, 1983; *Brandt et al.*, 1997] and the Strait of Gibraltar [*Brandt et al.*, 1996]. Theoretical studies into the generation of internal wave microwave surface signatures include those of *Alpers* [1985], *Lyzenga and Bennett* [1988], *Thompson* [1988], and *Kudryavtsev et al.* [2005].

[4] Nevertheless, significant gaps still exist in our understanding of how the surface currents associated with internal waves generate the signatures observed in microwave backscatter. While the role of surface current gradients in straining

¹Applied Physics Laboratory, University of Washington, Seattle, Washington, USA.

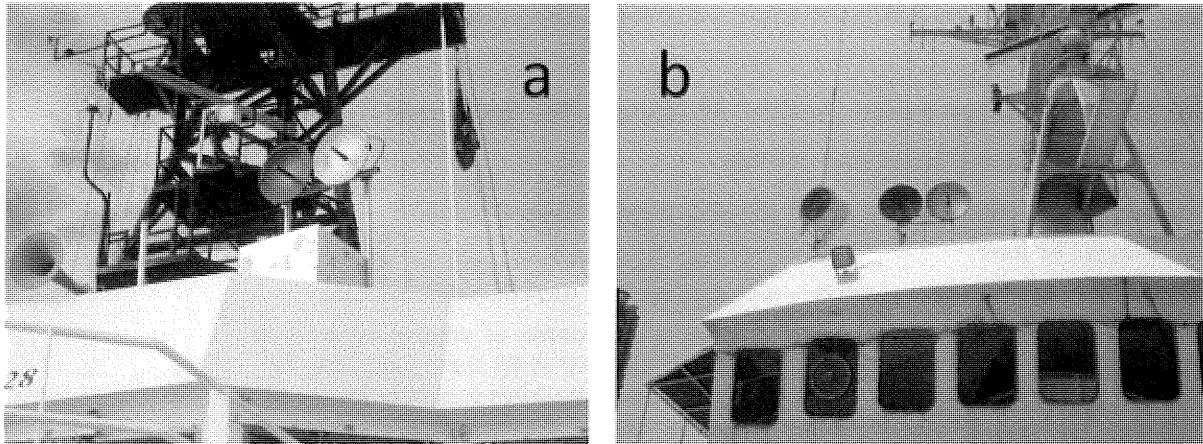


Figure 1. (a) The parabolic antennas of RiverRad mounted on the R/V *Revelle* in 2005. (b) RiverRad mounted on the Taiwanese ship R/V *Ocean Researcher 1* in 2007.

surface waves is clear, it is still not known how often these current gradients simply modulate surface waves and how often they cause surface waves to break thus generating short microwave scattering elements on the surface. Because both transmitting and receiving a horizontally polarized microwave signal (HH backscatter) causes sea return to be more sensitive to breaking surface waves than transmitting and receiving vertically polarized signals (VV backscatter), comparison of internal wave signatures at the two polarizations offers the possibility of investigating the prevalence of breaking waves in the signatures [Plant, 1997; Liu *et al.*, 1998; Hwang *et al.*, 2008]. Unfortunately, very little work has been done in which HH- and VV-polarized signals have been used at nearly the same time to observe internal wave signatures, especially at moderate incidence angles [Kropfli *et al.*, 1999; Churyumov *et al.*, 2002]. Even less work has been done to produce well-calibrated normalized radar cross section (NRCS) values near internal waves. Similarly, the determination of the dependence of the microwave signatures on azimuth angle has been little studied. Finally, in most situations, it is difficult to determine precisely the location of the surface signature with respect to an internal wave crest.

[5] In this paper, we address these issues. This second part of a two-paper series builds on part 1, where we showed that a Bragg-scattering-type model can explain the mean normalized radar cross section (NRCS) at VV polarization for incidence angles from 0° to 89° , but not at HH. We suggested that breaking waves play a large role in HH backscatter and a smaller role in VV [Plant *et al.*, 2010]. Here we report the effect of internal waves (IWs) on the NRCS of the sea, σ_o , and on the scatterer velocity and suggest that breaking plays a larger role in determining microwave signatures of IWs than it does in backscatter from a sea disturbed only by wind. All measurements reported here were made with HH and VV returns measured within a fraction of a second of each other, although in one experiment a switch failed so we only obtained VV signals and in another the HH and VV antennas looked in different directions. All NRCS values are calibrated. While the shipboard measurements were generally made with the radar antennas looking either in the direction of IW propagation or against it, the

aircraft measurements were made at many different azimuth angles so the dependence of signature intensities on antenna look direction could be studied. Finally, by comparing the shipboard radar measurements with currents measured simultaneously by acoustic Doppler current profilers (ADCPs) on the same ships, the location of the surface signature relative to IW crests could be determined.

[6] Our measurements were made as part of the Office of Naval Research (ONR) Nonlinear Internal Wave Initiative (NLIWI) with the aim of better understanding microwave signatures of very nonlinear internal waves. Because the measurements were made both in the South China Sea and in the Atlantic Ocean off the New Jersey coast, two very different types of internal waves were studied. In the South China Sea, surface signatures of very nonlinear internal solitons, which traveled in widely spaced trains, were observed. We also found that in the South China Sea, regular nearly sinusoidal trains of smaller amplitude internal waves were very frequently observed. These smaller waves were similar to the internal waves encountered off the New Jersey coast. We first discuss signatures of the nonlinear solitons, then the smaller sinusoidal wave trains.

2. Shipboard Measurements in the South China Sea

[7] Two sets of shipboard measurements were made in the South China Sea. In 2005, our X band, coherent radar called RiverRad was mounted on the R/V *Revelle* and made measurements in the South China Sea from 18 April to 14 May. These measurements were all made in deep water. In 2007, we operated RiverRad on two cruises, one from 24 April to 13 May was in the relatively shallow water of the western shelf of the South China Sea and the second from 13 May to 20 May was in deep water. On all these cruises, the parabolic, pencil-beam antennas were pointed approximately in the direction of the ship's heading. Figure 1 shows RiverRad mounted on these two ships, while Figure 2 indicates where in the South China Sea significant nonlinear solitons were encountered.

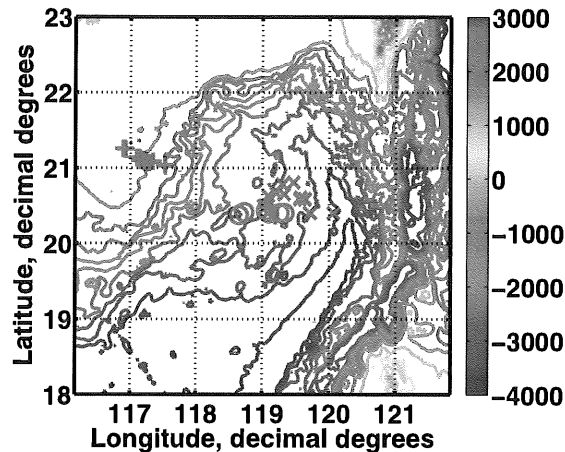


Figure 2. Locations at which nonlinear internal solitons were encountered in the South China Sea. Pluses are for shallow water in 2007, circles are for deep water in 2007, and crosses indicate deep water in 2005.

[8] Standard shipboard measurements of wind speed and direction, ship speed and direction, and currents from ADCPs were collected and recorded on the cruises. From the latter measurements, currents were extracted from the nearest good bin to the surface and resolved into components in and perpendicular to the ship heading as shown in Figure 3c. In 2005, the nearest good bin to the surface was 17 m below the surface; in 2007, it was 52 m deep. In addition, latitude, longitude, time, pitch, and roll were recorded during the cruise. We also had a GPS receiver mounted on the RiverRad antennas and its speed readings were used to correct the Doppler shifts observed by RiverRad.

[9] Microwave data consisted of the standard output of RiverRad, which has been described previously elsewhere [Plant *et al.*, 2005b]. Briefly, RiverRad is a coherent, 9.36 GHz radar that transmits and receives signals from a single parabolic antenna. It interrogates a series of range bins sufficiently rapidly to calculate a Doppler spectrum at every bin. Averages of these spectra over a complete record are stored for each range bin but were used only for quality control in this study. In 2005 a record was 50 s long, in 2007 it was 30 min long. In addition, the first three moments of the Doppler spectrum, mean received power, Doppler offset, and Doppler bandwidth are stored for every scan, each of which was approximately 365 ms long. Alternate scans were collected with HH and VV polarizations by switching between the two antennas. Therefore a scan at each polarization was 365 ms long and occurred every 730 ms. The range resolution was 15 m in 2005 and 30 m in 2007.

[10] Our original intention was to use the pitch and roll recorded on the ship to compute the incidence angle of the radar. However, uncertainties in the measurement of the incidence angle when pitch and roll were both zero forced us to use a different method. Because the antenna beams were so narrow, the location of the maximum return power averaged over several range bins was well related to the instantaneous incidence angle. The relationship between received power, P_r , and incidence angle, θ , is $P_r \sim G^2(\theta) \cos^3\theta/\sin\theta$

where the antenna gain can be well represented by $G \sim \exp[-8\ln 2(\theta - \theta_0)^2/\alpha^2]$, α being the one-way, half-power beam width. The maximum of P_r then yields the nominal incidence angle θ_0 , which varies with the pitch and roll of the ship. We found this to be the most reliable method of determining instantaneous incidence angle.

[11] From the three recorded moments of the spectrum, we obtained the normalized radar cross section (NRCS or σ_o , a measure of surface roughness), the mean surface velocity, and the spread in scatterer velocities for each range bin averaged over a scan time (365 ms). The NRCS was obtained from the mean received power using the radar equation along with a calibration constant which we had determined on our laboratory antenna range. This determination used a carefully oriented corner reflector and a moveable mount for the antenna. Maximizing the return from the corner reflector and utilizing its known cross section allowed us to determine the calibration constant to within about 1 dB. More details of the calibration procedure are given by Plant *et al.* [1994].

[12] Figure 3 gives an example of data collected on these cruises. Images of the scatterer velocity are shown in Figure 3a, while images of σ_o are shown in Figure 3b. These images are space-time plots of the return to the radar along the antenna-look direction, the direction of the ship's heading. They were smoothed over 50 s. The vertical axis is distance along the ship's heading from the start of the run. The black dotted curves in the images show the location of the ship.

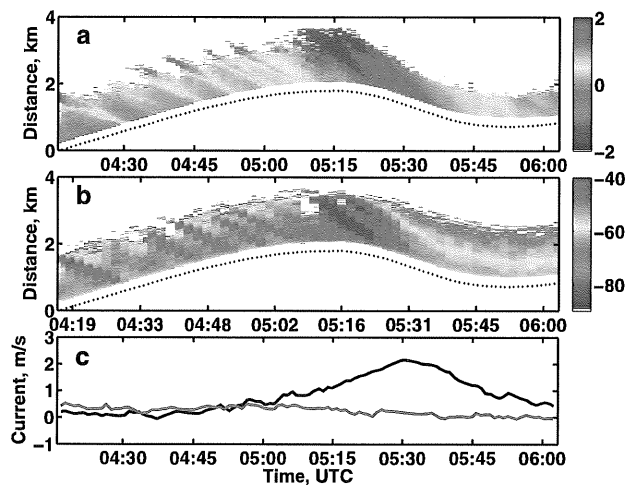


Figure 3. Data collected from the R/V *Reville* on 28 April 2005 averaged over 50 s. (a) Radar surface (scatterer) velocities in the direction of the ship's heading as functions of distance in the heading direction and time. The curve of black dots is the ship's location. (b) Same as Figure 3a but for the normalized radar cross section, $\sigma_o(VV)$. (c) ADCP current at 17 m depth parallel (black, positive toward antenna) and perpendicular (green, positive toward starboard) to the ship's heading. Wind speed was 2.4 m/s, wind direction (from) was $221^\circ T$, ship speed at locations away from IW was 0.5 m/s, and ship heading was $80^\circ T$. Currents were measured at 17 m depth in deep water. The location of the measurements was $(20.59^\circ N, 119.59^\circ W)$.

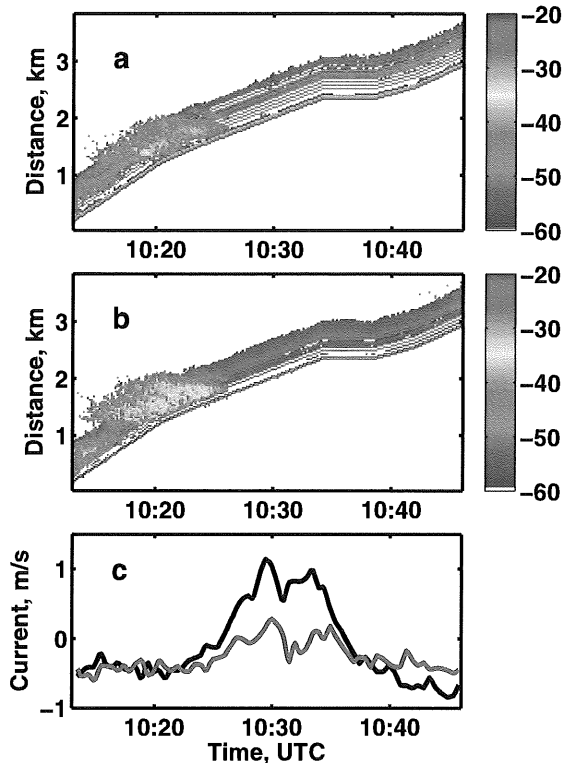


Figure 4. Data from the 2007 cruise of the R/V *Ocean Researcher 1* on the shelf of the South China Sea on 4 May 2007 starting at 0939:47 UTC. (a) $\sigma_0(VV)$ in decibels. (b) $\sigma_0(HH)$ in decibels. (c) ADCP currents parallel to ship heading (black, positive toward antenna) and perpendicular to ship heading (green, positive toward starboard). Wind speed was 5.4 m/s, wind direction (from) was $187^\circ T$, ship speed at locations away from IW was 1.5 m/s, and ship heading was $126^\circ T$. Currents were measured at 52.4 m depth in water of depth 389 m. The location of the measurements was $(21.12^\circ N, 117.18^\circ W)$.

Note how the currents of the IW advect the ship. The radar return starts about 250 m in front of the ship and goes out to almost 2 km. The antennas were 18 m above the water surface so the incidence angle ranged from 85.9° to 89.5° . This type of display places the radar return at the location it has for a stationary observer if the ship's heading is constant.

[13] Surface signatures of two types of internal waves, small nearly sinusoidal waves and a larger soliton wave, are clearly present in both the velocity and cross section measured by the radar. As indicated by the sign of the ADCP-measured internal soliton current along the heading and the lack of internal soliton current perpendicular to the heading, the ship was traveling directly opposite the direction of propagation of the large internal wave. The train of smaller sinusoidal internal waves with a wavelength of less than 800 m is observed in both the surface currents and cross sections in front of the large soliton. Both the surface velocity and the cross section of the smaller waves increase significantly over the large internal wave. Apparently the inter-

action of the soliton and the smaller wave train increases the amplitude of the small wave train. In fact the small wave train is difficult to observe after the ship has passed the soliton, indicating that it may have been blocked by the soliton.

[14] The slope of these surface features is the speed of the internal wave if the perpendicular ADCP current is zero. If the internal waves do not propagate directly toward or away from the radar, then the slope of the feature is the maximum possible speed of the internal wave. The train of small internal waves is clearly visible in the radar return but is barely visible in the currents measured at 17 m depth. This makes it difficult to determine their direction of propagation except that a component of their propagation vector comes toward the ship because the slope, dR/dt , is negative. We can say with certainty that the train of small internal waves is moving much more slowly than the soliton since we know the direction of soliton travel. Crests of the wave train require a longer time to travel a given distance than do the soliton crests. Thus the speed of the train is smaller than that of the soliton no matter what direction it travels. Furthermore, the speed of a crest increases as it approaches the crest of the soliton because the slope of the crest, dR/dt , becomes less negative, that is, smaller in magnitude.

[15] We now leave the wave trains to concentrate on the large solitons. In order to obtain the precise location of the increases in cross section and surface velocity caused by the soliton with respect to the location of the soliton, their effects must be extrapolated to the position of the ship. Carrying out this extrapolation in the images of Figure 3, clearly shows that the surface signature of the internal wave, in both cross section and velocity, is nearly directly above the soliton crest. As we will show later, we generally found that in deep water, the surface signature maximized near the crest of the internal wave.

[16] Figure 4 shows that the signature does not always maximize directly above the soliton crest. The data shown in Figure 4 are from the 2007 cruise on the OR1 in shallow water. The format of Figure 4 is the same as that of Figure 3. Again, the ship travels very nearly opposite the direction of soliton movement. Now, however, maxima in both the cross section and surface velocity signatures of the wave occur well before the crest of the soliton reaches the ship.

[17] Figure 5 summarizes the location of the maximum cross section with respect to soliton wave crests for all of the data we collected in 2005 and 2007. Figure 5a shows the situation schematically. The internal wave moves right, L is the distance by which the microwave surface signature leads the wave crest, W is the full width of the soliton at half its maximum velocity, V_m . This velocity, of course, is in the direction of soliton travel. Figure 5b shows measured values of L/W versus $1000 \cdot V_m/W$, the latter quantity being proportional to the maximum strain rate of the soliton. Because L is positive, Figure 5b shows that the microwave signature of the soliton occurs farther in front of the crest when the soliton is steeper. In only one case, the cross enclosed in a triangle, did this behavior obviously not occur. In general, solitons in the shallow water of the shelf are steeper than in deep water, and their signatures lead the soliton crest by greater distances than those in deep water.

[18] In the majority of cases that we examined, the response of the cross section to the surface currents set up by

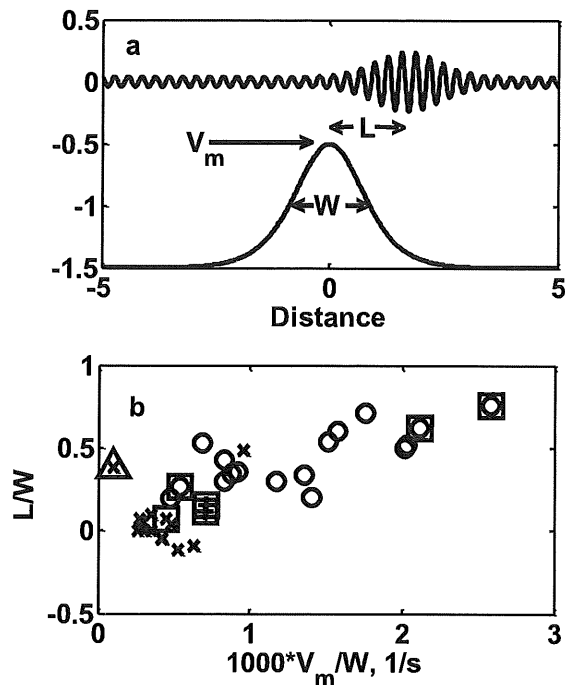


Figure 5. (a) Diagram showing IW velocities and the related surface roughness. The IW is moving to the right. L is positive when the roughness is in front of the maximum IW velocity; W is the full width at half maximum. (b) Measured relationship of the surface roughness location to the maximum IW velocity. Crosses are for 2005, deep water; circles are for 2007, shelf; and pluses are for 2007, deep water. Symbols with squares or a triangle around them are discussed in the text.

the internal waves was an increase unaccompanied by any detectable decrease. The symbols in Figure 5 that are enclosed in squares show the cases where this was not true and the increase was followed by a significant decrease. We do not believe that the behavior of the majority of our data is due to the fact that a decrease in cross section is hidden by noise, as suggested by *da Silva et al.* [1998] for SAR imagery of internal waves. Figure 6 illustrates that RiverRad's signals are generally well above the noise level. Two of the cases where increases were followed by decreases are illustrated in Figures 7 and 8. Figure 7 is in the same format as Figure 6 and shows an NRCS increase followed by a decrease. Note the presence of small nearly sinusoidal waves before the internal soliton arrives at the ship and their absence afterward. Figure 8 illustrates a case from 2007 where the sinusoidal waves are not so prominent. Note that the increase followed by a decrease occurs for both HH and VV polarizations for the first internal wave but does not occur for either polarization when the second internal wave arrives. For both internal waves, the polarization ratio exceeds 3 dB at its maximum value, well above a value that could be explained by the uncertainties in our NRCS measurements.

[19] Most researchers today agree that the direct modulation of gravity-capillary Bragg waves by IW surface currents is very small. Therefore intermediate-scale waves, short-gravity waves that are modulated by the internal wave

currents, should determine the location at which the microwave signature maximizes because the steepest short-gravity waves produce the most microwave scatterers [Thompson and Gasparovic, 1986; Thompson, 1988; Lyzenga and Bennett, 1988; Kudryavtsev et al., 2005]. Thus we modeled the modulation of the mean square slope (mss) of waves between 24 cm and 400 cm long. Note that we are not attempting to model the amplitude of our microwave signatures. Rather we want to determine whether the locations of microwave signatures with respect to the internal wave crest behave the same as short-gravity wave slopes. We computed the modulation of short-gravity waves by internal solitons of fixed width but of variable amplitude using the action balance techniques described by Lyzenga and Bennett [1988]. We used a 4 m/s wind speed and three different wind directions relative to the internal wave propagation direction, 0° , 90° , and 180° . Phase speeds, C_{IW} , of the internal waves were assumed to be related to their maximum velocities, V_m (both in m/s) by $C_{IW} = 1.6 + 0.5V_m$. The results are shown in Figure 9.

[20] We found that when the wind blew against the internal wave, the maximum mss of the short-gravity waves

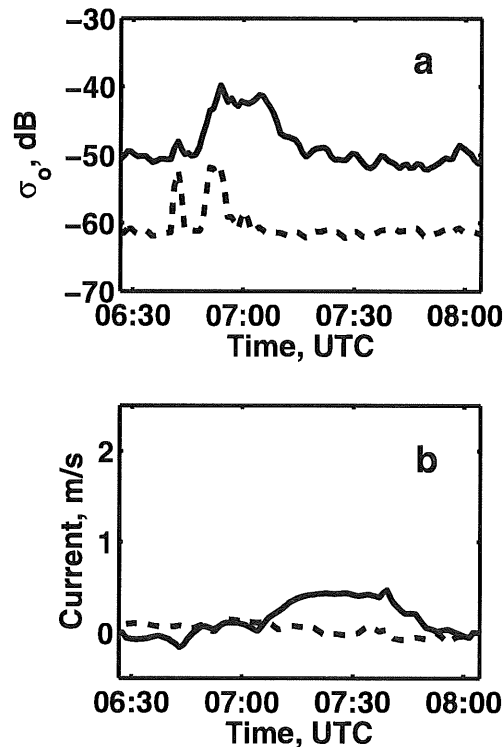


Figure 6. (a) NRCS (σ_0) measured on 24 April 2005 at a range of $700 \text{ m} \pm 30 \text{ m}$ as a function of time. The solid curve is σ_0 , while the dashed curve is the noise-equivalent NRCS. (b) The solid curve is the ADCP current in the heading direction, while the dashed curve is the ADCP current perpendicular to the heading. The sign convention is the same as in Figure 3. Wind speed was 4.0 m/s, wind direction (from) was 18°T , ship speed at locations away from IW was 0.9 m/s, and ship heading was 85°T . Currents were measured at 17 m depth in deep water. The location of the measurements was (20.80°N , 119.44°W).

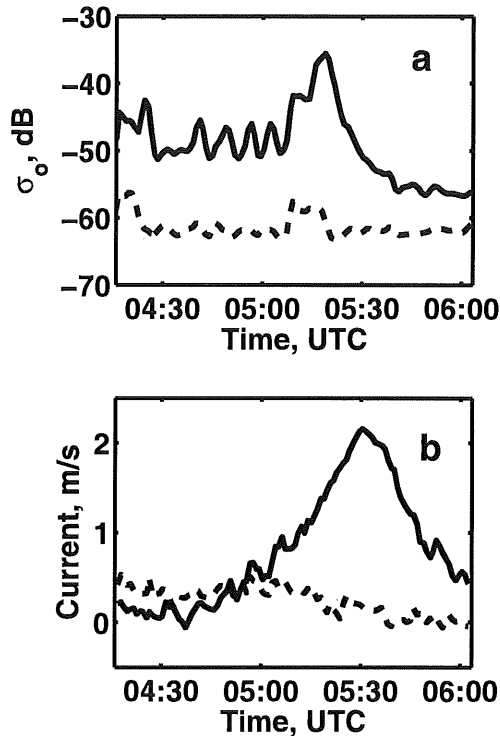


Figure 7. Same as Figure 6 but for 28 April 2005, illustrating a case where an internal wave caused an NRCS increase followed by a decrease. Wind speed was 2.5 m/s, wind direction (from) was 219°T, ship speed at locations away from IW was 0.8 m/s, and ship heading was 80°T. Currents were measured at 17 m depth in deep water. The location of the measurements was (20.58°N, 119.62°W).

moved down the forward face of the internal wave as its amplitude increased, but by much smaller distances than we observed (Figure 9d and triangles in Figure 9a). When the wind blew perpendicular to the internal wave, the maximum moved much more in line with our observations (Figures 9c and squares in Figure 9a). When the wind blew in the direction of the internal wave, the maximum moved down the forward face of the internal wave somewhat farther than the majority of our measurements did (Figure 9b and circles in Figure 9a). The vast majority of wind directions during our experiments were either in the internal wave propagation direction or perpendicular to it. This strongly suggests that microwave surface signatures of internal waves maximize where short-gravity-wave slopes maximize, confirming the indirect modulation or generation of microwave scatterers.

[21] The sudden jumps in mss of the short-gravity waves seen in Figures 9b and 9c occur where the longer short-gravity waves are no longer able to approach the internal wave crest. This region is presumably accompanied by breaking, which the model is unable to reproduce. Closer to the crest of the internal wave, both on the front and rear side, these long, short-gravity waves are trapped by the internal wave and never able to get far away from the crest. Thus their amplitude is increased much less by the internal wave currents. Finally behind the internal wave, the short-gravity waves become able to propagate away from the internal wave

crest; they are no longer trapped. These results agree with those of *Ramamonjariisoa* [1995].

[22] For all three of the wind directions that we modeled, a depression of the mss of the short-gravity waves occurred behind the crest of the internal wave. This depression was generally small for low-amplitude internal waves but became larger as the internal wave steepness increased. If the mss of these intermediate-scale waves plays a role in determining the level of the microwave scatterers, then this decrease should reduce σ_0 . Our data do lend some support to the idea of a larger decrease of σ_0 behind internal waves of larger amplitude (see Figures 6–8). However, Figure 5b shows that this was not consistently the case. Nevertheless, the very small decreases associated with smaller amplitude internal solitons may explain why we generally were not able to observe decreased NRCS associated with the surface signatures.

3. Airborne and Shipboard Measurements off the New Jersey Coast

[23] Our measurements in the Atlantic Ocean near the New Jersey shelf break suggest that the increased steepness of short-gravity waves caused by internal waves increases the probability that the short-gravity waves will break. The measurements were made both on the R/V Endeavor and on a Cessna Skymaster. Figure 10a shows RiverRad mounted on the ship, while Figure 10b shows a similar, coherent radar, Coherent Real Aperture Radar (CORAR), mounted on the plane.

[24] For the shipboard measurements, RiverRad's antennas were scanned back and forth in a windshield-wiper fashion through an arc 80° in azimuth centered at a 24° higher azimuth angle than the heading. The antennas were mounted 35° apart in azimuth; one was VV polarized and the other was HH polarized. The VV antenna was at the higher azimuth angle. The antennas swept through their 80° arc in approximately 40 s. Thus the arcs only partially overlapped and one antenna looked in the direction of the ship heading only about every 20 s. The range resolution was set to 3.75 m.

[25] The airborne measurements were made in a side-looking mode. The VV and HH antennas were mounted one above the other looking to the left side of the plane. CORAR has been described in detail by *Plant et al.* [2005a]. CORAR is very similar to RiverRad except that data are collected and stored more quickly, as is necessary for airborne operation. A scan was 340 ms in length and the first three spectral moments were saved at every range bin on each scan along with a complete spectrum from a selected range bin.

[26] Figure 11 shows an image of internal waves from the shipboard data collected on the Endeavor. Figures 11a and 11b show cross sections at HH and VV polarizations, respectively, while Figures 11c and 11d show the corresponding scatterer velocities. White areas indicate regions of very low signal level from which cross sections and velocities could not be obtained. Clearly $\sigma_0(\text{HH})$ is much larger than $\sigma_0(\text{VV})$ at the maxima of surface signatures of the internal waves. Similarly scatterer velocities are much larger for HH polarization than for VV. Velocities at HH frequently exceed 1 m/s, sometimes reaching 2 to 3 m/s. Similarly high velocities can be seen in the VV image though velocities in general are much lower at this polarization. We

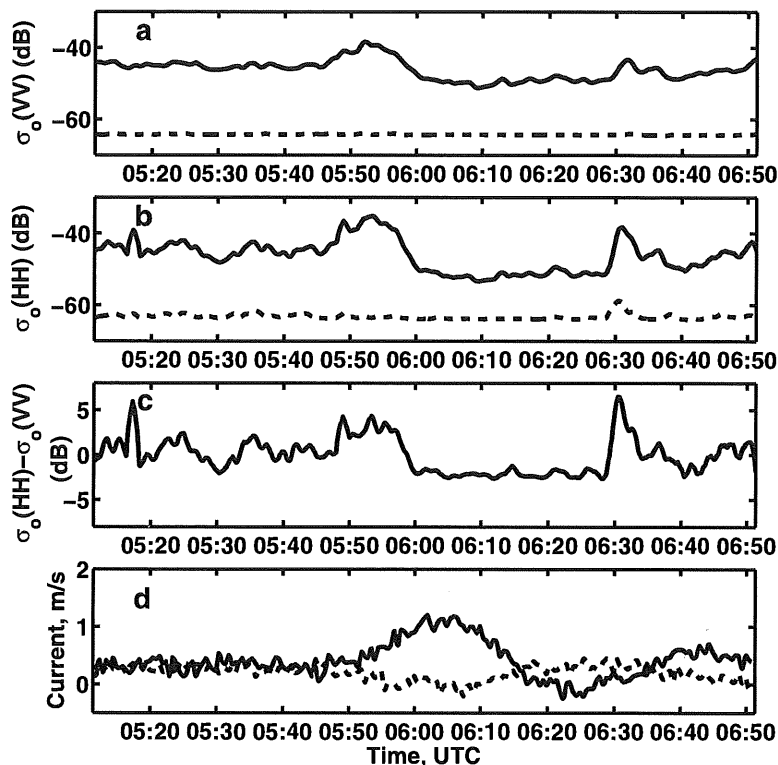


Figure 8. Illustration of two sequential internal waves causing different responses in the NRCS on 1 May 2007. (a) NRCS versus time. The solid curve is $\sigma_o(\text{VV})$, while the dashed curve is noise-equivalent $\sigma_o(\text{VV})$. (b) Same as Figure 8a but for HH. (c) Polarization ratio $\sigma_o(\text{HH}) - \sigma_o(\text{VV})$ in decibels. (d) ADCP currents parallel (solid curve) and perpendicular (dashed curve) to the ship's heading. Wind speed was 5.4 m/s, wind direction (from) was 306°T , ship speed at locations away from IW was 0.5 m/s, and ship heading was 58°T . Currents were measured at 54.2 m depth in water of depth 611 m. The location of the measurements was $(21.09^\circ\text{N}, 117.34^\circ\text{W})$.

interpret these results as being evidence of the involvement of breaking waves in microwave signatures of internal waves.

[27] Unfortunately, we were unable to determine the phase of the microwave signatures with respect to the surface velocities set up by the internal waves for these shipboard measurements because the radar measurements and the ADCP current measurements did not overlap. The radar operated early in the experiment until a large storm damaged the antennas and the ADCP did not begin operating until after this storm.

[28] One striking feature of the images shown in Figure 11 is that both the cross sections and velocities are highly variable within the area of strong return. If we average the data in the σ_o images that are within 20° of the ship's heading, we obtain plots of σ_o as a function of ground range such as those shown in Figure 12. For the three different times shown in Figure 12, the ship was always heading into the internal waves and the antennas were always rotating counterclockwise. Thus the VV antenna viewed the heading direction about 20 s later than the HH antenna and the figure shows that the internal wave has advanced (moved left) during that time. This motion includes both the internal wave speed and the ship speed. Figures 12a–12f show oscillations of the NRCS with lengths 15–30 m. For the HH return these

oscillations increase significantly on the forward face of the general increase in cross section owing to the internal waves. These regions are circled in Figures 12a, 12b, and 12c. This strongly suggests that the internal waves increase the amplitudes of short-gravity waves in this region, leading to an oscillating cross section. The differences between the ship's heading and the wind direction in the three cases shown are 104° , 74° , and 118° . Thus, the wind is almost perpendicular to the internal wave in all cases so a significant increase in short-gravity waves is expected in front of the crest of the internal wave as shown in Figure 9c. The increase in these waves affects $\sigma_o(\text{HH})$ more $\sigma_o(\text{VV})$ but can also be detected in $\sigma_o(\text{VV})$ (circled parts of Figures 12d and 12e).

[29] The airborne imagery also confirms that $\sigma_o(\text{HH})$ is more affected by internal waves than $\sigma_o(\text{VV})$. Figure 13 documents one case of a flight track across a train of internal waves. Internal wave-induced oscillations in the HH imagery are much more pronounced than in the VV imagery even though the mean cross-section level in the VV image exceeds that in the HH image. In fact, Figures 13c and 13d show that $\sigma_o(\text{HH})$ often approaches the level of $\sigma_o(\text{VV})$ at the signature maxima and sometimes exceeds it at the higher incidence angle.

[30] On 9 August 2006, the plane and the ship both traversed the same internal wave train many times. The ship

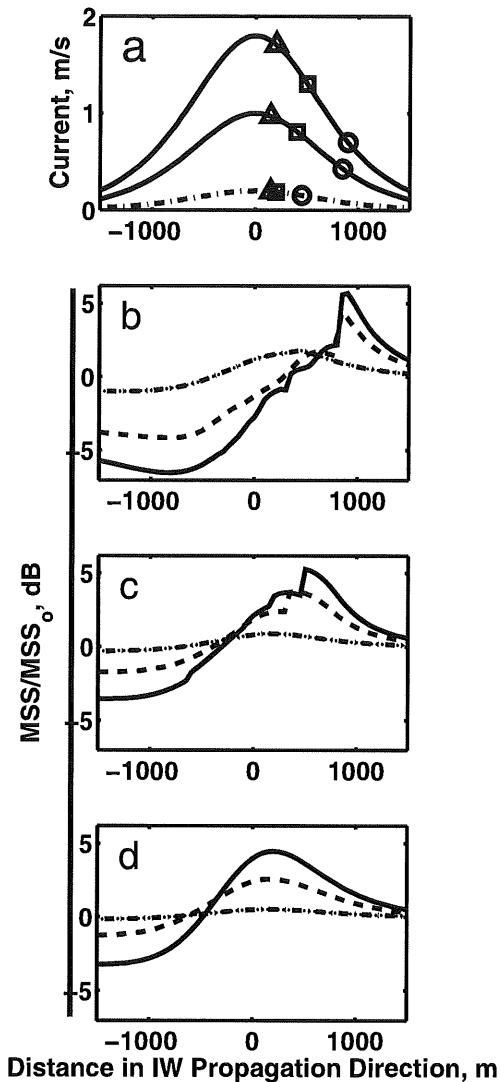


Figure 9. (a) Surface currents for internal waves of three different amplitudes with the positions of the maximum mean square slope of short-gravity waves between 24 and 400 cm long as predicted by action balance equations shown as circles. (b) Mean square slope (mss) of short-gravity waves between 24 and 400 cm long relative to the corresponding mean square slope of a wavefield undisturbed by IW currents for the three different solitary wave currents shown in Figure 9a. The wind velocity is 4 m/s in the direction of IW propagation. (c) Same as Figure 9b, but wind now blows perpendicular to the IW propagation direction. (d) Same as Figure 9b, but wind now blows opposite to the IW propagation direction. Triangles in Figure 9a show the positions of the maxima of the curves in Figure 9d, squares show the maxima of the curves in Figure 9c, and circles show the maxima of the curves in Figure 9b.

traveled either against the internal wave or with it while the plane flew in many different compass directions. We were therefore able to determine the maximum NRCS produced by the internal wave looking both up-wave and down-wave at a variety of incidence angles at nearly the same time.

Figure 14 shows the average of the maximum NRCS values for both HH and VV polarizations produced by the internal waves when the antennas looked upwave (Figures 14b, 14d, 14f, and 14h) and down-wave (Figures 14a, 14c, 14e, and 14g). The antennas generally looked near the crosswind direction for these measurements. Therefore, we also show in Figure 14 the crosswind NRCS values predicted by the multiscale model [Plant, 2002] for a sea surface disturbed only by the wind. These curves are the same in the left and right columns since these columns are the same in the absence of internal waves. We have not shown multiscale predictions in Figures 14a and 14b since at these low wind speeds, model predictions depend not only on the wind speed but also on its variability. This latter quantity was difficult to estimate.

[31] Several conclusions can be drawn from Figure 14. Clearly, maximum σ_o values of internal wave signatures are much closer to multiscale predictions for VV polarization than for HH. This agrees with the less distinct internal wave signatures for VV than for HH that we have pointed out above. There is some tendency for maximum $\sigma_o(VV)$ to trend closer to the multiscale predictions at higher wind speeds and incidence angles. This suggests that internal wave signatures at VV polarization should be relatively difficult to detect under these circumstances in agreement with Figure 11. Maximum $\sigma_o(HH)$ values of internal wave signatures are much higher than the values predicted by the multiscale model, being close to or above $\sigma_o(VV)$. This model does not include wave breaking and we believe that breaking waves are the most likely source of the enhanced backscatter at HH polarization at the maxima of the internal wave signatures. This interpretation is supported by the observation that in the shipboard data, $\sigma_o(HH)$ is 5 to 10 dB higher than $\sigma_o(VV)$. We cannot rule out the possibility that wave breaking also plays a role in increasing $\sigma_o(VV)$ at signature maxima.

[32] The flights of the Skymaster over all internal waves we viewed near the shelf break showed that there is very little tendency for the signature of the internal waves to vary depending on antenna look direction at moderate incidence angles. We use two different measures of the intensity of the microwave surface signature of internal waves. One measure is the ratio of the standard deviation to the mean cross section at constant incidence angles. Time series of cross section from which means and standard deviations were obtained were shown in Figures 13c and 13d. The other measure of intensity is the RMS variance level of the image spectra derived from detrended σ_o images. Figure 15 shows that neither of these measures of intensity varies significantly with azimuth angle. Note once again that internal wave signatures are more distinct in HH backscatter than in VV.

[33] Finally, in Figure 16, we show these same measures of intensity as a function of wind speed for all the data that we collected from the plane. As is well known, IW signatures become less distinct as the wind speed increases, and Figure 16 confirms this. We find that the signatures have nearly disappeared at a wind speed of 9 m/s.

4. Conclusions

[34] We have shown not only that microwave signatures of internal waves are more distinct at HH polarization than at VV, but also that maximum $\sigma_o(HH)$ values are comparable

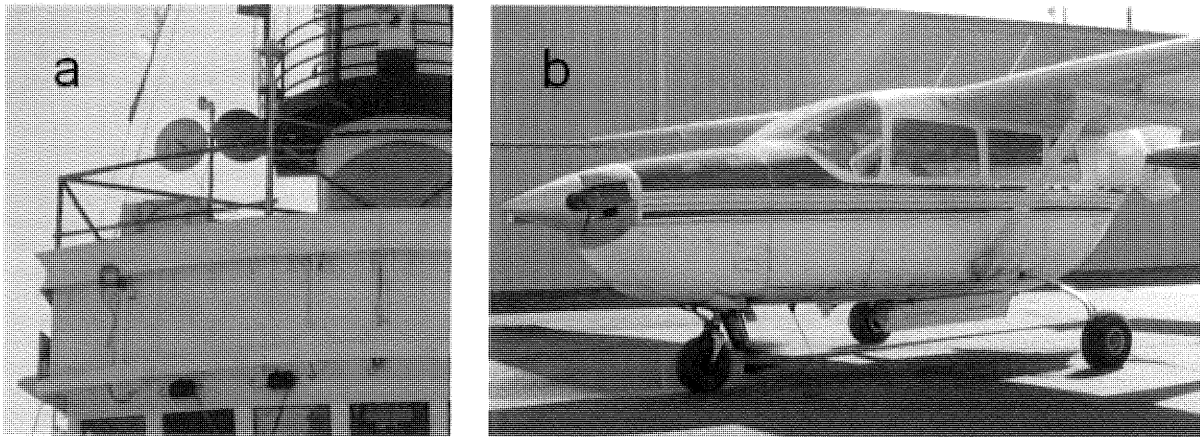


Figure 10. (a) RiverRad mounted on the R/V *Endeavor* in 2006 (the parabolic antennas). (b) CORAR mounted on the Cessna Skymaster at the same time (the white rectangular antennas under the fuselage).

to or even greater than maximum $\sigma_o(VV)$ values induced by the internal waves. The maximum $\sigma_o(HH)$ values produced by internal wave surface disturbances are much larger than the multiscale model predicts while maximum $\sigma_o(VV)$ values are comparable to or above the predicted values. Furthermore, the intensities of the signatures at both polarizations vary little with the direction of antenna look. All of these results suggest to us that breaking waves play a significant role in the production of microwave signatures by

internal waves. The many ways that this could happen were outlined in part 1 [*Plant et al., 2010*].

[35] The maximum of the microwave surface signature leads the maximum near-surface velocity of the internal wave by larger distances for steeper internal waves. This same behavior is seen in simulations of the location of the maximum modulation of short-gravity waves by internal waves using standard action balance techniques. These observations strongly suggest that microwave signatures of

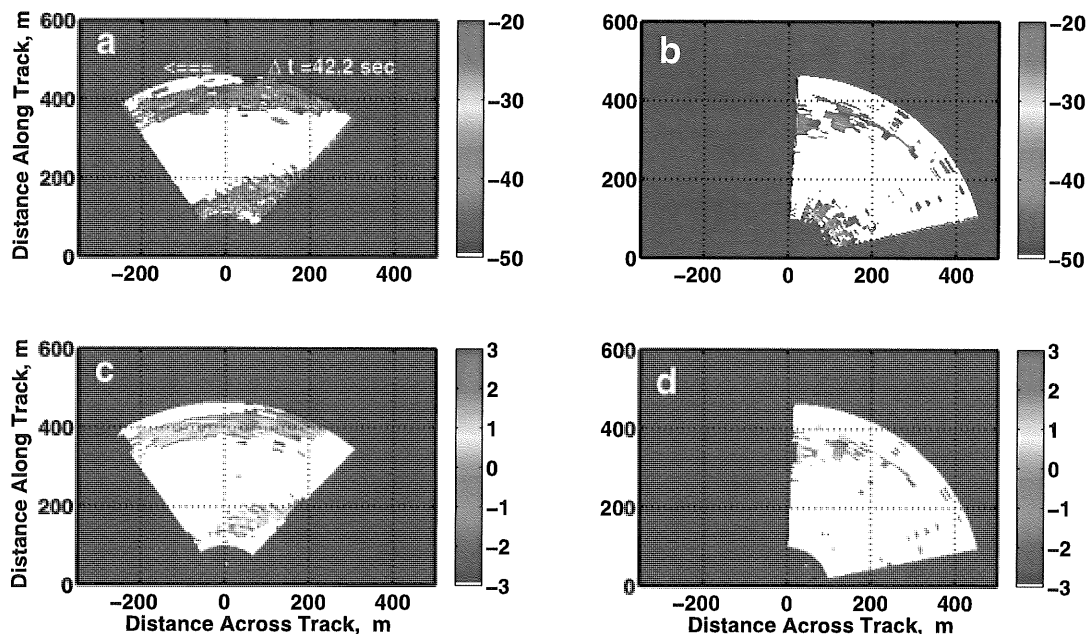


Figure 11. Images of microwave surface signatures of internal waves collected in 2006 from the R/V *Endeavor*. (a) $\sigma_o(HH)$, (b) $\sigma_o(VV)$, (c) scatterer velocities at HH, and (d) scatterer velocities at VV. The arrow in Figure 11a shows the direction of antenna rotation, and Δt is the time for the antennas to sweep out the displayed arcs. Normalized radar cross-section scales are in decibels; velocity scales are in m/s. Positive velocities are toward the radar. White regions show where the signal-to-noise ratio was too low to determine reliable σ_o or velocity values. Wind speed was 1.9 m/s, wind direction was $42^\circ T$, ship speed was 3 m/s, and ship heading was $146^\circ T$.

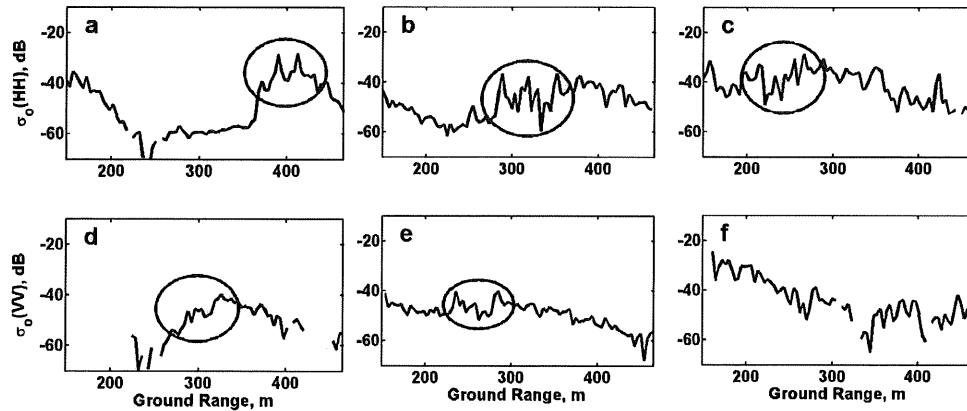


Figure 12. Average cross section versus ground range for data taken within 20° of the ship's heading. The circled areas show surface waves near the front face of the internal wave that are being amplified by the internal wave currents. (a) $\sigma_o(\text{HH})$ observed with wind speed of 1.9 m/s, wind direction relative to the ship heading of 104° , and ship speed of 3.0 m/s. (b) $\sigma_o(\text{HH})$ observed with wind speed of 3.3 m/s, wind direction relative to the ship heading of 73° , and ship speed of 3.2 m/s. (c) $\sigma_o(\text{HH})$ observed with wind speed of 6.0 m/s, wind direction relative to the ship heading of 118° , and ship speed of 3.5 m/s. (d) Same as Figure 12a but for $\sigma_o(\text{VV})$. (e) Same as Figure 12b but for $\sigma_o(\text{VV})$. (f) Same as Figure 12c but for $\sigma_o(\text{VV})$.

large internal waves are produced by the breaking of short-gravity waves as they are modulated by the internal waves in addition to the straining of wind waves by these short-gravity waves. In fact, in our shipboard measurements off the New Jersey coast, we observed cross-section oscillations

15 to 30 m in length that were modulated by the internal waves.

[36] Most of the microwave signatures observed in our low-grazing-angle measurements consisted of increases of the normalized radar cross section by the internal waves. A

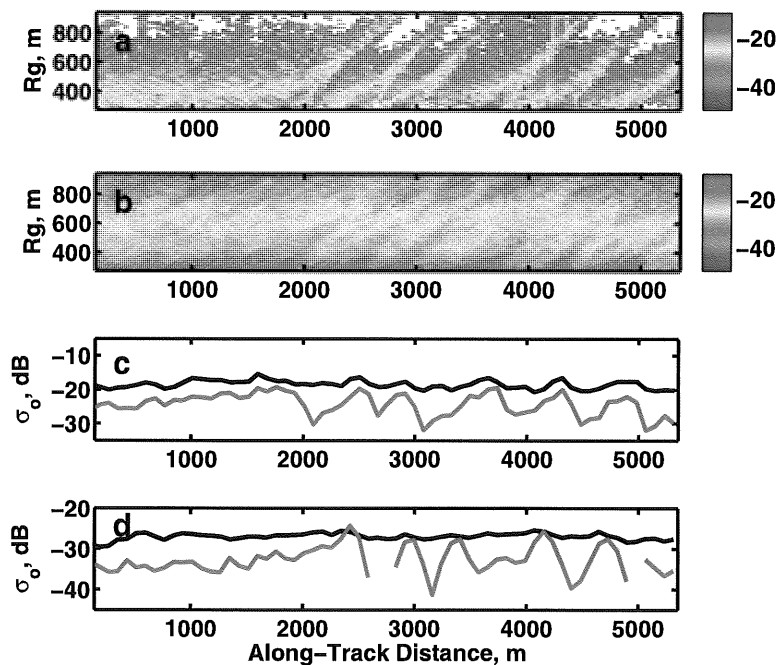


Figure 13. Normalized radar cross-section measurements of the sea taken from the Cessna Skymaster. (a) Image of $\sigma_o(\text{HH})$. The antenna was directed vertically, along the ground range; distance along the flight track is horizontal. (b) Same as Figure 13a but for $\sigma_o(\text{VV})$. (c) Cuts through $\sigma_o(\text{HH})$ and $\sigma_o(\text{VV})$ image at a constant incidence angle of 45° . (d) Same as Figure 13c but at a 65° incidence angle. For Figures 13a–13d, the flight track was along 82°T , while the internal wave traveled toward 320°T .

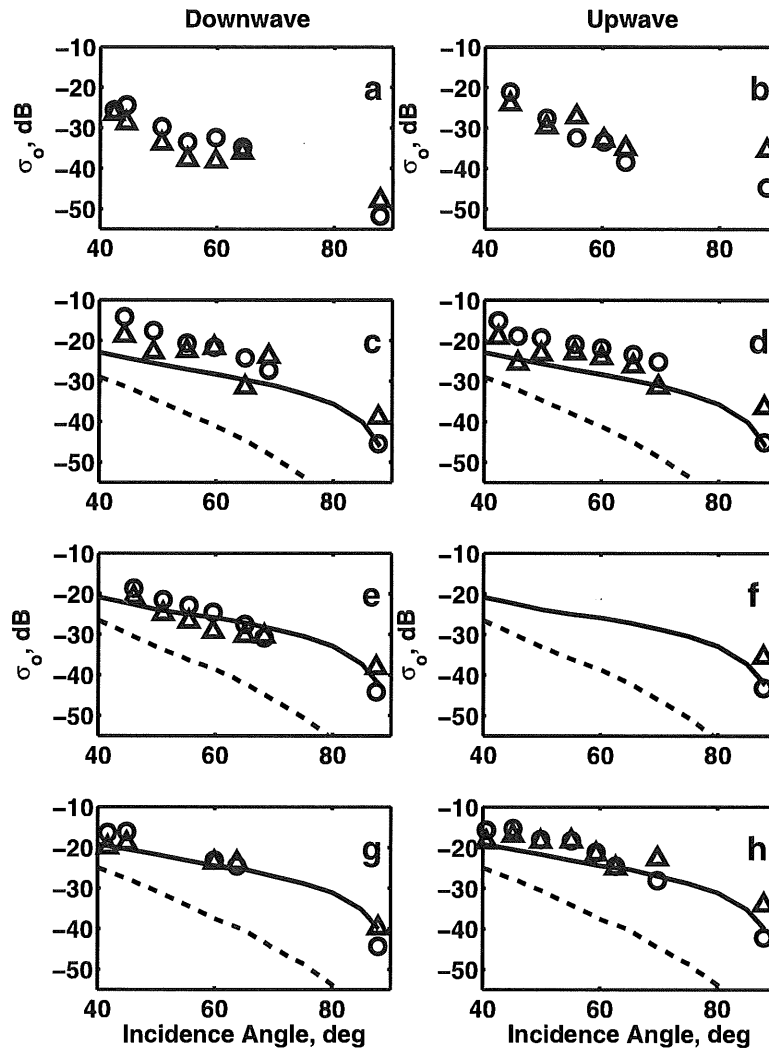


Figure 14. (a–h) Maximum NRCS values of the microwave signature modulated by an internal wave train as a function of incidence angle. Data in Figures 14a, 14c, 14e, and 14g were collected when the antennas looked along the internal wave’s propagation direction; data in the Figures 14b, 14d, 14f, and 14h were obtained with the antenna looking into the internal wave. The lines are predictions of the multiscale model of *Plant* [2002] for a sea surface disturbed only by wind averaged over azimuth angles between 45° and 135°, the range encountered in the present experiment. Solid curves and circles refer to VV polarization; dashed curves and triangles refer to HH. Wind speeds are between 1 and 2 m/s for Figures 14a and 14b, between 4 and 6 m/s for Figures 14c and 14d, between 5 and 6 m/s for Figures 14e and 14f, and between 6 and 7 m/s for Figures 14g and 14h.

few observations of increases followed by decreases were also recorded. We did not observe cases consisting only of a decreased cross section. We note that our simulations of short-gravity wave modulation by internal waves always showed increased short-gravity-wave mean squared slopes followed by decreases. However, many times the decreases were very small and may not have produced changes in σ_0 that our measurements could detect. *da Silva et al.* [1998] have reported seeing microwave surface signatures of internal waves from satellites at much lower incidence angles that consisted of cross section increases, decreases, and paired increases and decreases. They associated the first type of signature with low-wind conditions where the decrease is

not visible owing to system noise. This was not the case in our low-grazing-angle study. Our signal-to-noise ratio was usually sufficiently high that decreased cross sections were not hidden by noise.

[37] The movement of the NRCS maximum down the front face of the internal soliton as the wave steepened probably explains the results of *Kropfli et al.* [1999] that NRCS maxima generated by sinusoidal internal waves trains lie near the minima of the surface currents generated by the IW. Their quoted IW phase speeds are 0.7 to 0.9 m/s while the maximum currents 4.4 m below the surface appear to be less than 0.7 m/s and the time required for an IW to pass a fixed point is about 0.1 h (full width at half max). Thus one

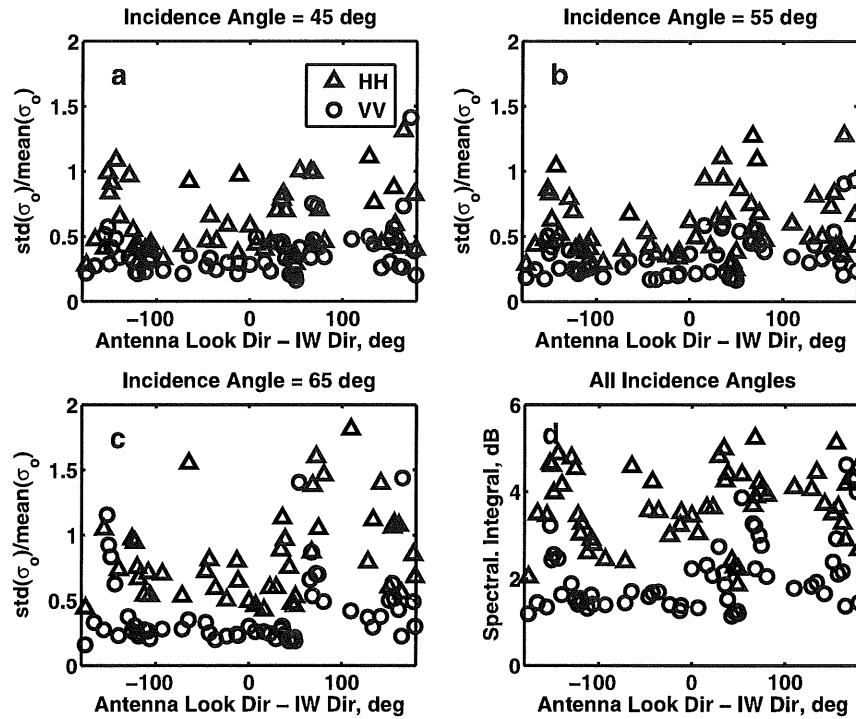


Figure 15. Measurements of the intensity of the internal wave microwave signature for various antenna look directions. (a) The ratio of the standard deviation to the mean cross section of the IW train at an incidence angle of 45°. (b) Same as Figure 15a but for a 55° incidence angle. (c) Same as Figure 15a but for a 65° incidence angle. (d) The RMS value of the image spectrum. This is necessarily calculated over the range of incidence angles that formed the image.

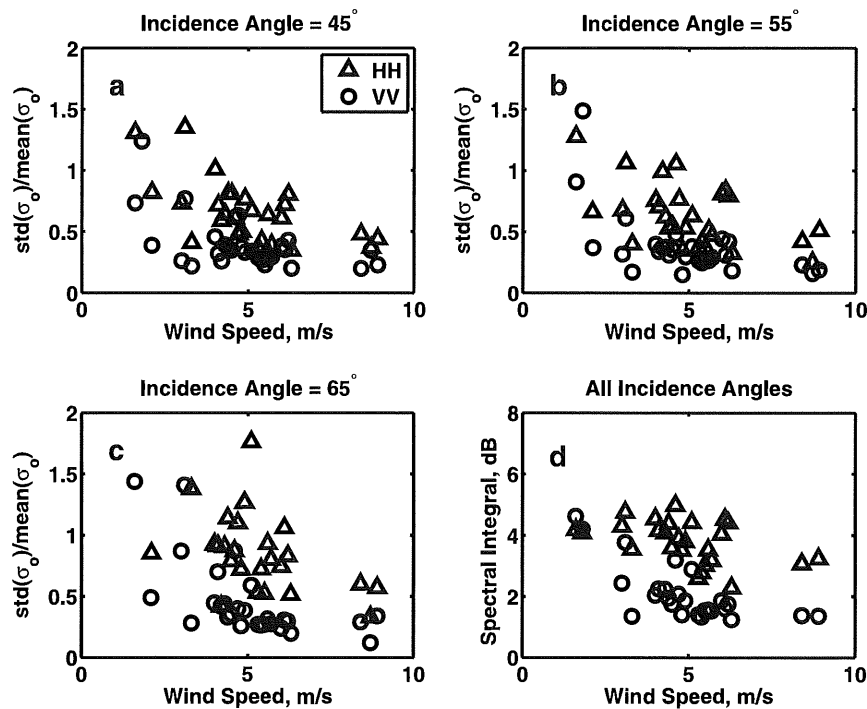


Figure 16. Dependence of the intensity of internal wave signatures on wind speed. (a-d) The same dependent variables as those in Figure 15.

thousand times the ratio of surface current to width, our measure of maximum strain rate, is about 2.8 1/s or a bit higher than the highest found in this study. Since wind directions generally had a significant component perpendicular to the IW propagation direction during the study, this implies that their modulation pattern should lead the IW current by nearly the width of the internal wave putting it nearly out of phase with a sinusoidal current. We were not able to verify this for the sinusoidal waves we observed off the New Jersey coast because the radar measurements and ADCP measurements did not overlap.

[38] Much additional information is available in this data set and is being studied. In particular, we are able to obtain the speeds of the internal waves from plots such as those shown in Figures 2 and 3. We are investigating these speeds and comparing them with predicted nonlinear wave speeds. Finally, we have not yet processed our data to yield the velocity spread within each range cell. This would aid in the identification of breaking-wave events and will be undertaken.

[39] **Acknowledgments.** We are grateful to Jody Klymak, Ren-Chieh Lien, and Cho-Teng Liu for providing us with processed ADCP data. We thank our pilots on the Skymaster, John Ambroult and John Williams of Ambroult Aviation, for safely flying us far offshore in the small aircraft and returning us to land. The crews of the three ships did an excellent job and are gratefully acknowledged. This work was supported by ONR grants N00014-05-1-0244, N00014-08-1-0977, and N00014-10-10318.

References

- Alpers, W. (1985), Theory of radar imaging of internal waves, *Nature*, *314*, 245–247, doi:10.1038/314245a0.
- Alpers, W., and E. Salusti (1983), Scylla and Charybdis observed from space, *J. Geophys. Res.*, *88*(C3), 1800–1808, doi:10.1029/JC088iC03p01800.
- Apel, J. R. (2004), Oceanic internal waves and solitons, in *Synthetic Aperture Radar Marine User's Manual*, edited by C. R. Jackson and J. R. Apel, pp. 189–206, U.S. Dep. of Commer., Washington, D. C.
- Apel, J. R., H. M. Byrne, J. R. Prom, and R. L. Chamell (1975), Observations of oceanic internal and surface waves from the Earth Resources Technology Satellite, *J. Geophys. Res.*, *80*(6), 865–881, doi:10.1029/JC080i06p0865.
- Brandt, P., W. Alpers, and J. O. Backhaus (1996), Study of the generation and propagation of internal waves in the Strait of Gibraltar using a numerical model and synthetic aperture radar images of the European ERS 1 satellite, *J. Geophys. Res.*, *101*(C6), 14,237–14,252, doi:10.1029/96JC00540.
- Brandt, P., A. Rubino, W. Alpers, and J. O. Backhaus (1997), Internal waves in the Strait of Messina studied by a numerical model and synthetic aperture radar images from the ERS 1/2 satellites, *J. Phys. Oceanogr.*, *27*, 648–663, doi:10.1175/1520-0485(1997)027<0648:IWITSO>2.0.CO;2.
- Chang, M. H., R. C. Lien, Y. J. Yang, T. Y. Tang, and J. Wang (2008), A composite view of surface Signatures and interior properties of nonlinear internal waves: observations and applications, *J. Atmos. Oceanic Technol.*, *25*, 1218–1227, doi:10.1175/2007JTECHO574.1.
- Churyumov, A. N., Y. A. Kravtsov, O. Y. Lavrova, K. T. Litovchenko, M. I. Mityagina, and K. D. Sabinin (2002), Signatures of resonant and non-resonant scattering mechanisms on radar images of internal waves, *Int. J. Remote Sens.*, *23*(20), 4341–4355, doi:10.1080/01431160110107644.
- da Silva, J. C. B., S. A. Ermakov, I. S. Robinson, D. R. G. Jeans, and S. V. Kijashko (1998), Role of surface films in ERS SAR signatures of internal waves on the shelf 1. Short-period internal waves, *J. Geophys. Res.*, *103*(C4), 8009–8031, doi:10.1029/97JC02725.
- Hogan, G. G., R. D. Chapman, G. Watson, and D. R. Thompson (1996), Observations of ship-generated internal waves in SAR images from Loch Linnhe, Scotland, and comparison with theory and in situ internal wave measurements, *IEEE Trans. Geosci. Remote Sens.*, *34*(2), 532–542, doi:10.1109/36.485129.
- Hughes, B. A., and T. W. Dawson (1988), Joint Canada-U.S. Ocean Wave Investigation Project: An overview of the Georgia Strait Experiment, *J. Geophys. Res.*, *93*(C10), 12,219–12,234, doi:10.1029/JC093iC10p12219.
- Hughes, B. A., and R. F. Gasparovic (1988), Introduction, *J. Geophys. Res.*, *93*(C10), 12,217, doi:10.1029/JC093iC10p12217.
- Hughes, B. A., and H. L. Grant (1978), Effect of internal waves on surface wind waves: 1. Experimental measurements, *J. Geophys. Res.*, *83*(C1), 443–454, doi:10.1029/JC083iC01p0443.
- Hwang, P., M. A. Sletten, and J. V. Toporkov (2008), Breaking wave contribution to low grazing angle radar backscatter from the ocean surface, *J. Geophys. Res.*, *113*, C09017, doi:10.1029/2008JC004752.
- Kropfli, R. A., L. A. Ostrovski, T. P. Stanton, E. A. Skirta, A. N. Keane, and V. Irisov (1999), Relationships between strong internal waves in the coastal zone and their radar and radiometric signatures, *J. Geophys. Res.*, *104*(C2), 3133–3148, doi:10.1029/98JC02549.
- Kudryavtsev, V., D. Akimov, J. Johannessen, and B. Chapron (2005), On radar imaging of current features: 1. Model and comparison with observations, *J. Geophys. Res.*, *110*, C07016, doi:10.1029/2004JC002505.
- Liu, A. K., C.-R. Ho, and C.-T. Liu (2008), *Satellite Remote Sensing of the South China Sea*, 312 pp., Tingmao, Taipei.
- Liu, Y., S. J. Frasier, and R. E. McIntosh (1998), Measurement and classification of low-grazing-angle radar sea spikes, *IEEE Trans. Geosci. Remote Sens.*, *46*(1), 27–40.
- Lyzenga, D. R., and J. R. Bennett (1988), Full-spectrum modeling of synthetic aperture radar internal wave signatures, *J. Geophys. Res.*, *93*(C10), 12,345–12,354, doi:10.1029/JC093iC10p12345.
- Plant, W. J. (1997), A model for microwave Doppler sea return at high incidence angles: Bragg scattering from bound, tilted waves, *J. Geophys. Res.*, *102*(C9), 21,131–21,146, doi:10.1029/97JC01225.
- Plant, W. J. (2002), A stochastic, multiscale model of microwave backscatter from the ocean, *J. Geophys. Res.*, *107*(C9), 3120, doi:10.1029/2001JC000909.
- Plant, W. J., E. A. Terray, R. A. Pettit Jr., and W. C. Keller (1994), The dependence of microwave backscatter from the sea on illuminated area: Correlation times and lengths, *J. Geophys. Res.*, *99*(C5), 9705–9723, doi:10.1029/93JC00862.
- Plant, W. J., W. C. Keller, and K. Hayes (2005a), Simultaneous measurement of ocean winds and waves with an airborne coherent real aperture radar, *J. Atmos. Oceanic Technol.*, *22*, 832–846, doi:10.1175/JTECH1724.1.
- Plant, W. J., W. C. Keller, and K. Hayes (2005b), Measurement of river surface currents with coherent microwave systems, *IEEE Trans. Geosci. Remote Sens.*, *43*(6), 1242–1257, doi:10.1109/TGRS.2005.845641.
- Plant, W. J., W. C. Keller, K. Hayes, and G. Chatham (2010), Normalized radar cross section of the sea for backscatter: 1. Mean levels, *J. Geophys. Res.*, *115*, C09032, doi:10.1029/2009JC006078.
- Ramamonjiarisoa, A. (1995), On the kinematics of short waves in the presence of surface flows of larger scales, *J. Fluid Mech.*, *298*, 249–269, doi:10.1017/S0022112095003296.
- Thompson, D. R. (1988), Calculation of radar backscatter modulations from internal waves, *J. Geophys. Res.*, *93*(C10), 12,371–12,380, doi:10.1029/JC093iC10p12371.
- Thompson, D. R., and R. F. Gasparovic (1986), Intensity modulation in SAR images of internal waves, *Nature*, *320*, 345–348, doi:10.1038/320345a0.

G. Chatham, K. Hayes, W. C. Keller, N. Lederer, and W. J. Plant, Applied Physics Laboratory, University of Washington, 1013 NE 40th St., Seattle, WA 98105-6698, USA. (plant@apl.washington.edu)

Optical and Microwave Detection of Wave Breaking in the Surf Zone

Patricio A. Catalán, Merrick C. Haller, Robert A. Holman, and William J. Plant, *Member, IEEE*

Abstract—Synchronous and colocated optical and microwave signals from waves in the surf zone are presented and analyzed. The field data were collected using a high-resolution video system and a calibrated horizontally polarized marine radar during the decaying phase of a storm. The resulting changes in the received signals from varying environmental conditions were analyzed. The analysis of the optical signal histograms showed functional shapes that were in accordance with the expected imaging mechanisms from the breaking and nonbreaking waves. For the microwave returns, the histogram shape showed a little dependence on the environmental parameters and exhibited an inflexion point at high returned power that is attributed to a change in the scattering mechanism. The high intensity signals were clearly associated with active wave breaking. However, with either sensor, it can be difficult to effectively isolate the wave breaking signature from other sources, such as a remnant foam or the highly steepened nonbreaking waves. A combined method was developed using the joint histograms from both sensors, and it is shown to effectively discriminate between active breaking, remnant foam, and steepened waves. The new separation method allows a further analysis of the microwave scattering from the breaking waves and a better quantification of the length scales of the breaking wave roller and the spatial/temporal distribution of wave breaking and wave dissipation in the surf zone.

Index Terms—Nearshore, optical imaging, radar, remote sensing, sea surface, surface waves, wave breaking.

I. INTRODUCTION

OBSERVATIONS of the location and frequency of the occurrence of wave breaking are important in improving our understanding and predictive capabilities of nearshore hydrodynamics. Wave breaking leads to a transfer of momentum that is the dominant driver of surfzone currents and is also important for the resuspension and transport of sediments. The wave breaking roller is the physical structure generated in the breaking process, and it consists of a turbulent body of air and

water that develops on and propagates with the front face of a surfzone wave. The roller can be a dominant factor in the surfzone mass balance and in the generation of cross-shore currents [1]. In general, wave breaking exhibits a significant spatial and temporal variability that is difficult to observe and accurately predict in detail.

For example, models for nearshore hydrodynamics require a description at some level of wave breaking quantities, such as the onset of breaking, the fraction of the breaking waves, and the probability distribution of the breaking wave heights. These quantities appear in wave models of all types—parametric wave evolution models [2]–[4], third generation spectral models [5], or models that are based on the mild slope equation [6], and they are needed in order to quantify the wave dissipation and to calculate the additional quantities of the momentum transfer. In addition, other work has shown that the physical scales of the wave roller are directly related to dissipation [7], [8]. Therefore, the observations of the wave roller physical scales and the spatial/temporal distribution of wave breaking will support improvements in both our understanding of wave breaking statistics and the relationship between roller-related quantities and dissipation models.

However, the proper identification of wave breaking is a difficult task. Somewhat loosely defined as the transformation of organized wave energy into other energy states (turbulence, heat, and sound), wave breaking is not simply quantifiable. Some single-point methods exist [9], but the synoptic remote sensing approaches are best suited in identifying the space/time variability of the wave breaking occurrence. Furthermore, wave breaking signatures are usually very prominent in a number of different remote sensing modalities. Some examples are the following: acoustic [10], [11], optical [12], [13], infrared [14], [15], and microwave [16], [17]. Nonetheless, other phenomena can still contaminate the signal, causing difficulties in the accurate discrimination of breaking from other phenomena. For example, in the surf zone, the locations of preferential breaking are correlated with the increased mean intensity values of a series of optical images [18] or microwave images [19], [20], but these results can be affected by the presence of persistent foam or steepening waves, respectively.

Time exposures or the map of the temporal mean of the signal corresponds to the most basic statistical measure that can be used to discriminate between the breaking and nonbreaking waves. However, the probability density functions (pdfs) and the cumulative density functions of the time-varying signals encapsulate a higher level of information. The pdf approach has been used, for instance, in microwave-based maritime surveillance and target detection [21], [22] but only recently with

Manuscript received June 2, 2010; revised October 26, 2010; accepted November 16, 2010. Date of publication January 5, 2011; date of current version May 20, 2011. This work was supported in part by the Office of Naval Research under award numbers N00014-06-1-0317, N00014-08-1-0636, and N00014-07-1-0490 and in part by FONDECYT under award number 11090201.

P. A. Catalán is with the Departamento de Obras Civiles, Universidad Santa María, Valparaíso 110-V, Chile (e-mail: patricio.catalan@usm.cl).

M. C. Haller is with the School of Civil and Construction Engineering, Oregon State University, Corvallis, OR 97331 USA.

R. A. Holman is with the College of Oceanic and Atmospheric Sciences, Oregon State University, Corvallis, OR 97331 USA.

W. J. Plant is with the Applied Physics Laboratory, University of Washington, Seattle, WA 98105 USA.

Digital Object Identifier 10.1109/TGRS.2010.2095864

optical data [23]. In addition, there is some previous work examining simultaneous signals in optical and microwave sensors [17], [24], [25]. However, the procedures for wave breaking identification have been fairly qualitative, and a high level of uncertainty persists. In the present work, our objective is to improve our understanding of both the optical and microwave signals arising from different sources in the surf zone, with the overarching goal of obtaining improved identification and measurements of breaking events on a wave-by-wave basis.

II. IMAGING OF THE OCEAN SURFACE

In the open ocean, wave breaking takes place over a wide range of temporal and spatial scales: from individual micro-breaking events that produce small amounts of bubbles, turbulence, and spray but do not produce a strong optical signature (i.e., turbulent whitewater or foam) to larger scale events that are optically bright. In the following, we define these larger events as the signal of interest, and their imaging characteristics will be sensor dependent. We focus here on the occurrence and identification of these large events because they are a dominant process in surfzone hydrodynamics.

A. Optical

Optical sensing systems measure the radiance reaching the sensor at wavelengths in the visible band. The source is the sun irradiance that is being reflected by the ocean surface after being absorbed and diffused by the atmosphere, while the upwelling and direct sun radiances are often neglected. For the nonbreaking waves, the first approximation assumes the sky radiance to be isotropic and homogeneous, which leads to the observed radiance that is being dependent solely on the Fresnel reflection coefficient R . R , in turn, can be related to the surface slope of the ocean s . The relationship between R and the surface slope is nonlinear, and it exhibits a strong asymmetry between positive (surface normal pointing toward the camera) and negative slopes. The latter has a stronger dependence, which means that small variations in negative slope yield significant variations in R and, therefore, the radiant intensity [26]. However, if the slopes are small ($s < 20^\circ$), the relationship can be treated as linear [27].

The breaking waves depart from this specular reflection model in that the radiance depends on the diffuse reflectivity from the whitecap [28]. The radiometric whitecap measurements in the surf zone have shown that the foam-covered areas have a large albedo and reflect about one order of magnitude more than the foam-free areas [29]. Furthermore, the time histories of the passage of the breaking waves indicate sharp increases in reflectance in finite time, followed by an exponential decay.

In general, it is this large difference between the observed reflectivity of the bubbly and nonbubbly surfaces that is exploited to identify the whitecaps. However, most applications do not attempt to discriminate between active breaking and remnant foam, although some attempts have been made using subjective thresholds [30], [31], fractal representations of the intensity signal [32], or an approach based on wave kinematics [23].

A review of the existing methodologies for identifying active wave breaking in optical data shows that most separation methods have been developed for deep water whitecaps and that radiometric studies are rare [8]. Instead, usually the analyzed quantity is an uncalibrated image intensity, henceforth denoted as I . Therefore, the discrimination procedure between breaking and nonbreaking image portions is often carried out using relative intensity thresholds, in which pixels with intensities above a given threshold are attributed to the whitecaps. However, the overall image brightness can vary, owing to the changes in the environmental and experimental conditions. The environmental effects include the changes in the sun's zenith and the variations of the cloud coverage, for instance. The experimental effects include the differences in camera looking angles and the changes in camera aperture and shutter speed. As a consequence, no universal rule exists, and the threshold is data set specific and, in some cases, is allowed to vary between images [30], [33]. Recently, a few image processing algorithms have been proposed to reduce the subjectivity in threshold determination and to improve automation [13], [23], [34].

The use of these methods is not straightforward in the surf zone mainly due to the increased levels of breaking frequency and the persistence of the remnant foam, which can last several wave periods. Despite the presence of foam, to date, the main procedure that is used to denote zones of preferential breaking involves the use of time exposures where the contributions of the wave roller and remnant foam are intermingled. *Aarninkhof* and *Ruessink* [35] developed a procedure that is used to remove the foam contribution from the mean intensity image (or time exposure) during postprocessing by introducing a model for the decay of the intensity signal, but a separation methodology applicable on a wave-by-wave basis does not yet exist.

The mean and standard deviation of the intensity represent the basic level of characterization given by the lower order moments of the time-varying signal. However, the pdf yields more information. Although the optical pdf has not been previously described for the surf zone, the direct relationship between the observed radiance and the surface slopes for the nonbreaking waves [28] can be exploited. In deep water, the sea surface slope is best described as a Gaussian process whose pdf is described as the product of two Gaussian distributions, which is dependent on the co-wind and cross-wind slopes, respectively [28], [36]. Therefore, it can be expected that the pdf of the radiance would also be Gaussian distributed to first order. It must be noted that this is true only for relatively smooth surfaces (thus small slopes). For the wave fields with steeper slopes, the pdf would show a steep increase at low intensities, followed by an exponential-like decay [28]. However, in the shoaling region, the occurrence of nonlinear, asymmetric, or skewed waves can also lead to the distribution to depart from Gaussian.

The pdf of a broken wave, in turn, will depend on the duration and spatial extent of the breaker and foam coverage. For instance, the deep water whitecap life span exhibits a probability distribution that is almost exponential [28]. This departure from the expected Gaussian distribution of the nonbreaking waves has been used by *Mironov* and *Dulov* [23] to discriminate between wave breaking stages in deep water. In the surf zone,

Aarninkhof and *Ruessink* [35] introduced a model relating the time series of the optical intensity to the wave period T and a parameter that is related to foam persistence (λ). A pdf can be derived for this model

$$p(I) = \frac{1}{\lambda I} \quad (1)$$

where I is defined in the interval between a background level I_0 and the peak intensity $I_0 + \Delta I_b$. It can be seen that the pdf also resembles an exponential decay which is governed by foam persistence. However, this simple model does not take into account the spatial extent of the wave roller, and it also assumes that the brightest point will be located at the wave roller front. *Haller* and *Catalán* [8] used high-resolution optical data in the laboratory and showed that the brightest point is collocated with the wave crest, which is followed by a region of approximately constant high intensity values. The effect of those on the pdf will be a departure of the exponential decay, with a secondary peak at high intensity values. Finally, in the surf zone, the signal will usually be the result of a mixture of the breaking and nonbreaking waves. Therefore, the resulting radiance will be the sum of the area-weighted contributions arising from the breaking and nonbreaking areas [37]. In consequence, the pdfs are expected to be a combination of two exponential-like processes at different intensity ranges. However, the intensity threshold at which one process dominates cannot be determined beforehand.

B. Microwave

At moderate incidence angles ($\theta = 20^\circ$ – 70°), the microwave returns from the ocean surface are explained by Bragg scattering and the composite surface theory (CST) [38], [39], in which the ocean is modeled as a continuum of sloped facets whose extent is small compared to the (long) ocean waves but larger than the Bragg waves. The resulting scattering is then the modulation of the Bragg scattering by the long waves.

However, many observations show scattering signatures that are not consistent with Bragg scattering nor with the CST. These anomalies occur most often for active microwave sensors with low grazing angle (LGA) viewing geometries and include high intensity bursts of backscatter (sea spikes) [24], [25], [40], polarization ratios (HH/VV, where HH corresponds to horizontal transmit–horizontal receive and VV corresponds to vertical transmit–vertical receive) exceeding unity [22], [24], [41], [42], and a broadening of the Doppler spectrum and large Doppler offsets [43], [44]. The breaking waves have been often cited as the source for these anomalies, and the characteristics of the anomalies have been used for breaking wave detection. However, methods that are based on power thresholds lead to large false detection rates [16]. Usually, both breaking and steep unbroken waves are the source of observed sea spikes [25]. The polarization data have shown that the breaking waves exhibit ratios in the vicinity of one, but the polarization ratio alone was not considered to be a reliable discriminator [25]. However, a significant uncertainty still exists as others have assumed that polarization ratios exceeding unity suffice in discriminating the breaking events [42], [45].

In addition to the uncertainty regarding the relationship between the breaking waves and the scattering anomalies, the vast majority of previous studies use observations from deep water where the dynamics of breaking can be different from that in shallow water. In the surf zone, *Haller* and *Lyzenga* [17] used VV, X-band, and collocated video data and defined a spike as an event whose temporal excursion above the mean normalized radar cross section (NRCS) was longer than 0.2 s. They found out that 92% of the detected events corresponded to the optical breaking signatures identified by an observer. Moreover, their results indicated that the spikes were arising from the scattering from the active breaking region in front of the wave and that the remnant foam was a weaker scattering source, thus opening the possibility to discriminate between these states.

A good understanding of the statistical description of the scattered fields is needed for target detection applications, such as marine surveillance [21]. If the footprints are large and if uniform scatterers are distributed within it, the microwave amplitude will be Rayleigh distributed, and the power will be exponentially distributed [46]. The presence of spikes or high-resolution cells induce departures from purely exponential distributions, which have been modeled using compound models, combinations of Weibull distributions, or the K-distribution with varying levels of success [22], [46]–[50]. For instance, at LGA and HH, *Trizna et al.* [22], [51] found two distinct trends in the distribution, which they cite as evidence of two separate scattering mechanisms.

Here, we shall perform pdf and joint pdf (JPDF) analysis in order to develop a breaking wave identification method. First, we analyze the pdfs of data for each sensor in order to validate the conceptual scattering models presented in this section and their relation with the different stages of wave breaking. Next, we use the JPDF to develop a joint method, in which the different scattering characteristics between sensors and wave breaking stages are exploited to better identify the breaking events.

III. EXPERIMENTAL DATA

Nearshore remote sensing observations were collected over a six-week period between April 10 and May 22, 2008, at the U.S. Army Corp of Engineers Field Research Facility (FRF), Duck, NC. In the following, we utilize the FRF coordinate system where the cross-shore coordinate is denoted as x and points offshore, the y axis points roughly 18° west of north, and $z = 0$ correspond to NADV29. For the data analyzed herein, the shoreline was located at approximately $x = 90$ m in the FRF coordinate system. The data were collected using three remote sensors. The first one was a single polarization (HH) marine radar (Si-Tex RADARpc-25.9) operating at 9.45 GHz and attached to an independent data acquisition system (Imaging Science Research, Inc.). The radar antenna was mounted atop of a 10-m tower near the north end of the FRF facility ($x = 17.4$ m, $y = 971.4$ m, and $z = 13.8$ m; see Fig. 1). The marine radar is an active sensor with a 25-kW nominal power and a 9-ft open array antenna that rotates at approximately 44 r/min. Therefore, a point on the surface is sampled every 1.36 s (0.73 Hz). A pulse repetition

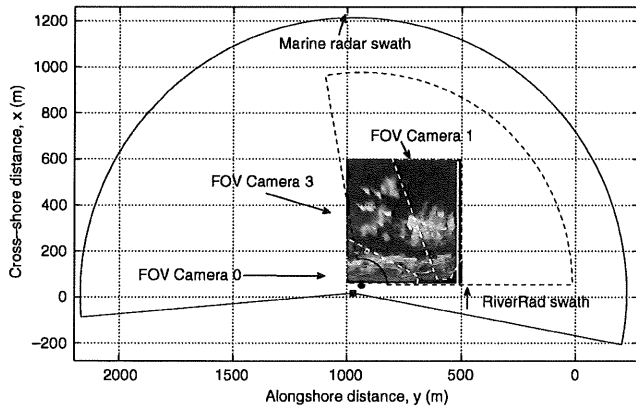


Fig. 1. Field of view of the sensors and sensor location. The circular sectors denote the swath covered by the marine radar (solid line) and RiverRad (dashed line), respectively. As the background, a merged image from the ARGUS III cameras is presented, with the white dashed lines denoting the boundaries between cameras. The vertical white at the $x = 516$ m line denotes the location of the FRF pier, and the solid square and circle denotes the location of the marine radar and RiverRad, respectively.

frequency of 2000 Hz was used along with a pulsewidth of 80 ns, resulting in an intrinsic range resolution of 12 m, although the data acquisition system internally oversamples, yielding a constant working range resolution of 3 m. The horizontal antenna beamwidth is 0.8° , and the vertical beamwidth is about 25° . Data acquisition was designed to average seven received waveforms, which reduced noise and decreased the azimuthal resolution to roughly 2° . Special care was taken to limit the saturation of the received signal by introducing an offset of -500 mV before processing by using the internal logarithmic amplifier. The recorded signal is then an uncalibrated grayscale intensity index $I_r(\theta, r, t)$. The acquisition system records the relative azimuth and time (accurate to 10 ms) of each sample, which enables geolocation and synchronization with the other sensors. The maximum recorded ground range was set to 1200 m, and the collections covered a swath of about 200° under nominal rotation speeds. Thirty-minute collections were recorded at the beginning of each hour throughout the duration of the experiment.

The second remote sensing system was comprised of three optical cameras from the ARGUS III observing station established at the FRF by the Coastal Imaging Laboratory, College of Oceanic and Atmospheric Sciences, Oregon State University (OSU). Further details of this system can be found in [12]. For the purpose of this experiment, a rectangular pixel array was designed, spanning $x = 60\text{--}600$ m and $y = 500\text{--}1000$ m, with a spatial resolution of $\Delta x = 2$ m and $\Delta y = 5$ m, using cameras 0, 3, and 1, as shown in Fig. 1. The optical (video) pixel intensity data $I(x, y, t)$ were collected simultaneously with the marine radar during daylight hours (seven runs of 31 min per day) at a sampling rate of 2 Hz.

The third sensor was RiverRad, which is an X-band (9.36 GHz) dual polarization (HH, VV) coherent radar developed by the Applied Physics Laboratory, University of Washington. It was deployed on the crest of the dune at the north end of the FRF property, at $x = 54.4$ m, $y = 936.2$ m, and $z = 10.2$ m. The data from this system were less synoptic than the others. The antennas were fixed in the staring mode at 10°

azimuthal increments for 2-min intervals. The total coverage was 80° in azimuth every 18 min. Further system details can be found in [52]. In the present work, the RiverRad data were only used for cross calibration to convert the marine radar data $I_r(\theta, r, t)$ to NRCSSs $\sigma_0(\theta, r, t)$. This step removes the system and range dependences that are irrelevant to the scattering dynamics, and it is an extension of the procedure presented in [53].

The analysis focuses on three collections labeled as Runs 9, 13, and 18, respectively, which occurred during a storm on May 12–16, 2008. As shown in Table I, the environmental conditions show a significant variability in three parameters, the significant wave height, wind speed, and wind direction. The wind direction changed from blowing onshore (upwind relative to the antennas) to offshore directed (downwind) for the last two runs. In addition, the combined effect of wind, tide level, and varying wave heights resulted in varying degrees of foaminess (see Fig. 2), which allows us to evaluate the effect of the remnant foam on the signals.

IV. DATA ANALYSIS

As stated previously, the data analysis will focus on the marine radar and optical systems. These two systems provide the largest synchronous surf zone coverage, and the duration of both time series allows the use of a large number of points to ensure a statistical significance. The time series is also short enough to ensure that the environmental conditions remained stable. We note that, although the radar scans the field of view in a finite time, for the present purpose, we treat the marine radar image as a snapshot of the surface. This should not be an issue, considering that the time required for the marine radar to scan through the area defined by the pixel array is $t \approx 0.3$ s. During this time, at a nominal wave speed of 10 m/s, waves would travel a distance shorter than a radar resolution cell. In addition, the scan through rate is less than the video sampling rate (0.5 s).

However, in order to analyze the synchronous instantaneous signals from the two sensors, the differences in sampling rates and spatial resolution need to be removed. This requires at least one of the sensors to be interpolated to a common domain. This is achieved in two steps. The first step involves the interpolation of the time domain of the video signal to the time domain of the marine radar, which is performed on a pixel-by-pixel basis using linear interpolation. The second step is the interpolation of the marine radar data to the higher resolution uniform grid defined by the video pixel array. Additionally, at the boundaries between the field of view of each camera, the differences in camera gain and integration time induce sharp gradients in the optical pixel intensity that is not related with the actual ocean surface. In order to minimize this effect, in the following, we group the data on a camera-by-camera basis, and we do not include the data near the camera boundaries.

In order to analyze the level of correlation between the time series of each sensor, the squared coherence γ^2 was calculated as

$$\gamma^2 = \frac{C_{O^2}(f) + Q_{U^2}(f)}{C_{MR}C_V} \quad (2)$$

TABLE I
SUMMARY OF THE WAVE CONDITIONS MEASURED AT THE 8-m ARRAY DURING THE STORM ON MAY 12–16, 2008, FOR THE THREE SELECTED RUNS.
THE RELATIVE (REL) DIRECTIONS ARE MEASURED CW WITH A 0° POINTING ALONG THE FRF x AXIS

Run #	Marine Run (yearday EST)	Time GMT	H_{m0} m	T_p s	Tide NAVD88 m	Wind Speed m/s	Wind Dir. ° TN (rel)	Wave Dir. ° TN (rel)
9	1341700	May 13-22:00	3.26	12.5	0.51	11.6	56 (-16)	56 (-16)
13	1351300	May 14-18:00	1.97	12.5	0.26	5.4	229 (157)	64 (-8)
18	1361000	May 15-15:00	1.47	11.4	-0.44	7.7	253 (181)	71 (-1)

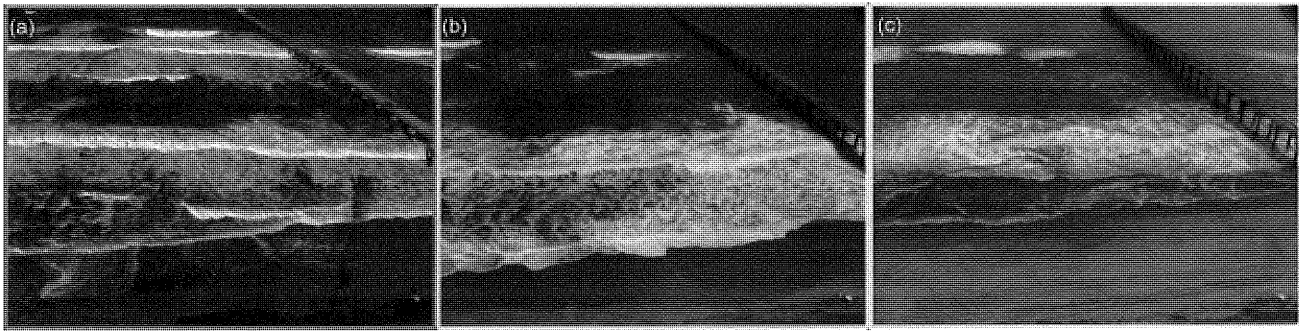


Fig. 2. Video snapshots taken from camera 1 for each of the three selected runs. (a) Run 9. (b) Run 13. (c) Run 18.

for every pixel within the field of view. Here, $Co(f)$ and $Qu(f)$ are the real (cospectrum) and imaginary (quad-spectrum) parts of the cross-spectrum, and C_{MR} and C_V are the marine radar and video pixel intensity autospectra [54]. Fig. 3 shows the time exposures from each sensor for each run (video in the top row and marine radar in the middle row). The bottom row shows the median γ^2 value within a window that is $\pm 5\%$ of the peak frequency of the ocean waves. In the time exposures, the zones of the preferential breaking correspond to areas where the average intensity (or power) is large, shown as brighter areas. As can be seen, the coherence levels are typically large for the majority of the field of view. Therefore, the signals are well correlated. The exceptions are bands of low coherence located on the seaward edges of the areas of preferential breaking. The presence of these bands is due to the intermittent change in the imaging mechanism for the video signal. For the nonbreaking waves, the imaging mechanism is specular reflection, and the local peak in intensity takes place toward the back of the wave where the local incidence angle is a minimum, whereas the wave fronts are dark. Once the waves break, the imaging mechanism in front of the wave changes to diffuse scattering that is due to the presence of the wave roller, and the signal becomes very bright. For the microwave sensor, the location of the peak power tends to be near the crest of the wave for both breaking and nonbreaking waves. As a consequence, there is a change in the phase between the microwave and video signals as the waves begin to break, which makes the two incoherent at locations where there is an intermittent breaking.

The time exposures show that, during the storm, on average, the waves were breaking near the shoreline and also over an outer bar. In order to differentiate the behavior of the signal between areas of persistent, intermittent, and sporadic breaking, we further divide each camera field of view into four areas, as shown in Fig. 4 and as defined in Table II. Although the characteristics of the signal emanating from each zone will be dependent on the environmental conditions, these zones

will remain constant throughout the analysis and will enable the study of the evolution of the signal as the conditions changed.

V. RESULTS

A. PDFs

The aggregate of all of the pixels within each of the zones shown in Fig. 4 produces a joint histogram by counting the frequency of occurrence of a given intensity pair (I, σ_0) in the ensemble of samples collected in each run. The integration of the joint histogram along each coordinate axis yields the individual histogram for each data set. Special care is taken to remove the occurrence of signal pairs where there is no marine radar signal (i.e., $I_r(\theta, r, t) = 0$). These are likely points on the water surface that are shadowed by the preceding wave crests (or simply scattering weakly), and they would bias the distributions toward low backscattered power.

The minimum number of usable sample pairs was around 535 000 (camera 1, surf zone, and Run 18). The joint and individual histograms were constructed using 25 predefined bins, 11 intensity values wide for video, and 3 dB wide for marine radar. In the following, the results are presented for the field of view corresponding to camera 1. The results from the other cameras show a similar behavior unless noted otherwise. In the following, we treat the normalized histograms as a representative of the pdf and JPDF.

1) *Video Data*: The left column in Fig. 5 shows the pdfs of the video data. In general, the histograms have three different shapes. The first type is the expected peak at low intensity values, e.g., the offshore series for Runs 13 and 18 (circles and asterisks in Fig. 5(a)). These data represent the intensity modulations induced by the wave slope variations of the nonbreaking waves. The resulting signal has a relatively narrow dynamic range, which spans a few bins of the histogram. Also, although the shape is preserved, the means are the offset between runs

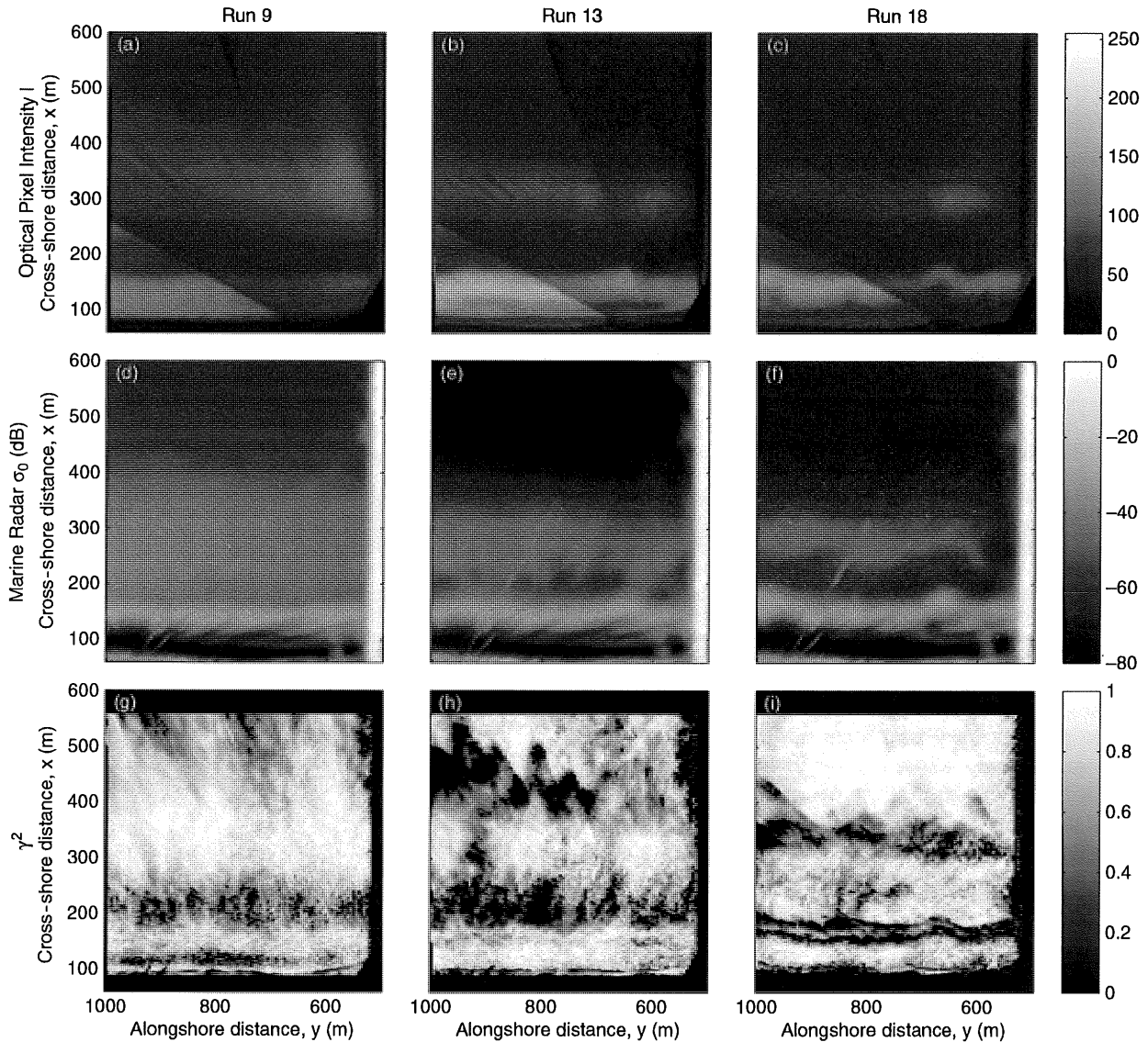


Fig. 3. (Upper row) Thirty-minute time-averaged video images. (Middle row) Thirty-minute time-averaged marine radar images. (Lower row) Median magnitude squared coherence (γ^2) within $\pm 5\%$ of the peak frequency. The columns correspond to different runs.

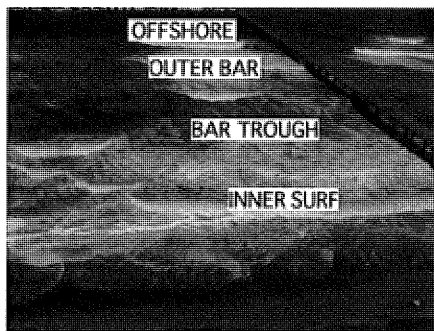


Fig. 4. Definition of the zones within the field of view of camera 1.

mostly owing to the changes in the ambient light, the color of the sea surface, and/or the changes in the camera settings, which were allowed to be adjusted freely between runs depending on the illumination conditions. The wave conditions (wave

TABLE II
DEFINITION OF THE ZONES. THE VALUES REPRESENT THE CROSS-SHORE DISTANCE IN THE FRF REFERENCE SYSTEM

Identifier	Cross-shore limits (m)	
	x_{\min}	x_{\max}
Inner Surf	100	150
Bar Trough	150	250
Outer Bar	250	350
Offshore	400	600

height, period, and, hence, slope) mostly govern the width of the histogram, with a lesser effect on the mean.

The second evident shape is a peak of smaller magnitude at low intensities, followed by an exponentially decaying tail. This kind of behavior would be expected from zones where some wave breaking is taking place with some degree of foam persistency. This can be seen, for instance, in the offshore zone (squares in Fig. 5(a)) where Run 9 differs from the other runs due to intermittent breaking (as shown in Fig. 2).

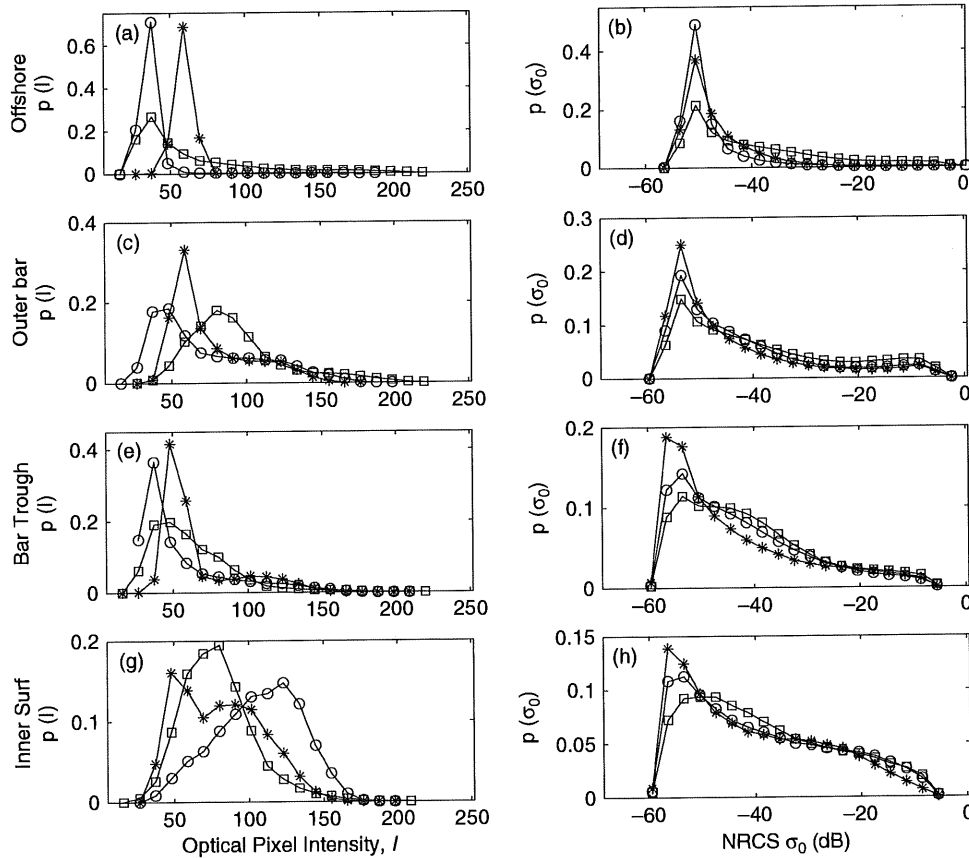


Fig. 5. Histograms of the optical pixel intensity (left) and marine radar NRCS (right) for the data taken within the field of view of camera 1. Top to bottom correspond to measurements taken in the offshore, outer bar, bar trough, and inner surf zone boxes, respectively. (□) Run 9. (o) Run 13. (*) Run 18. Note that the vertical axis is different for each panel.

This behavior can also be seen in the outer bar for Runs 9 and 13 (Fig. 5(c); circles and squares, respectively). Finally, the third shape corresponds to conditions where the breaking becomes more frequent and/or foam persistence becomes more pronounced. In which case, the histogram widens, the peak intensity count occurs at larger I values, and the high intensity side of the histogram shows a gently fall off, as can be seen in the inner surf for Runs 9 and 13 (Fig. 5(g); circles and squares).

2) *Marine Radar*: As shown in the right column of Fig. 5, the majority of the curves for the marine radar show a relatively constant shape, characterized by a sharp peak at a low backscattered power (usually about -55 to -50 dB), followed by an exponential decay, both of which are consistent with the scattering according to the CST model. The magnitude of the peak and the tail contribution show a dependence on the environmental and wave parameters, such as wind-induced roughness or wave breaking. For instance, the effect of wave breaking can be observed in the transition from the high peaks and low tails for Run 18 to the low peaks and high tail values for Run 9 (asterisks and squares in Fig. 5(f)), which represents the relative increase in wave breaking in the trough between those two runs. This is similar to the spatial transition within Run 9 from Fig. 5(d)–(h), as wave breaking steadily increased as the waves propagated onshore.

Of particular interest is the effect of intermittent breaking, for instance, at the outer bar (Fig. 5(d)). In this zone, the histograms

for each run are very similar in shape. Each also shows a clear departure from the monotonic decay near -25 dB, where the histograms instead increase in magnitude, reaching maxima at around -7 dB, above which they show a decaying trend. Similar results were also found for all runs in the outer bar, bar trough, and inner surf for the field of view of cameras 3 and 0 (not shown) and for the offshore zone in camera 1 (squares in Fig. 5(b)). The increased probability values above the exponential decay at an NRCS greater than -20 dB cannot be explained by traditional scattering models. It seems reasonable that these are related to another scattering mechanism. However, a clear identification of the source is not possible with the histogram alone.

B. Joint Histograms

The results, so far, qualitatively demonstrate how the different water surface types (unbroken waves, active breaking, and foam) manifest themselves in the pdfs. In terms of breaking identification, we know that the challenge is to separate active breaking from remnant foam in the optical data and steep nonbreaking waves from active breaking in the radar data. In order to overcome the limitations of independently using either sensor, we will pursue a sensor fusion approach. We hypothesize that the information from both sensors can be combined in the JPDF (or, in this case, the joint histogram)

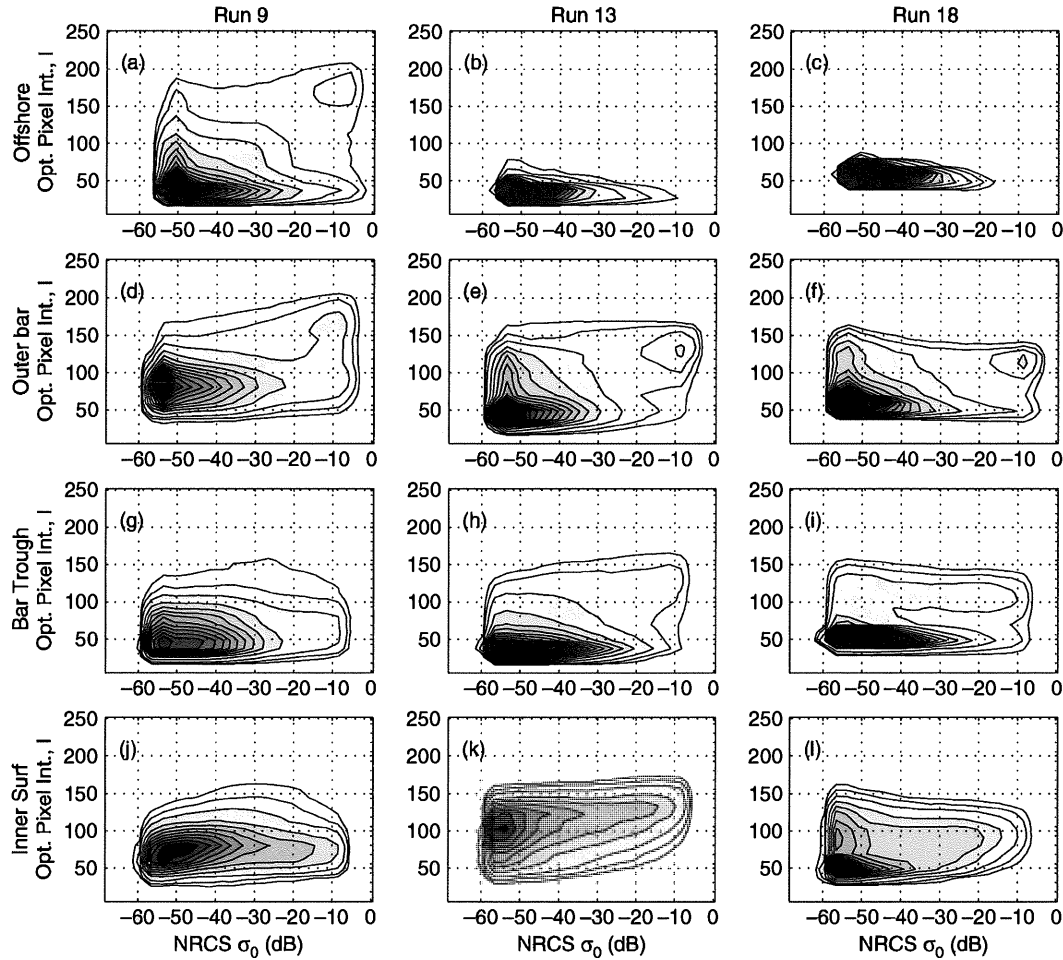


Fig. 6. Joint histograms for the video (camera 1) and marine radar. The columns correspond to Runs 9, 13, and 18, respectively. The rows correspond to zones according to Fig. 4.

in order to better identify the active breaking events and to distinguish them from both the remnant foam and the steep nonbreaking waves.

Fig. 6 shows the JPDFs for all zones in each of the three runs. It can be seen that, typically, the peak of the JPDF occurs at relatively low video intensities and low backscattered powers. We expect the data in this area of the JPDF to arise from the nonbreaking waves, and this is confirmed by the fact that most of the data in panels Fig. 6(b) and (c) (offshore and nonbreaking conditions) are confined to this area. In those panels, the JPDF concentrates along a ridge covering a narrow band of optical intensities (vertical axis, typically between $I = 20$ – 70) and a wide range of NRCS levels (horizontal axis). This is due to the slope modulations from the unbroken waves inducing a large dynamic range in the NRCS signal, in accordance with the CST [55], but a relatively narrow dynamic range in the optical signal, which is due only to specular slope modulations [26]. This narrow ridge is also prominent in the data from the bar trough for the decaying wave conditions (Fig. 6(h) and (i)). In addition, it can be seen that the strongest radar returns correspond to the weakest optical intensities (e.g., Fig. 6(c)) from the (optically dark) steep front faces of the waves.

There is also a secondary ridge that is fairly prominent in many cases (e.g., Fig. 6(a), (e), and (f)). This is a vertical ridge spanning a wide range of optical intensity bins (I up to 150) but a relatively narrow range in NRCS (typically -55 to -50 dB). This ridge is indicative of the remnant foam which does not scatter strongly at X-band, but it is optically bright [17].

There is also an evidence in the JPDFs of a secondary peak of lesser magnitude at relatively large optical intensities and large backscattered powers. This local peak is most evident in Fig. 6(a), (d), and (e) for $I > 100$ – 125 and $\text{NRCS} > -20$ dB. It is totally absent in the nonbreaking conditions (Fig. 6(b) and (c)). Based on our existing understanding, this peak should be the signature of the active wave breaking appearing bright in both sensors. While the peak seems to be consistently backscattering more than -20 dB, the intensity magnitudes appear to decrease some from Fig. 6(a)–(f) (discussed further in the following). Nevertheless, the JPDF method effectively separates out this portion of the data. For example, the secondary peak in Fig. 6(a) is well separated from the main peak of the nonbreaking waves in the lower left quadrant.

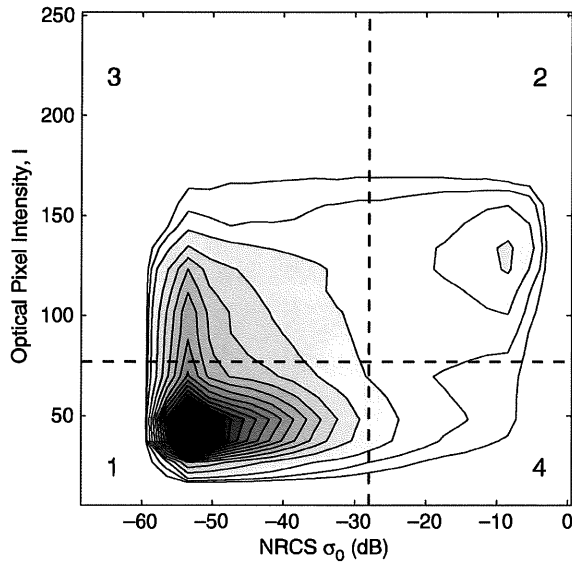


Fig. 7. Characterization of the JPDF in four main regions. The dashed lines denote the discrimination thresholds defined in (3).

C. Identification of Breaking Events

The JPDF suggests that, by using simultaneous data from both sensors, the discrimination between different stages of the breaking process is feasible. In particular, it is possible to identify four distinct regions in the JPDF that are associated with different stages of wave breaking in the surf zone. These are shown in Fig. 7. Region 1 corresponds to low optical intensities and low backscattered power (thus the nonbreaking waves). Region 2 corresponds to large optical pixel intensities and large backscattered power due to active breaking waves. Region 3 corresponds to large optical intensities at relatively low backscattered power due to remnant foam. The fourth region corresponds to low optical intensities and large returned power, corresponding to steep waves.

The discrimination procedure is conceptually simple in the sense that, given a suitable selection of the threshold lines shown in Fig. 7, it is straightforward to differentiate between regions. Consequently, the following rules are defined.

Nonbreaking (region 1):

$$I(x, y, t) < I^t \quad \sigma_0(x, y, t) < \sigma_0^t. \quad (3a)$$

Breaking (region 2):

$$I(x, y, t) \geq I^t \quad \sigma_0(x, y, t) \geq \sigma_0^t. \quad (3b)$$

Foam (region 3):

$$I(x, y, t) \geq I^t \quad \sigma_0(x, y, t) < \sigma_0^t. \quad (3c)$$

Steep waves (region 4):

$$I(x, y, t) < I^t \quad \sigma_0(x, y, t) \geq \sigma_0^t. \quad (3d)$$

where I^t denotes the optical intensity threshold and σ_0^t is the power threshold (in decibels) for the marine radar record.

However, the threshold values still need to be determined, and there may be some variability due to the environmental conditions. A clear example of this is the aforementioned peak in region 2 shown in Fig. 6(d)–(f), which exhibits a steady decrease in optical intensity values. The decrease is most likely a direct result of the change in sun position for the different runs, as the collection times were 6 P.M., 2 P.M., and 11 A.M. local time, respectively. Hence, the sun was moving from a position behind the cameras to a position in front (the cloud cover data were not recorded). Consequently, we first approach the problem in an *ad hoc* manner using visual inspection to iteratively select the threshold values that appear to provide the best detection rate on a run-by-run basis.

There is really no absolute measure of how well the separation method works. Instead, we must rely on a visual qualitative comparison by overlaying the extracted water surface types onto the video image time series. We recognize that an automated detection algorithm that still relies on qualitative measures of ground truth may seem to be of limited value. Therefore, to clarify our purposes here, clearly, using the “eye of the beholder” as a breaking detection method is highly impractical for large data sets. In addition, the very high resolution data needed for the human (visual) detection of the breaking place heavy demands on data storage and bandwidth capabilities. Hence, here, we have pursued a detection method that is based on thresholds that are initially verified by visual means but, ideally, with limited dependence on the environmental conditions. After these tests, further verification will come from the comparison of the derived breaking wave data with the expected results based on the surf zone dynamics, similar to what was done by *Haller and Catalán* [8].

Figs. 8 and 9 show the examples of the performance of the joint method of detection for Runs 9 and 18, respectively (the results for Run 13 were similar), where random snapshots (taken from the 30-min-long series) of each sensor are overlaid with spatial contours based on the rules for water surface type. The contours that outline the breaking appear to well correspond with what we consider to be the active breaking region, which travels on the wave fronts. This can be seen, for instance, on the large breaking event spanning $y = 520$ – 630 m and at $x = 350$ m in Fig. 8(d). The foam patches also appear to be clearly identified, e.g., the large foamy area centered at $x = 300$ m in Fig. 9(d). In the same panel, the detection of the very steep faces is highlighted with the event at $y = 640$ – 720 m and $x = 370$ m. Moreover, the joint method improves detection especially under conditions when the roller fronts are not so easily discernible from the remnant foam by looking at the video image alone, e.g., the event at $y = 670$ m and $x = 280$ m in Fig. 9(d). Although in these figures only a snapshot is shown, the visual validation of these and other events (such as the breaking wave identified at $y = 720$ m and $x = 500$ m in Fig. 8(d)) used the full optical time history of the waves as they shoal and break.

Table III shows the final selected thresholds and some related statistics determined using camera 1. Encouragingly, the table shows that the best performing I^t and σ_0^t values are essentially constant between the three runs. Clearly, the optical threshold must be affected by the illumination conditions (e.g., no

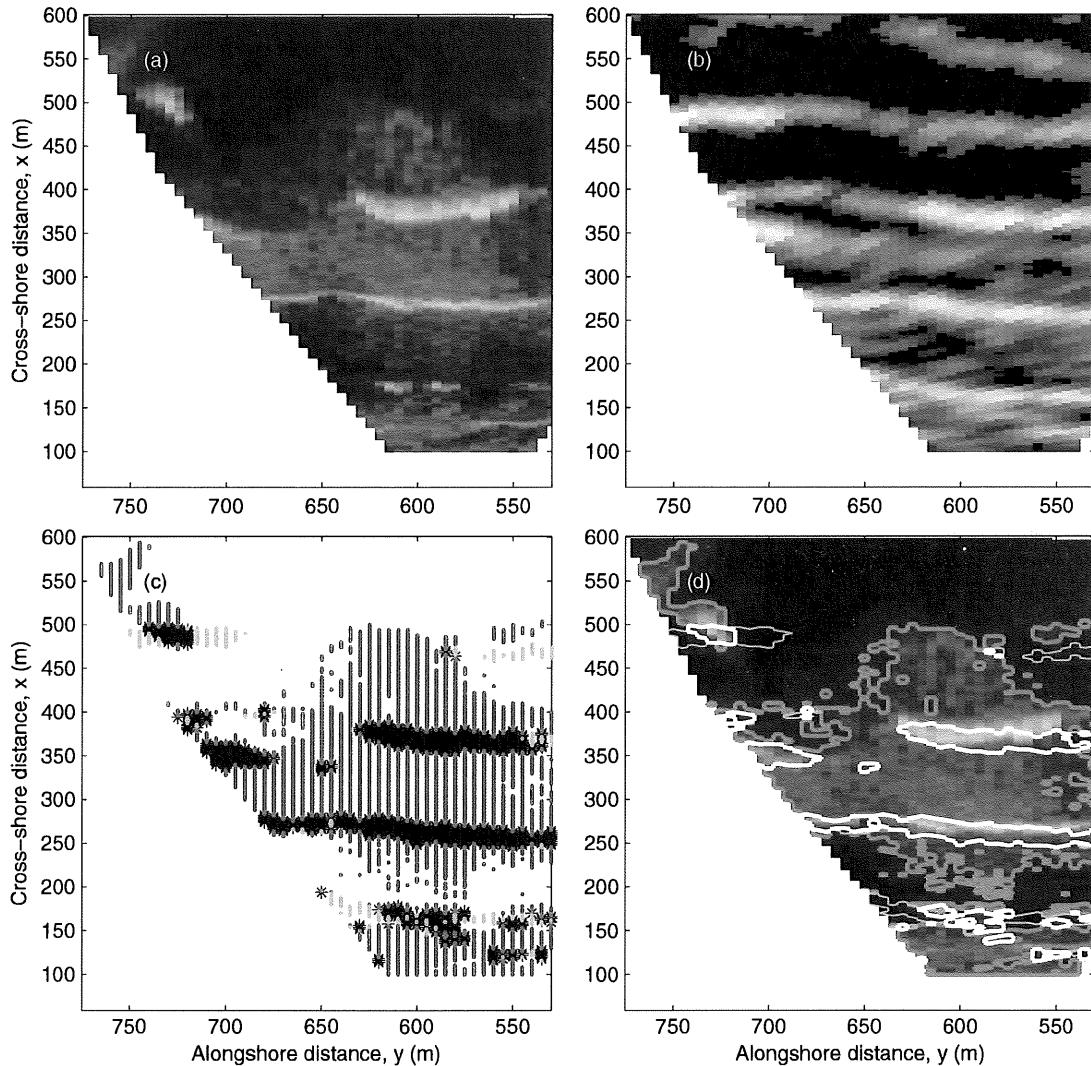


Fig. 8. Combined breaking detection example using camera 1 (Run 9). (a) Video snapshot. (b) Marine radar snapshot. (c) Discrimination results. The black markers denote breaking, the gray markers denote the remnant foam, and the light gray markers denote the steep waves. (d) Discrimination results overlaid as contours over the video snapshot. The white lines denote the breaking events, the dark gray lines denote the remnant foam, and the thin light gray lines denote the steep waves.

threshold exists for the nighttime data), and it shows some variability. However, the cameras have their own automated gain and shutter adjustments, which generally account for preventing saturation and limiting the variability in the detection threshold. Finally, it has to be noted that the selected optical thresholds were found to be $I^t = 2/3 * \bar{I}(x, y)_{\max}$, where $\bar{I}(x, y)_{\max}$ is the spatial maximum over the whole field of view of the time exposure image, suggesting a rule for application to other data.

On the other hand, there was no variation needed in the NRCS threshold for breaking detection partly because the gain setting on the marine radar remains fixed. This suggests a nondependence on the environmental conditions and, possibly, a standard value. However, testing against a larger data set is required. Nevertheless, the suggested threshold value falls within the range of the backscattered powers associated with the departure of the microwave pdf from the exponentially decaying tail.

Next, in order to demonstrate the improvement in detection that the JPFD method provides in comparison to the single sensor methods, the sensitivity of the detection skill to the thresholds I^t and σ_0^t is independently tested for each sensor. For the optical record, the thresholds are chosen at selected ratios that are relative to the maximum of the time exposure due to the apparent rule found from the trial-and-error procedure. For the marine radar data, a range of NRCS thresholds on the decibel scale and centered on the baseline found in the joint detection tests is chosen.

Fig. 10 shows the results for the optical records, where each colored area demarcates the region being identified as breaking waves when using a given threshold. Increasing the threshold values yields a better agreement with the visual signature of breaking (see Fig. 8(a) for reference). For Run 9 (Fig. 10(a)), the best agreement is obtained for $I^t = 1.5\bar{I}(x, y)_{\max}$, while the lower thresholds tend to include the remnant foam. However, the skill changes for Run 18 (Fig. 10(b) to be compared

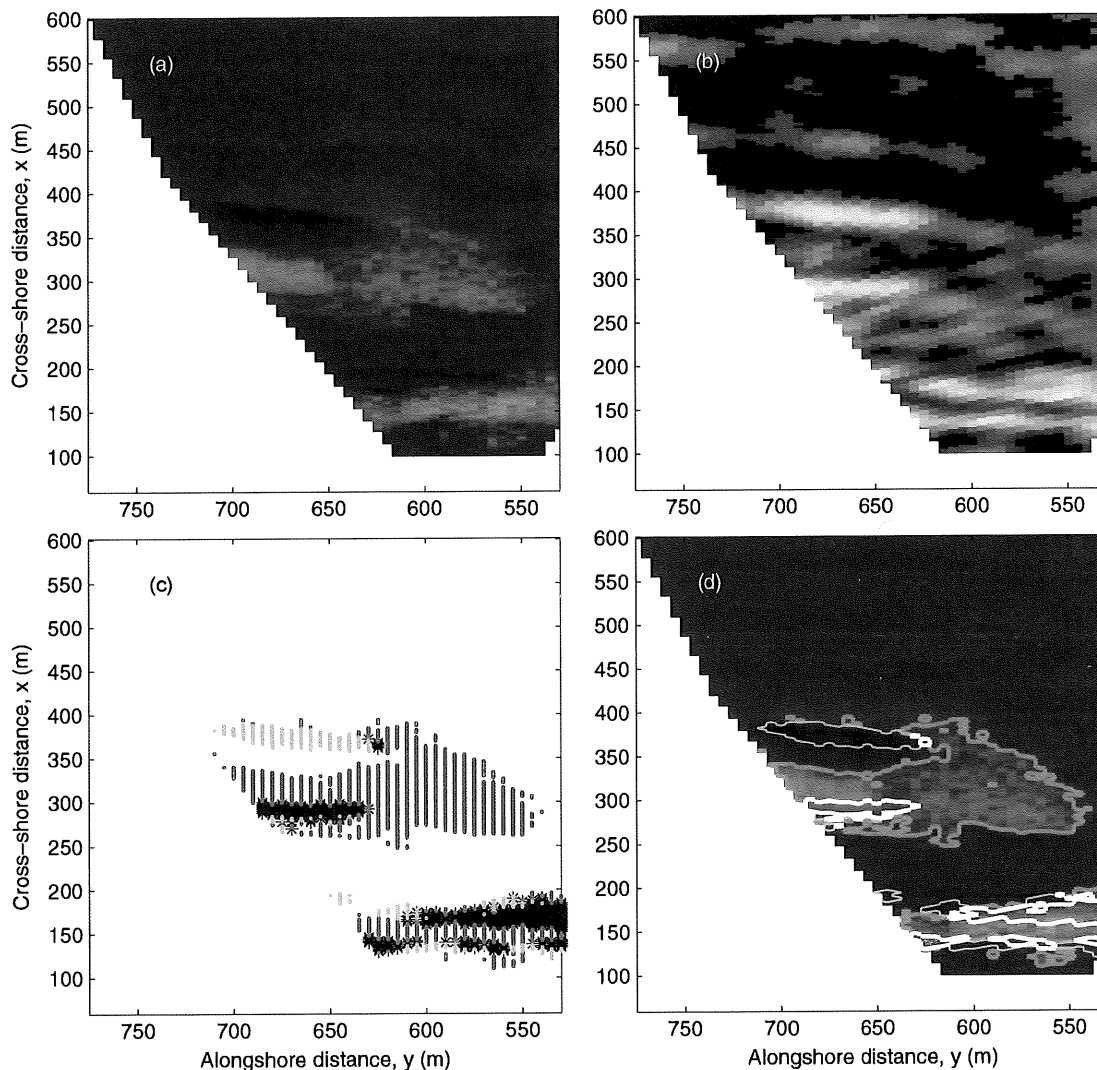


Fig. 9. Combined breaking detection (Run 18). Same key as Fig. 8.

TABLE III

SUMMARY OF THE THRESHOLD VALUES FOR THE COMBINED BREAKING DETECTION METHOD. THE ABSOLUTE MAXIMA “MAX(0)” AND THE MAXIMA OF THE TIME EXPOSURE “MAX(–)” ARE PROVIDED FOR REFERENCE. THE VIDEO VALUES ARE GIVEN IN GRAYSCALE INTENSITY, AND THE RADAR VALUES ARE IN DECIBELS

Run #	Video I^t	Video Max(I)	Video Max(\bar{I})	Video $I^t/\text{Max}(\bar{I})$	Radar σ_0^t	Radar Max(σ_0)	Radar Max($\bar{\sigma}_0$)
9	70	219	105	66%	-28	0	-17
13	77	205	128	60%	-28	-1	-18
18	75	207	119	63%	-28	-3	-18

with Fig. 9(a)), where the foam patches tend to be included even at the largest threshold used. These highest thresholds are also nonconservative in that they do not capture the small breaking events and tend to minimize the size of the breaking wave rollers.

For the radar images (Fig. 11), even the use of the largest thresholds tends to overpredict the spatial extent of the roller by including the steepened waves (see $y = 640\text{--}720$ m and $x = 370$ m; Fig. 11(b) compared with Fig. 9(a)). The steep waves that are mistakenly identified as breaking are easier to point out visually than the complementary effect of the

foam that is mistakenly identified as breaking. In summary, in Figs. 8–11, it is clear that either sensor acting independently cannot provide a reliable detection with the predefined thresholds in an automated way. On the other hand, the thresholds used successfully in the joint method correspond to the minimum (optical) and mid values (marine radar) tested in Figs. 10 and 11. These thresholds are inherently conservative, and they include the foam and steep waves in the detection when independently used. However, when both sensors are used together, these conservative thresholds appear to work well.

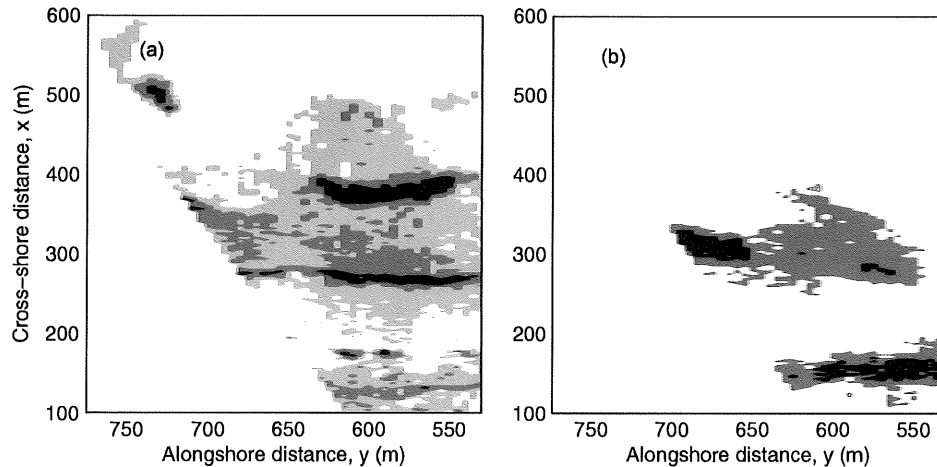


Fig. 10. Sensitivity tests for independent breaking detection using the optical records. (a) Run 9. (b) Run 18. The colored areas denote the events that are identified as breaking using different optical pixel intensity thresholds. The light gray, dark gray, and black areas correspond to the thresholds set at $I^t = 0.66 \max(I)$, $1.0 \max(I)$, and $1.5 \max(I)$, respectively.

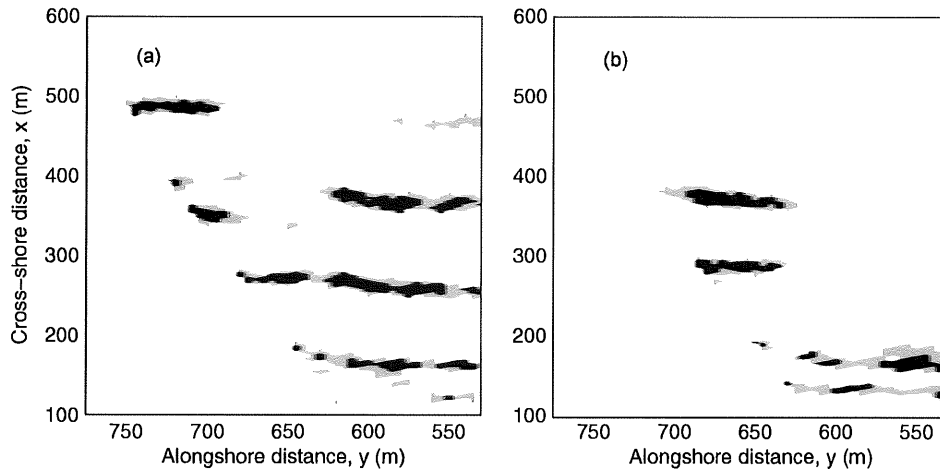


Fig. 11. Sensitivity tests for independent breaking detection using the microwave records. (a) Run 9. (b) Run 18. The colored areas denote the events that are identified as breaking using different NRCS thresholds. The light gray, dark gray, and black areas correspond to the thresholds set at $\sigma_0^t = -40$, -28 , and -15 dB, respectively.

VI. DISCUSSION

A. Sample Applications

The results in the previous section validate the qualitative interpretation of the JPFD and the hypothesis that the joint method can be used for breaking detection. Next, we use the joint method to demonstrate that it can be used to quantify the wave breaking parameters that are important in nearshore processes. For instance, the parametric wave evolution models [2], [3] often rely on a statistical description of the percentage of waves breaking at a given spatial location. Models for this quantity, also known as the fraction of breaking waves Q_b , have been generally determined and calibrated by visually counting the breaking waves at discrete locations and along a single cross-shore transect [3], [4]. Consequently, the spatial resolution and coverage are often poor. In Fig. 12, the spatial (2-D) distribution of Q_b is shown for the three runs, where, for instance, it can be seen that the camera dependences are nicely reduced, as compared to Fig. 3 (upper panels).

Other important parameters are the geometrical properties of the roller. The early work of *Duncan* [7] showed that, under equilibrium conditions, the dissipation of the energy can be related to the geometry of the wave roller, i.e., the roller cross-sectional area, cross-wave length, and local wave slope. However, a direct measurement of those parameters in the field is a difficult task. Recently, the cross-shore evolution of the roller lengths was linked to roller dissipation using laboratory data [8]. The present approach offers the possibility to extend the technique to field data. For instance, assuming that the waves are propagating normal to the shore, the roller length can be measured as the cross-shore extent of the region identified as a breaking wave at any given alongshore position. As an example, in Fig. 13, the roller lengths obtained from the present data set along a cross-shore transect are shown. These data show a similar (but field scale) cross-shore variation as the laboratory results of *Haller and Catalán* [8], and if extended in the alongshore direction to obtain the roller areal coverage, they could be used to determine the spatial distribution of the roller dissipation.

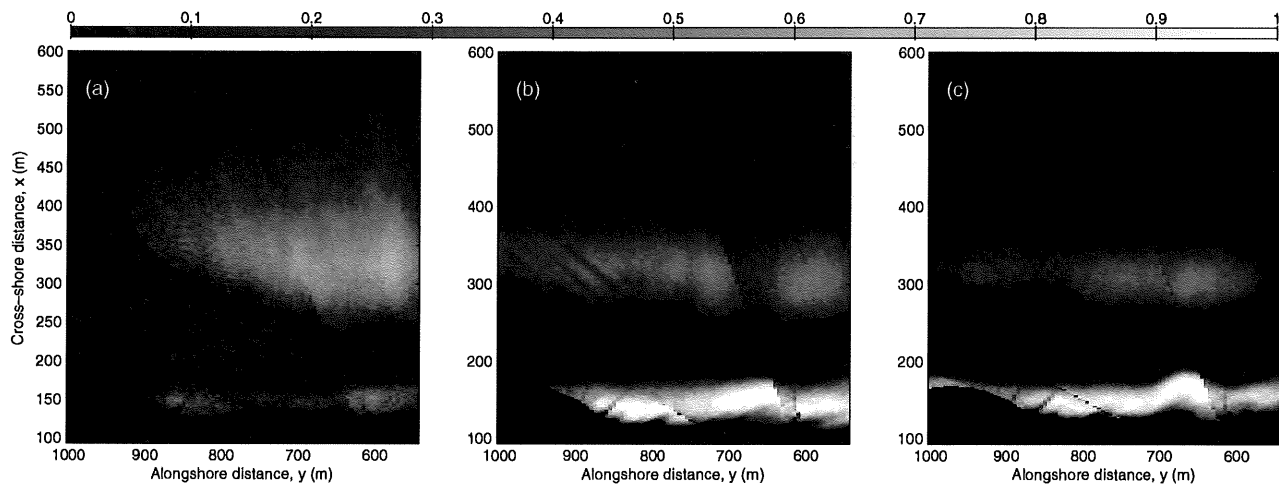


Fig. 12. Computed fraction of the breaking waves for Runs (a) 9, (b) 13, and (c) 18.

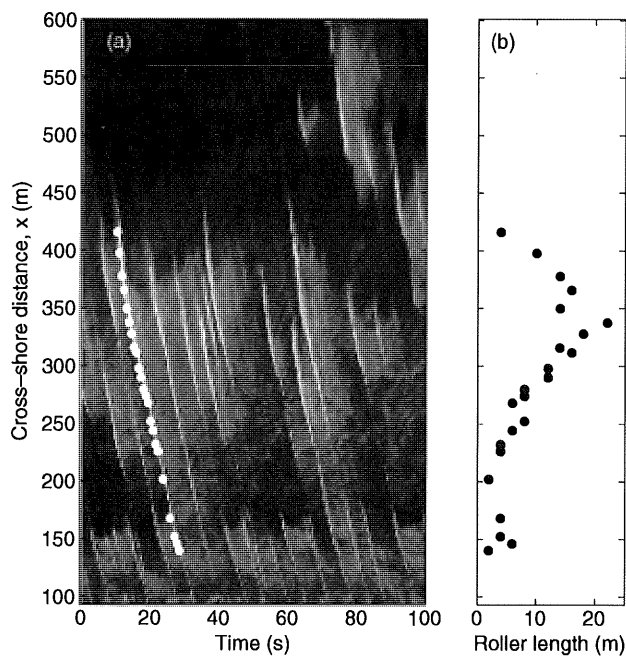


Fig. 13. (a) Time–space map of the optical pixel intensity obtained from a cross-shore transect of Run 9. The white circles correspond to the points along a sample wave trajectory on which the breaking events have been isolated. (b) Measured roller lengths.

B. Sources of Error

A key to the success of the method is to have the two sensors accurately synchronized and geolocated in order to allow point-to-point comparisons. Potential errors arise from the misregistration of either of the signals. The video is more susceptible to this as the line-of-view registration (as opposed to the time-of-flight for the microwave sensor) is affected by finite amplitude waves on which signals from higher vertical elevations than the predefined reference (usually the mean water level) are rectified to the horizontal points further away from the camera. This becomes more pronounced at large range distances (lower grazing angles) and for larger waves. This effect might be strong near the onset of breaking since it is the location of the largest wave amplitude, and the optical signature would be most

shifted backwards, relative to the location of the wave crest. Radar misregistration error could arise from changes in (or incorrect determination of) the azimuthal datum for the antenna rotor. Both systems are also subject to synchronization errors in the recorded GPS time stamps. Fortunately, accuracies of < 0.5 s are sufficient as the video sampling rate used was 2 Hz (for the radar, it is 0.73 Hz).

The size and orientation of the intrinsic radar resolution cells can be another factor. For instance, we note that the JPFDs do appear less well organized in the inner surf zone (Fig. 6 bottom row). Although the main peak appears due to the nonbreaking phase of the waves, the rest of the data tends to smear out toward the right or the upper right quadrant rather than exhibiting a clear secondary peak. For these cases and location (camera 1 and inner surf), the radar is looking obliquely at the waves. Therefore, the individual radar cells may be encompassing both active breaking and nonbreaking scatterers, thus averaging the returned power toward higher values than when only the non-breaking waves were present [56]. A more uniform population of the scatterers can be expected when the incoming wave direction is aligned with the radar look direction. This is the case for camera 3, whose pdfs exhibit a very distinct secondary peak (breaking waves) even in the inner surf zone (not shown).

VII. CONCLUSION

The specific goal of the present work is to develop a methodology for identifying the active breaking events in the surf zone, which minimizes the false alarms that are due to the remnant foam or steep waves. It was found that a joint method using two synchronized remote sensors proved successful in identifying the breaking events on a wave-by-wave basis. The optimal method uses conservative (i.e., high false alarm rate if used independently) joint threshold values that do not vary significantly with the environmental conditions that were tested.

The methodology was developed through an analysis of the individual pdfs determined from the surf zone observations using optical and X-band sensors and through comparisons with the expected distribution functions for each sensor, as found in previous works. The pdfs from the optical sensor were consistent with the existence of two distinct scattering mechanisms. In

addition, the pdfs from the X-band sensor showed the presence of an inflection point at a large NRCS, which is suggestive of a departure from the Bragg or CST scattering mechanism. This inflection point was located in the range -30 to -20 dB, and a fixed value of -28 dB was used in the detection algorithm. This value proved to be independent of the changes in the ambient environmental conditions during the experiment. Being consistent with the findings of previous research [16], [25], [57], it was found that the strongest backscatter comes from the steep and/or breaking waves. However, unlike most results from a deeper water, it is apparent from the present results that, in the surf zone, the depth-limited breaking waves are the more dominant mechanism.

Finally, the joint method allows several water surface types to be identified, i.e., the active breaking, the remnant foam, and the crests of the steep waves. The method can now be used to quantify important parameters for wave-driven hydrodynamics such as the space-time variability of wave breaking, the fraction of the breaking waves, the wave roller scales, and the wave roller dissipation. In addition, the method can allow a more detailed analysis of the microwave scattering mechanisms and their dependence on the water surface conditions.

ACKNOWLEDGMENT

The authors would like to thank D. Trizna from the Imaging Science Research, Inc.; the staff of the USACE Field Research Facility; J. Stanley from the Coastal Imaging Laboratory, OSU; and G. Chatham from APL-UW for their support during the field experiment.

REFERENCES

- [1] I. A. Svendsen, *Introduction to Nearshore Hydrodynamics*. River Edge, NJ: World Sci., 2006, ser. Advanced Series on Ocean Engineering.
- [2] J. A. Battjes and J. P. F. M. Janssen, "Energy loss and set-up due to breaking random waves," in *Proc. 16th Int. Conf. Coastal Eng.*, 1978, pp. 569–587.
- [3] E. B. Thornton and R. T. Guza, "Transformation of wave height distribution," *J. Geophys. Res.*, vol. 88, no. C10, pp. 5925–5938, 1983.
- [4] T. E. Baldock, P. Holmes, S. Bunker, and P. V. Weert, "Cross-shore hydrodynamics within an unsaturated surf zone," *Coastal Eng.*, vol. 34, no. 3/4, pp. 173–196, Sep. 1998.
- [5] N. Booij, R. C. Ris, and L. H. Holthuijsen, "A third-generation wave model for coastal regions 1. Model description and validation," *J. Geophys. Res.*, vol. 104, no. C4, pp. 7649–7666, Apr. 1999.
- [6] R. Silva, M. Losada, and P. Salles, "Modelling linear wave transformation induced by dissipative structures—Random waves," *Ocean Eng.*, vol. 33, no. 16, pp. 2174–2194, Nov. 2006.
- [7] J. Duncan, "An experimental investigation of breaking waves produced by a towed hydrofoil," *Proc. R. Soc. Lond. A, Math. Phys. Sci.*, vol. 377, no. 1770, pp. 331–348, Jul. 1981.
- [8] M. C. Haller and P. A. Catalán, "Remote sensing of wave roller lengths in the laboratory," *J. Geophys. Res.*, vol. 114, no. C7, p. C07022, Jul. 2009.
- [9] M. S. Longuet-Higgins and N. D. Smith, "Measurement of breaking waves by a surface jump meter," *J. Geophys. Res.*, vol. 88, no. C14, pp. 9823–9831, Nov. 1983.
- [10] W. K. Melville, M. R. Loewen, F. C. Felizardo, A. T. Jessup, and M. J. Buckingham, "Acoustic and microwave signatures of breaking waves," *Nature*, vol. 336, no. 6194, pp. 54–56, Nov. 1988.
- [11] M. R. Loewen and W. K. Melville, "Microwave backscatter and acoustic radiation of breaking waves," *J. Fluid Mech.*, vol. 224, pp. 601–623, 1991.
- [12] R. Holman and J. Stanley, "The history and technical capabilities of ARGUS," *Coastal Eng.*, vol. 54, no. 6/7, pp. 477–491, Jun./Jul. 2007.
- [13] A. H. Callaghan and M. White, "Automated processing of sea surface images for the determination of whitecap coverage," *J. Atmos. Ocean. Technol.*, vol. 26, no. 2, pp. 383–394, Feb. 2009.
- [14] A. T. Jessup, C. J. Zappa, M. R. Loewen, and V. Hesany, "Infrared remote sensing of breaking waves," *Nature*, vol. 385, no. 6611, pp. 52–55, Jan. 1997.
- [15] G. O. Marmorino and G. B. Smith, "Bright and dark ocean whitecaps observed in the infrared," *Geophys. Res. Lett.*, vol. 32, no. 11, p. L11 604, Jun. 2005.
- [16] A. T. Jessup, W. K. Melville, and W. C. Keller, "Breaking waves affecting microwave backscatter. 1. Detection and verification," *J. Geophys. Res.*, vol. 96, no. C11, pp. 20 547–20 559, Nov. 1991.
- [17] M. C. Haller and D. R. Lyzenga, "Comparison of radar and video observations of shallow water breaking waves," *IEEE Trans. Geosci. Remote Sens.*, vol. 41, no. 4, pp. 832–844, Apr. 2003.
- [18] T. C. Lippmann and R. A. Holman, "Quantification of sandbar morphology: A video technique based on wave dissipation," *J. Geophys. Res.*, vol. 94, no. C1, pp. 995–1011, Jan. 1989.
- [19] B. G. Ruessink, P. S. Bell, I. M. J. van Enckevort, and S. G. J. Aarninkhof, "Nearshore bar crest location quantified from time-averaged X-band radar images," *Coastal Eng.*, vol. 45, no. 1, pp. 19–32, Mar. 2002.
- [20] J. E. McNinch, "Bar and Swash Imaging Radar BASIR: A mobile X-band radar designed for mapping nearshore sand bars and swash-defined shorelines over large distances," *J. Coastal Res.*, vol. 23, no. 1, pp. 59–74, Jan. 2007.
- [21] K. Ward, C. Baker, and S. Watts, "Maritime surveillance radar. I. Radar scattering from the ocean surface," *Proc. Inst. Elect. Eng. F—Radar Signal Process.*, vol. 137, no. 2, pp. 51–62, Apr. 1990.
- [22] D. B. Trizna, "Statistics of low grazing angle radar sea scatter for moderate and fully developed ocean waves," *IEEE Trans. Antennas Propag.*, vol. 39, no. 12, pp. 1681–1690, Dec. 1991.
- [23] A. S. Mironov and V. A. Dulov, "Detection of wave breaking using sea surface video records," *Meas. Sci. Technol.*, vol. 19, no. 1, p. 015 405, Jan. 2008.
- [24] B. L. Lewis and I. D. Olin, "Experimental study and theoretical model of high-resolution radar backscatter from sea surfaces," *Radio Sci.*, vol. 15, no. 4, pp. 815–828, Jul./Aug. 1980.
- [25] Y. Liu, S. Frasier, and R. McIntosh, "Measurement and classification of low grazing angle radar sea spikes," *IEEE Trans. Antennas Propag.*, vol. 46, no. 1, pp. 27–40, Jan. 1998.
- [26] B. Jähne, J. Klinke, and S. Waas (1994, Aug.). Imaging of short ocean wind waves: A critical theoretical review. *J. Opt. Soc. Amer. A, Opt. Image Sci.* [Online]. 11(8), pp. 2197–2209. Available: <http://www.opticsinfobase.org/abstract.cfm?URI=josaa-11-8-2197>
- [27] D. Stilwell, "Directional energy spectra of the sea from photographs," *J. Geophys. Res.*, vol. 74, no. 8, pp. 1974–1986, Apr. 1969.
- [28] R. E. Walker, *Marine Light Field Statistics*. New York: Wiley, 1994.
- [29] R. Frouin, M. Schwindling, and P.-Y. Deschamps, "Spectral reflectance of sea foam in the visible and near-infrared: In situ measurements and remote sensing implications," *J. Geophys. Res.*, vol. 101, no. C6, pp. 14 361–14 371, 1996.
- [30] D. B. Ross and V. Cardone, "Observations of oceanic whitecaps and their relation to remote measurements of surface wind speed," *J. Geophys. Res.*, vol. 79, no. 3, pp. 444–452, 1974.
- [31] E. C. Monahan and D. K. Woolf, "Comments on 'variations of whitecap coverage with wind stress and water temperature'," *J. Phys. Oceanogr.*, vol. 19, no. 5, pp. 706–709, May 1989.
- [32] B. R. Kerman and L. Dernier, "Multifractal representation of breaking waves on the ocean surface," *J. Geophys. Res.*, vol. 99, no. C8, pp. 16 179–16 196, 1994.
- [33] C. Lafon, J. Piazzola, P. Forget, O. Le Calve, and S. Despiau, "Analysis of the variations of the whitecap fraction as measured in a coastal zone," *Boundary-Layer Meteorol.*, vol. 111, no. 2, pp. 339–360, May 2004.
- [34] Y. Sugihara, H. Tsumori, T. Ohga, H. Yoshioka, and S. Serizawa, "Variation of whitecap coverage with wave-field conditions," *J. Mar. Syst.*, vol. 66, no. 1–4, pp. 47–60, Jun. 2007.
- [35] S. Aarninkhof and B. G. Ruessink, "Video observations and model predictions of depth-induced dissipation," *IEEE Trans. Geosci. Remote Sens.*, vol. 42, no. 11, pp. 2612–2622, Nov. 2004.
- [36] C. Cox and W. Munk, "Statistics of the sea surface derived from sun glitter," *J. Mar. Res.*, vol. 13, no. 2, pp. 198–227, 1954.
- [37] P. Koepke, "Effective reflectance of oceanic whitecaps," *Appl. Opt.*, vol. 23, no. 11, pp. 1816–1824, Jun. 1984.
- [38] J. W. Wright, "A new model for sea clutter," *IEEE Trans. Antennas Propag.*, vol. AP-16, no. 2, pp. 217–223, Mar. 1968.
- [39] F. G. Bass, I. M. Fuks, A. I. Kalmykov, I. E. Ostrovsky, and A. D. Rosenberg, "Very high frequency radio scattering by a disturbed sea surface: 2. Scattering from an actual sea surface," *IEEE Trans. Antennas Propag.*, vol. AP-16, no. 5, pp. 560–568, Sep. 1968.

- [40] S. J. Frasier, Y. Liu, and R. E. McIntosh, "Space-time properties of radar sea spikes and their relation to wind and wave conditions," *J. Geophys. Res.*, vol. 103, no. C9, pp. 18 745–18 757, Aug. 1998.
- [41] A. T. Jessup, W. C. Keller, and W. K. Melville, "Measurements of sea spikes in microwave backscatter at moderate incidence," *J. Geophys. Res.*, vol. 95, no. C6, pp. 9679–9688, Jun. 1990.
- [42] P. A. Hwang, M. A. Sletten, and J. V. Toporkov, "Analysis of radar sea return for breaking wave investigation," *J. Geophys. Res.*, vol. 113, p. C02 003, Feb. 2008.
- [43] P. H. Lee, J. D. Barter, K. L. Beach, C. L. Hindman, B. M. Lake, H. Rungaldier, J. C. Shelton, A. B. Williams, and H. C. Yuen, "X band microwave backscattering from ocean waves," *J. Geophys. Res.*, vol. 100, no. C2, pp. 2591–2611, Feb. 1995.
- [44] W. J. Plant, "A model for microwave Doppler sea return at high incidence angles: Bragg scattering from bound, tilted waves," *J. Geophys. Res.*, vol. 102, no. C9, pp. 21 131–21 146, 1997.
- [45] P. A. Hwang, M. A. Sletten, and J. V. Toporkov, "Breaking wave contribution to low grazing angle radar backscatter from the ocean surface," *J. Geophys. Res.*, vol. 113, p. C09 017, 2008.
- [46] B. L. Gotwols and D. R. Thompson, "Ocean microwave backscatter distributions," *J. Geophys. Res.*, vol. 99, no. C5, pp. 9741–9750, May 1994.
- [47] B. Gotwols and W. Keller, "Radar backscatter statistics from water waves," in *Proc. OCEANS Conf. 'Engineering in the Ocean Environment'*, 1990, pp. 240–242.
- [48] D. R. Thompson and B. L. Gotwols, "Comparisons of model predictions for radar backscatter amplitude probability density functions with measurements from SAXON," *J. Geophys. Res.*, vol. 99, no. C5, pp. 9725–9739, May 1994.
- [49] D. B. Trizna and D. J. Carlson, "Studies of dual polarized low grazing angle radar sea scatter in nearshore regions," *IEEE Trans. Geosci. Remote Sens.*, vol. 34, no. 3, pp. 747–757, May 1996.
- [50] J. V. Toporkov and M. A. Sletten, "Statistical properties of low-grazing range-resolved sea surface backscatter generated through two-dimensional direct numerical simulations," *IEEE Trans. Geosci. Remote Sens.*, vol. 45, no. 5, pp. 1181–1197, May 2007.
- [51] D. Trizna, J. P. Hansen, P. Hwang, and J. Wu, "Laboratory studies of sea spikes at low grazing angles," *J. Geophys. Res.*, vol. 96, no. C7, pp. 12 529–12 537, Jul. 1991.
- [52] W. Plant, W. Keller, and K. Hayes, "Measurement of river surface currents with coherent microwave systems," *IEEE Trans. Geosci. Remote Sens.*, vol. 43, no. 6, pp. 1242–1257, Jun. 2005.
- [53] C. Gommenginger, N. Ward, G. Fisher, I. Robinson, and S. Boxall, "Quantitative microwave backscatter measurements from the ocean surface using digital marine radar images," *J. Atmos. Ocean. Technol.*, vol. 17, no. 5, pp. 665–678, May 2000.
- [54] J. S. Bendat and A. G. Piersol, *Random Data Analysis and Measurement Procedures*, 2nd revised ed. New York: Wiley, 1986.
- [55] W. J. Plant, "Bragg sea scattering of electromagnetic waves from the air/sea interface," in *Surface Waves and Fluxes*, G. L. Gernaert and W. J. Plant, Eds. Norwell, MA: Kluwer, 1990, ch. 11, pp. 41–108.
- [56] H. W. Melief, H. Greidanus, P. van Genderen, and P. Hoozeboom, "Analysis of sea spikes in radar sea clutter data," *IEEE Trans. Geosci. Remote Sens.*, vol. 44, no. 4, pp. 985–993, Apr. 2006.
- [57] J. A. Puleo, G. Farquharson, S. J. Frasier, and K. T. Holland, "Comparison of optical and radar measurements of surf and swash zone velocity fields," *J. Geophys. Res.*, vol. 108, no. C3, p. 3100, 2003.



Patricio A. Catalán received the B.S. degree from the Universidad Santa María, Valparaíso, Chile, in 1997 and the M.Sc. and Ph.D. degrees in civil engineering from Oregon State University, Corvallis, in 2005 and 2008, respectively.

He is currently an Assistant Professor with the Departamento de Obras Civiles, Universidad Santa María. His research interests include multisensor remote sensing of the nearshore ocean, wave breaking, and nearshore modeling.



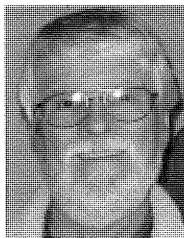
Merrick C. Haller received the B.S. degree from Purdue University, West Lafayette, IN, in 1993 and the M.C.E. and Ph.D. degrees in civil engineering from the University of Delaware, Newark, in 1996 and 1999, respectively.

He presently holds joint appointments as an Associate Professor with the School of Civil and Construction Engineering as well as the College of Oceanic and Atmospheric Sciences, Oregon State University, Corvallis. Previously, he worked as a Research Engineer with Veridian Systems Division and the University of Michigan, Ann Arbor. His present research interest is in nearshore wave transformation and breaking and all that becomes of that.



Robert A. Holman received the B.S. degree in mathematics and physics from the Royal Military College of Canada, Kingston, ON, Canada, in 1972 and the Ph.D. degree in physical oceanography from Dalhousie University, Halifax, NS, Canada, in 1979.

He then joined the College of Oceanic and Atmospheric Sciences, Oregon State University, Corvallis, where he is currently a Full Professor. He is also the Secretary of the Navy/Chief of Naval Operations Chair of Oceanography. He is also the Head of the ARGUS Program for nearshore remote sensing. His research interest includes the application of optical remote sensing methods to understand the dynamics of the nearshore ocean.



William J. Plant (M'93) received the B.S. degree in physics from Kansas State University, Manhattan, in 1966 and the M.S. and Ph.D. degrees in physics from Purdue University, West Lafayette, IN, in 1968 and 1972, respectively.

He is a Principal Research Scientist with the Applied Physics Laboratory, University of Washington, Seattle, where he is the past Chairman. From 1971 to 1973, he was a National Research Council Postdoctoral Research Associate with the Naval Research Laboratory (NRL), Washington, DC. In 1973, he was with the staff of NRL and remained there until 1988, serving as the Head of the Ocean Measurements Section during the final three years. In 1988, he moved to the Woods Hole Oceanographic Institution, Woods Hole, MA, as a Senior Scientist before coming to the Applied Physics Laboratory in 1991. In 1995, he was a Visiting Scientist with the Max-Planck-Institut für Meteorologie, Hamburg, Germany, and in 2000, he was a Visiting Scientist with the Rosenstiel School of Marine and Atmospheric Sciences, University of Miami, Coral Gables, FL, where he is an Adjunct Professor with the Division of Applied Marine Physics. He has served as an Associate Editor of the *Journal of Geophysical Research* and the *Journal of Oceanic Engineering*. He has authored or coauthored over 80 scientific and technical publications and has coedited two books. The primary objectives of his research are to investigate the microwave scattering from rough water surfaces and to develop algorithms to obtain the geophysical information from such scattering.

Dr. Plant was awarded the Distinguished Technical Achievement Award by the IEEE Oceanic Engineering Society in 1993. In 2003, he was awarded the John Wesley Powell Award by the U.S. Geological Survey.

Characteristics of Internal Waves in the South China Sea Observed by a Shipboard Coherent Radar

William J. Plant, *Member, IEEE*, William C. Keller, Kenneth Hayes, and Gene Chatham, *Member, IEEE*

Abstract—In 2005 and 2007, a coherent X-band radar was deployed in the South China Sea on two different ships. In both cases, the two parabolic antennas of the radar were fixed at grazing angles of approximately 2° looking toward the bow of the ship. The radar transmitted and received through a single antenna but alternated between the two antennas approximately every half second. One antenna was horizontally polarized and the other was vertically polarized. The data were analyzed by computing normalized radar cross sections and scatterer velocities as a function of ground range and time. Surface signatures of internal waves were obvious in both types of image and at both polarizations as regions of enhanced cross sections or scatterer velocities. The collected imagery showed that at least two different types of internal waves exist in the South China Sea: small, nearly sinusoidal trains of waves and large soliton-like waves. These different types traveled at very different speeds and interacted with each other. The small nearly sinusoidal waves traveled at phase speeds near 1 m/s that appeared to increase as the small wave trains were overtaken by the faster solitons. Combined with other shipboard measurements, the radar measurements yielded the widths, maximum velocities, and strain rates of the solitons as well as the dependence of phase speed on amplitude. When the speeds of both the ship and the solitons were removed, the measurements showed that soliton full-widths at half-maximum ranged from about 0.5–4.5 km. These widths showed a dependence on the amplitude of the soliton. The phase speeds of the solitons also depended on their amplitude, reaching 3 m/s in deep water but only about 1.2 m/s in shallow water. CTD profiles were used to estimate an interface depth for a two-layer fluid model of the propagation of the solitons. The phase speeds predicted by this model agreed well with the observed dependence of the soliton phase speed on amplitude in both shallow and deep water.

Index Terms—Coherent radar, internal solitons, internal wave speed, South China Sea.

I. INTRODUCTION

TWO sets of shipboard radar measurements were made in the South China Sea as part of the Non-Linear Internal Wave Initiative (NLIWI) of the Office of Naval Research (ONR). In 2005, our X-band coherent radar called RiverRad [1] was mounted on the *R/V Revelle* and made measurements in the South China Sea from April 18 to May 14. These measurements were all made in deep water. In 2007, we operated RiverRad on two cruises. One from April 24 to May 13 was in the relatively shallow water of the western shelf of the South China Sea while the second from May 13 to May 20 was in deep water.

Manuscript received January 06, 2011; accepted March 16, 2011. Date of publication June 16, 2011; date of current version July 01, 2011. This work was supported by ONR under Grants N00014-05-1-0244, N00014-08-1-0977, and N00014-10-10318.

Associate Editor: W. Carey.

The authors are with the Applied Physics Laboratory, University of Washington, Seattle, WA 98115 USA (e-mail: plant@apl.washington.edu).

Digital Object Identifier 10.1109/JOE.2011.2133030

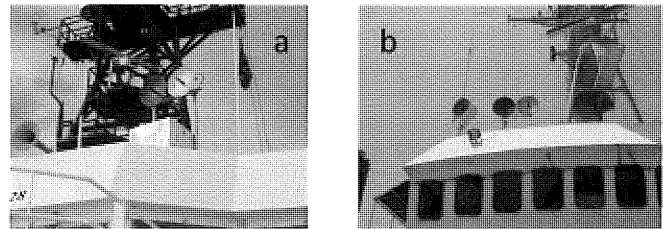


Fig. 1. (a) The parabolic antennas of RiverRad are shown mounted on the *R/V Revelle* in 2005. (b) RiverRad mounted on the Taiwanese ship *R/V Ocean Researcher 1* in 2007.

On all these cruises, the parabolic pencil-beam antennas were pointed approximately in the direction of the ship's heading. Fig. 1 shows RiverRad mounted on these two ships while Fig. 2 indicates where in the South China Sea significant nonlinear solitons were encountered.

RiverRad collects the in-phase and quadrature components of the time series of microwave fields backscattered from the ocean. Using these time series, Doppler spectra are computed via Fourier transformation and the zeroth, first, and second moments of the spectra are computed and stored along with the Doppler spectra. From the three recorded moments, we obtained the normalized radar cross section (NRCS or σ_0 , a measure of surface roughness), the mean scatterer velocity (the ocean surface velocity if wave breaking does not occur and the Bragg wave phase speed is removed), and the spread in scatterer velocities for each range bin averaged over a scan time (365 ms). The velocity spread is not discussed in this paper. The NRCS was obtained from the mean received power using the radar equation along with a calibration constant which we had determined on our laboratory antenna range. This determination used a carefully oriented corner reflector and a moveable mount for the antenna. Maximizing the return from the corner reflector and utilizing its known cross section allowed us to determine the calibration constant to within about 1 dB. More details of the calibration procedure are given in [2].

II. METHODS

Fig. 3 shows the types of data collected on these cruises. Fig. 3(a) and (b) shows space-time plots of scatterer velocities and normalized radar cross sections, respectively; they will be explained further below. The standard shipboard measurements of wind speed and direction, ship speed, heading, and track, acoustic Doppler current profiler (ADCP) currents, and global positioning system (GPS) information were collected and recorded. From the ADCP measurements, currents were extracted from the nearest good bin to the surface and resolved into components parallel and perpendicular to the ship heading

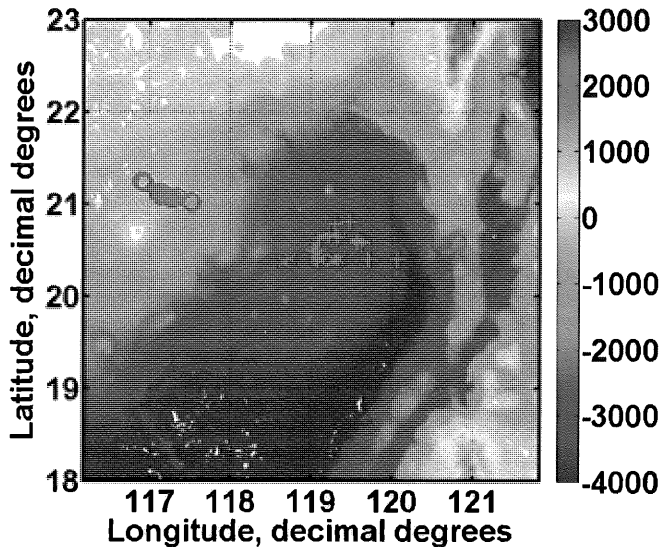


Fig. 2. Locations at which nonlinear internal solitons were encountered in the South China Sea. Shallow water, 2007 = \circ ; deep water, 2007 = \times ; deep water, 2005 = $+$.

as shown in Fig. 3(c). In 2005, the nearest good bin to the surface was 17 m below the surface; in 2007, it was 52 m deep. Latitude, longitude, time, pitch, and roll from the ship's GPS were recorded during the cruise. We also had a GPS receiver mounted on the RiverRad antennas and its speed readings were used to correct the radar Doppler shifts.

Images of the scatterer velocity are shown in Fig. 3(a) while images of σ_o are shown in Fig. 3(b). These images are space-time plots of the return to the radar along the antenna-look direction, the direction of the ship's heading. The vertical axis is distance along the ship's heading from the start of the run. The black dotted curves in the images show the location of the ship. Note how the currents of the soliton advect the ship. The radar return starts about 250 m in front of the ship and goes out to almost 2 km. The antennas were 18 m above the water surface so the incidence angle ranged from 85.9° to 89.5° . This type of display places the radar return at the location it has for a stationary observer if the ship's heading is constant, as it was here.

III. RESULTS

Surface signatures of two types of internal waves, small nearly sinusoidal waves and a larger soliton wave, are clearly present in both the velocity and cross section measured by the radar. As indicated by the sign of the ADCP-measured soliton current along the heading and the lack of soliton current perpendicular to the heading, the ship was traveling directly opposite the direction of propagation of the large internal wave. The train of smaller sinusoidal internal waves with a wavelength of less than 800 m is observed in both the surface currents and cross sections in front of the large soliton. Both the surface velocity and the cross section of the smaller waves increase significantly over the large internal wave. Apparently the interaction of the soliton and the smaller wave train increases the amplitude of

the small wave train. In fact the small wave train is difficult to observe after the ship has passed the soliton, indicating that it may have been blocked by the soliton.

With some caveats discussed below, the slope of these surface features is the speed of the internal wave if the perpendicular ADCP current is zero. If the internal waves do not propagate directly toward or away from the radar, then the magnitude of the feature is the maximum possible speed of the internal wave. The train of small internal waves is clearly visible in the radar return, but is barely visible in the currents measured at 17-m depth. This makes it difficult to determine their direction of propagation except that a component of their propagation vector comes toward the ship because the slope, dR/dt , is negative. We can say with certainty that the train of small internal waves is moving much more slowly than the soliton since we know the direction of soliton travel. Crests of the wave train require a longer time to travel a given distance than do the soliton crests. Thus the speed of the train is smaller than that of the soliton no matter what direction it travels. Furthermore, the speed of a small-wave crest appears to increase as it approaches the crest of the soliton because the slope of the crest, dR/dt , becomes more negative, i.e., larger in magnitude. The apparent phase speeds of the small waves increase from 0.9 m/s away from the soliton to 1.8 m/s at the crest.

This, however, may not be the true speed of the wave train near the crest of the soliton. Modulation of the amplitude of the small wave train by the soliton causes the slope of the small wave train in the image to change. This can cause difficulties in determining the speed of either the small wave train or the soliton. Fig. 4 illustrates the problem. The figure shows a soliton, which we assume to travel at 3 m/s, overtaking a small wave train traveling in the same direction at 1.0 m/s. Fig. 4(a)–(e) shows the two types of waves and their interference pattern at various times as seen in a frame of reference moving with the soliton. The interference pattern determines the surface currents and therefore the intensity of the radar backscatter [3]. The amplitude modulation of the small waves by the soliton causes the peak of the intensity pattern to shift back and forth with respect to the peak of the soliton. The resulting motion of the peak of the pattern in an earth-fixed frame of reference is shown as the solid black line in Fig. 4(f). While the peak moves at an average speed of 3 m/s over long times, for shorter periods (several seconds) it moves at a speed which is neither that of the soliton nor of the short wave train. This means that the slopes of the very intense lines in both cross section and velocity images of Fig. 3 near the soliton peak do not yield a true phase speed. Fig. 4 indicates that the location of either edge of the interference pattern is a better indicator of the phase speed of the soliton than is the peak of the pattern. In this paper, we concentrate on the properties of the large solitons and determine their phase speeds from the edges of the interference pattern.

Many characteristics of the observed solitons can be determined from plots such as those shown in Fig. 3. From the ADCP measurements, the maximum current (at 17- or 54-m depth) produced by the internal wave, V_{max} , can be determined and the time taken by the ship to travel across the soliton, t_w , can be measured. Furthermore, from the plots of along and cross track

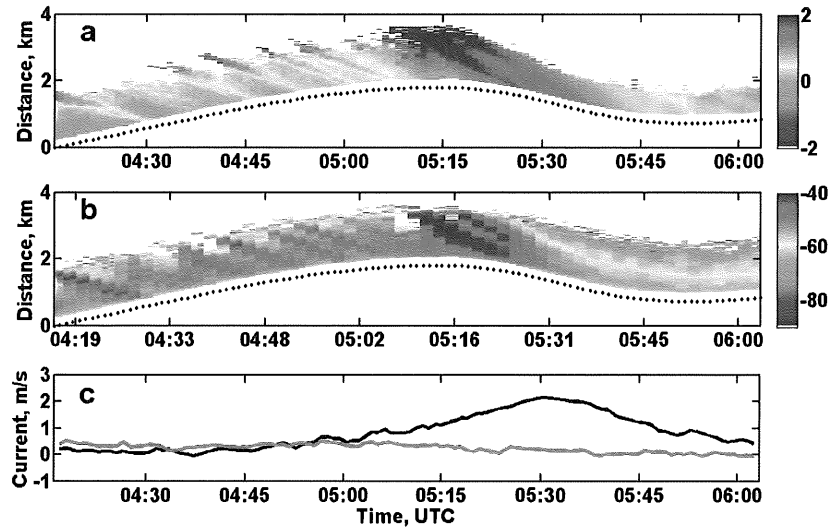


Fig. 3. Data collected from the *R/V Revelle* on April 28, 2005 averaged over 50 s. (a) Radar scatterer velocities in meters per second in the direction of the ship's heading as functions of distance in the heading direction and time. The curve of black dots is the ship's location. (b) Same as a but for the normalized radar cross section, σ_o (VV) in decibels. (c) ADCP current at 17-m depth parallel (black, positive toward antenna) and perpendicular (green, positive toward starboard) to the ship's heading. Wind speed = 2.4 m/s, wind direction (from) = 221° T, ship speed at locations away from internal waves = 0.5 m/s, ship heading = 80° T. Currents were measured at 17-m depth in deep water. The location of the measurements was (20.59° N, 119.59° W).

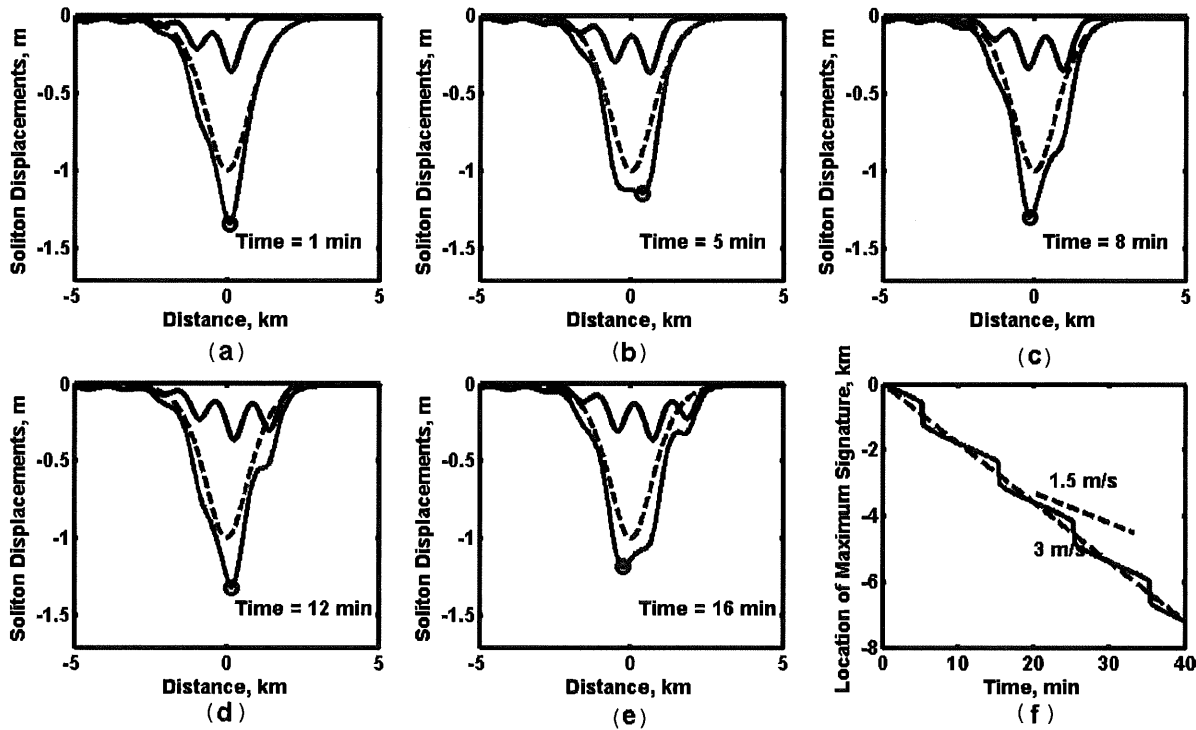


Fig. 4. The effect of interference between a train of short internal waves (upper solid line) and a large soliton (dashed line) on the location of the peak of the interference pattern (lower solid line). The soliton is moving toward negative locations at 3 m/s while the short wave train is moving in the same direction at 1 m/s. Panels (a)–(e) are in a frame of reference moving with the soliton. The peak of the interference pattern is shown in panels (a)–(e) by the circle. Panel (f) shows the motion of this peak in an earth-fixed reference frame. Note that while the long-term motion of the peak of the pattern is at the speed of the soliton, its short-term speed is neither that of the soliton nor the short wave train.

ADCP velocities, the angle, θ , of the ship track to the propagation direction of the internal wave can be determined. Therefore, the slope of the intense features in either radar image, dR/dt , is equal to the internal wave phase speed, c_{iw} divided by $\cos \theta$. If the ship heading is constant, we can also obtain the width of the

soliton W from

$$W = c_{iw}t_w + \cos \theta \int_0^{t_w} V(t)dt$$

where V is the ship speed, c_{iw} is positive and $\theta = 0$ when the ship travels against the internal wave. In this analysis, t_w was

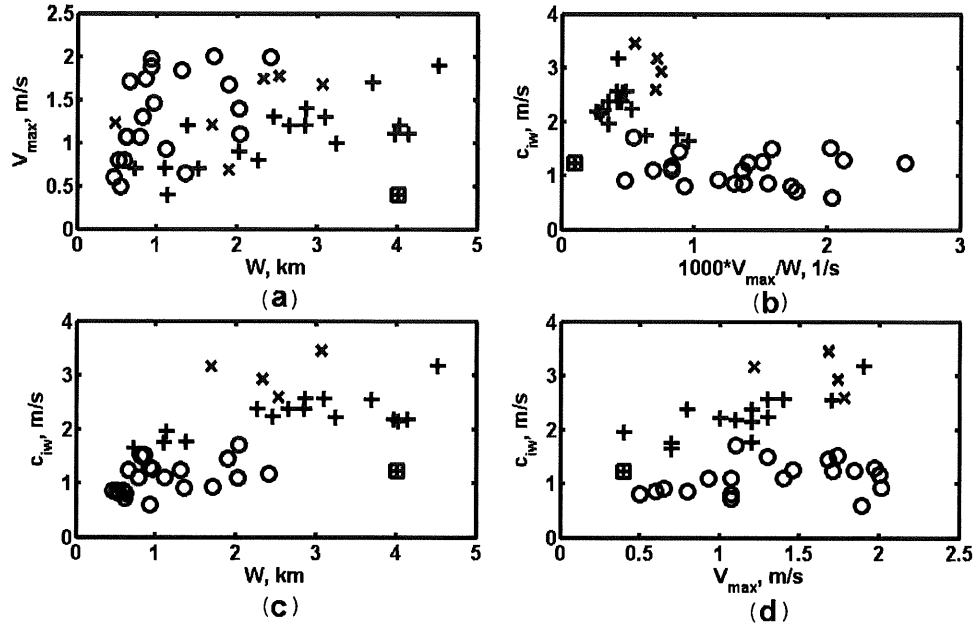


Fig. 5. Measured internal wave properties in deep (+, 2005 and x, 2007) and shallow (o, 2007) water. The value enclosed in a square indicates a somewhat anomalous data point.

taken to be the time between the points at which the internal wave current was half its maximum value. Thus W is the full width of the soliton at half its maximum amplitude.

The relationship between these characteristic quantities is shown in Fig. 5. Fig. 5(a) shows V_{\max} versus W . The maximum current generated by the soliton increases with its width more quickly in shallow water than in deep. The scatter in the data makes it difficult to characterize this dependence precisely. Nevertheless, widths of solitons are generally larger in deep water but maximum currents are comparable. This behavior is characteristic of shoaling waves and may cause the internal waves to break on the continental shelf. Fig. 5(b) shows c_{iw} versus V_{\max}/W , which is proportional to the maximum strain rate of the soliton. Deep and shallow water data are well separated in this plot and show that strain rates of deep-water solitons are generally smaller than those in shallow water. Deep-water solitons also move faster than shallow-water ones. Fig. 5(c) and (d) shows that soliton phase speeds increase with both their width and their maximum velocity.

The maximum surface velocity of the soliton is, of course, related to its amplitude. Fig. 5(d), therefore, shows that the phase speed of the soliton depends on its amplitude, as expected for a nonlinear wave. We may investigate this dependence farther by making a two-layer fluid approximation [4]. In this approximation, the baroclinic linear phase speed of an internal wave is given by

$$c_o^2 = g \left(\frac{\Delta\rho}{\rho} \right) \left(\frac{h_1 h_2}{h_1 + h_2} \right) \quad (1)$$

where g is gravitational acceleration, ρ is the mean density of the two layers, $\Delta\rho$ is the density difference, h_1 is the depth of the top layer, and h_2 is the depth of the bottom layer. In deep water, h_2 is very large so

$$c_o^2 = g \left(\frac{\Delta\rho}{\rho} \right) h_1. \quad (2)$$

In the weakly nonlinear approximation, the phase speed of an internal wave given by Helfrick and Melville [5] is

$$c_{iw} = c_o + \frac{\eta_o \alpha_1}{3} \quad (3)$$

where η_o is the amplitude of the internal wave and

$$\alpha_1 = \frac{3c_o(h_1 - h_2)}{2h_1 h_2}.$$

But, because the horizontal velocity is the derivative of the velocity potential with respect to x , the equations given by Apel [4] show that

$$V_{\max} = -\frac{\eta_o c_o}{h_1}.$$

Therefore

$$c_{iw} = c_o - \left(\frac{V_{\max}}{2} \right) \left(\frac{h_1 - h_2}{h_2} \right)$$

which becomes in deep water

$$c_{iw} = c_o + \frac{V_{\max}}{2}.$$

Thus in this approximation, the phase speed of an internal wave is linearly proportional to the maximum current it generates.

We fit our data to this two-layer fluid model by adjusting the values of $\Delta\rho/\rho$, h_1 , and h_2 . CTD casts were taken on the three cruises and we used them to check the viability of the resulting values. The comparison between the densities used in the two-layer fluid model and those measured using the CTDs is shown in Fig. 6. (The density anomaly is the density in kg/m^3 minus 1000.) The fitted parameters seem to set the density interface at

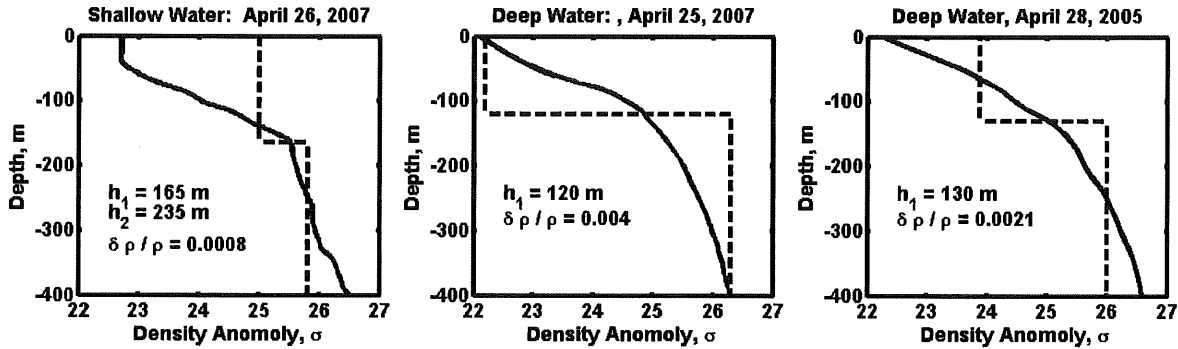


Fig. 6. Comparison of the density structure of the two-fluid model (dashed lines) with that measured by CTDs (solid lines).

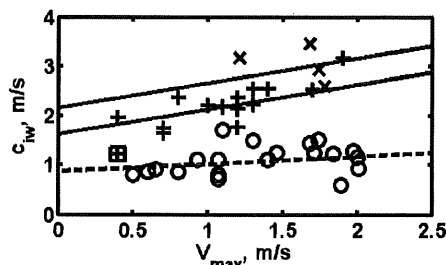


Fig. 7. Internal wave phase speeds determined from radar measurements (symbols) compared with the predictions of a weakly nonlinear two-layer fluid model. Symbols are as follows: + deep water, 2005; o shallow water, 2007; x deep water, 2007. Again, the x within the square is the anomalous data point.

a reasonable depth but yield somewhat strange densities for the two fluids.

Comparisons of the two-layer fluid model using these parameters to our radar-measured, internal-soliton phase speed are shown in Fig. 7. The measurements appear to conform to theory quite well using our chosen parameters. Note especially that the rate of increase in measured phase speeds in deep water is fit well by the model and that this rate of increase does not depend on the parameters obtained from fits to CTD data shown in Fig. 6. In deep water, these parameters simply determine the vertical position of the predicted line.

IV. CONCLUSION

This study has shown that the internal waves in the South China Sea that travel as solitons conform well to theory. The maximum horizontal surface velocity, or current, induced by these waves increases with their width. The phase speed of the solitons increases with both their maximum current and their width. When plots of phase speed versus maximum current are compared with the predictions of a two-layer fluid model, the comparison is quite good using parameters reasonably consistent with CTD data.

These solitons share the South China Sea with smaller internal waves that travel as trains of nearly sinusoidal waves and propagate much more slowly than the solitons. These smaller waves interact with the solitons, increasing their amplitudes as they are overtaken by a soliton. Maximum phase speeds of the

solitons in deep water are about 3 m/s while in shallow water they travel at about 1 m/s. By contrast, the smaller trains of waves move at speeds less than 1 m/s in deep water.

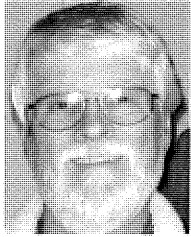
The results presented here are generally consistent with other studies of internal solitons in the South China Sea [6]–[8]. All studies show that the solitons move faster than the linear phase speed. The study by Alford *et al.* finds firm evidence that larger waves travel faster [6]. However, that study concludes that the weakly nonlinear form, (3), under predicts the increase with wave amplitude, in contrast to the present study. Finally, the narrowing of the internal waves as they propagate onto the continental shelf found by Alford *et al.* is also observed in our measurements as shown by Fig. 5(a), although considerable overlap between deep and shallow water width exists.

ACKNOWLEDGMENT

The authors would like to thank J. Klymak and R.-C. Lien for providing the CTD data. They also gratefully acknowledge the crews of the *R/V Reville* and the *R/V Ocean Researcher I*, who both provided excellent conditions in which to conduct this study.

REFERENCES

- [1] W. J. Plant, W. C. Keller, and K. Hayes, "Measurement of river surface currents with coherent microwave systems," *IEEE Trans. Geosci. Remote Sensing*, vol. 43, no. 6, pp. 1242–1257, 2005.
- [2] W. J. Plant, E. A. Terray, R. A. Pettit Jr., and W. C. Keller, "The dependence of microwave backscatter from the sea on illuminated area' correlation times and lengths," *J. Geophys. Res.*, vol. 99, no. C5, pp. 9705–9723, 1994.
- [3] W. J. Plant, W. J. W. C. Keller, K. Hayes, G. Chatham, and N. Lederer, "Normalized radar cross section of the sea for backscatter: 2. Modulation by internal waves," *J. Geophys. Res.*, vol. 115, no. C09033, 2010.
- [4] J. R. Apel, *Principles of Ocean Physics*. New York: Academic, 1987, pp. 231–231.
- [5] K. R. Helfrich and W. K. Melville, "Long nonlinear internal waves," *Annu. Rev. Fluid Mech.*, vol. 38, pp. 395–425, 2006.
- [6] M. H. Alford, R.-C. Lein, H. Simons, J. Klymak, S. Ramp, Y. J. Yang, D. Tang, and M.-H. Chang, "Speed and evolution of nonlinear internal waves transiting the South China Sea," *J. Phys. Ocean.*, vol. 40, 2010.
- [7] C. R. Jackson, "An empirical model for estimating the geographic location of nonlinear internal solitary waves," *J. Atom. Ocean. Tech.*, vol. 26, pp. 2243–2255, 2009.
- [8] J. M. Klymak, R. Pinkel, C.-T. Liu, A. K. Liu, and L. David, "Prototypical solitons in the South China Sea," *Geophys. Res. Lett.*, vol. L11607, 2006.



William J. Plant (M'93) received the B.S. degree in physics from Kansas State University, Manhattan, and the M.S. and Ph.D. degrees from Purdue University, West Lafayette, IN, in 1966, 1968, and 1972, respectively.

He is currently a Principal Research Scientist with the Applied Physics Laboratory, University of Washington, Seattle. He is the past Chair of the Air Sea Interaction and Remote Sensing Department at the Laboratory. He was with the Naval Research Laboratory, Washington, DC, from 1971 to 1988, serving as Head of the Ocean Measurements Section during the final three years. In 1988, he moved to the Woods Hole Oceanographic Institution, Woods Hole, MA, before coming to the Applied Physics Laboratory in 1991. In 1995, he was a Visiting Scientist at the Max-Planck-Institut für Meteorologie, Hamburg, Germany. In summer 2000, he was a Visiting Scientist at the Institut de Recherche sur les Phenomenes Hors Equilibre, Luminy, France. From 2000 to 2001, he was a Visiting Scientist at the Rosenstiel School of Marine and Atmospheric Sciences, University of Miami, Miami, FL. He was an Adjunct Member of the USGS Hydro21 committee from 1999 to 2009. He is an Adjunct Professor in the Division of Applied Marine Physics at the University of Miami.

Dr. Plant has served as an Associate Editor of the IEEE JOURNAL OF OCEAN ENGINEERING and the *Journal of Geophysical Research*.



William C. Keller received the M.S. degree in physics from the University of Tennessee, Knoxville, in 1960.

He is an expert in microwave remote sensing of wind-disturbed water surfaces. He joined the Applied Physics Laboratory, University of Washington, Seattle, in 1992 after 32 years at the Naval Research Laboratory, Washington, DC. He has published extensively in various journals such as the *Journal of Geophysical Research*. His journal publications contain several significant advances leading to

currently accepted theories for microwave scattering by ocean surface waves, including experimental verification of the composite surface theory, the use

of Doppler shift to measure the orbital velocity of ocean surface waves, the concept of the ocean wave-radar modulation transfer function, and the effect of the sea-air temperature difference on the ocean radar cross section. Microwave scatterometers that he designed are used by many organizations. His current interest is remote sensing of ocean surface winds, waves, and currents using microwave radar operated from blimps and aircraft.



Kenneth Hayes received the B.S. degree in electrical engineering from the University of Maryland, College Park, in 1968.

He joined the Applied Physics Laboratory, University of Washington, Seattle, in 1991, coming from Bendix Corporation, where he was a Field Engineer. He specializes in computer systems management, applications programming, and the development of data acquisition systems. His primary field of application is ocean remote sensing where he is concentrating on real-time data acquisition and processing. His experience ranges over airborne, satellite, and shipboard field experiments. He is developing data acquisition systems that will yield surface wind information from scatterometry, and analysis programs to interpret synthetic aperture radar images of the ocean.

of the ocean.



Gene Chatham (S'05-M'06) received the B.S. degree in electrical engineering from the University of Washington, Seattle, in 2006.

He began his work at the Applied Physics Laboratory, University of Washington, Seattle in 2005 as an undergraduate student, and stayed on after graduation to work professionally for the laboratory. With his mechanical background as a former machinery technician in the U.S. Coast Guard, he specializes in designing and fabricating electrical circuits and electro-mechanical systems.

Wave Shadowing and Modulation of Microwave Backscatter from the Ocean

William J. Plant and Gordon Farquharson
Applied Physics Laboratory
University of Washington

September 26, 2011

Abstract: Shadowing and modulation of microwave backscatter by ocean waves are studied using coherent X-band radars. Two types of shadowing are investigated: geometric shadowing (complete blockage of incident rays) and partial shadowing (diffraction combined with weak scatterers). We show that, at a particular range (grazing angle), received power levels less than or equal to the noise level of the radar occur primarily where the incident power is low. Furthermore, in some cases, the fraction of samples of received power near the noise level depends on polarization. Since geometric shadowing should not depend on either the incident power level or the polarization, we conclude that it plays little role in microwave backscatter from the ocean at low grazing angles. Comparison with Milder's (2003) prediction of the fraction of a rough surface that is illuminated under geometric shadowing assumptions confirms this conclusion. We also study the modulation of microwave backscatter by ocean waves using these data. Phase differences between received power and scatterer velocity are found to depend on polarization and antenna look direction. Modulation patterns at VV polarization appear to be rather well explained by standard composite surface theory, having phases between power and velocity that are positive looking upwave and negative looking downwave. For HH polarization, however, other effects, probably due to breaking, come into play and overshadow composite surface effects of free waves. These breaking wave effects cause the modulation phase difference to be near zero for upwave looks and near 180° for downwind looks. A simple model, linear in long wave slope, that involves both breaking and freely-propagating waves but does not include any shadowing effects is shown to account for observed phase differences at both polarizations to within about 10° . Both the shadowing and modulation results are very relevant to ongoing attempts to measure phase-resolved ocean waves using shipboard radars. They imply that at VV polarization, cross section modulation is closely related to wave slope and height but at HH polarization, both the cross section and the scatterer velocity modulation are more closely related to breaking waves.

1. Wave Modulation and Shadowing of Microwave Backscatter

Radars are being widely used to monitor the sea surface today due to the dependence of the backscattered signal on winds, ocean surface heights, currents, and long ocean waves. They are generally deployed for these purposes on satellite, aircraft, ship, tower, and land-based platforms. Currently many efforts are underway to extract phase-resolved ocean waves from backscatter received by shipboard radars. For these efforts to be successful, modulations of received phase, power, and scatterer velocities must be related to ocean wave heights. Because these measurements are made at low grazing angles, shadowing may contribute to these relationships,

in contrast to the situation at higher grazing angles. Here we investigate shadowing and modulation of microwave backscatter by ocean waves.

As the angle between the boresite of the antenna and the mean sea surface (the nominal grazing angle) decreases, a point is reached where rays from the antenna to a location on the sea surface may be blocked by intervening surface displacements. If this blockage is considered to be complete, it is called geometric shadowing. Areas of the surface that rays cannot reach are considered to send no radiation back to the antenna. Because of its relative simplicity, much theoretical effort has been devoted to geometrical shadowing (Beckman, 1965; Smith, 1967; Brown, 1980; Bourlier et al., 2002; Milder, 2004). However, experimental evidence that geometrical shadowing actually occurs in microwave backscatter from the ocean is lacking. In fact, many theoretical and modeling studies of microwave backscatter from the ocean at low-grazing angles indicate that it does not occur (Barrick, 1995; Holliday et al., 1995; Sturm and West, 1998; Johnson et al., 2009). Diffraction in the regions of large surface displacement causes electric currents to be set up on the surface even in the geometrically shadowed areas, allowing them to send radiation back to the antenna. We shall refer to this type of shadowing as partial shadowing.

We may consider effects of the possible types of rough-surface shadowing on the modulation of backscattered power by ocean waves as shown in Figure 1. Incoming rays are indicated by slanting lines from the left. Figures 1a and c (left-hand panels) show geometric shadowing at low and high incident power levels. Increasing the incident power can only increase the return in the illuminated areas. By the very definition of geometric shadowing, the change in power level cannot affect the regions that are not illuminated so the probability of observing signals at the noise level cannot change. Also note that geometric shadowing is a ray theory so the polarization of the incident radiation is irrelevant. By contrast, Figures 1b and d (right-hand panels) show cases of partial shadowing at low and high incident power levels. In this case, backscatter can come from the areas that are geometrically shadowed but may be reduced either because the incident field is reduced or because scatterers in this region are weaker than in the illuminated areas due to their modulation by waves. Both of these processes may be polarization dependent. If the incident power level is low, the radar may still observe signals at the noise level in areas behind a crest as shown in Figure 1b. In practice, the difference between the modulations of received power diagrammed in Figures 1a and b may be difficult to distinguish. However, for partial shadowing, an increase in the incident power level may raise the backscatter from behind the crests above the noise level as shown in Figure 1d. Thus either changing the incident power level or noting polarization differences may allow differentiation between geometric and partial shadowing.

As noted by Poulter et al (1994), shadowing of either type is essentially an additional contribution to the ocean wave/radar modulation transfer function (MTF) (Plant, 1989). Thus it is difficult to discriminate between wave-induced modulations of scattered power when the incident field remains constant and those caused by shadowing variations in incident power. Modeling may be useful in this respect and the evidence of the most accurate models (generally one-dimensional) is that backscatter does occur from regions that would be geometrically shadowed. Figure 2a illustrates this with a plot from Johnson et al. (2009) where according to geometrical shadowing ideas, only the points marked by the asterisks should be illuminated. The wave modulation shown in this figure is in line with the measurements we report below. For much of our HH polarized data, the range resolution was 30 m. Figure 2b shows the backscatter of Figure 2a, which has a 2.34 m resolution, averaged to a 30 m resolution. The modulation

appears to be comparable to that shown in Figure 2c, which is from our actual measurements with 30 m resolution.

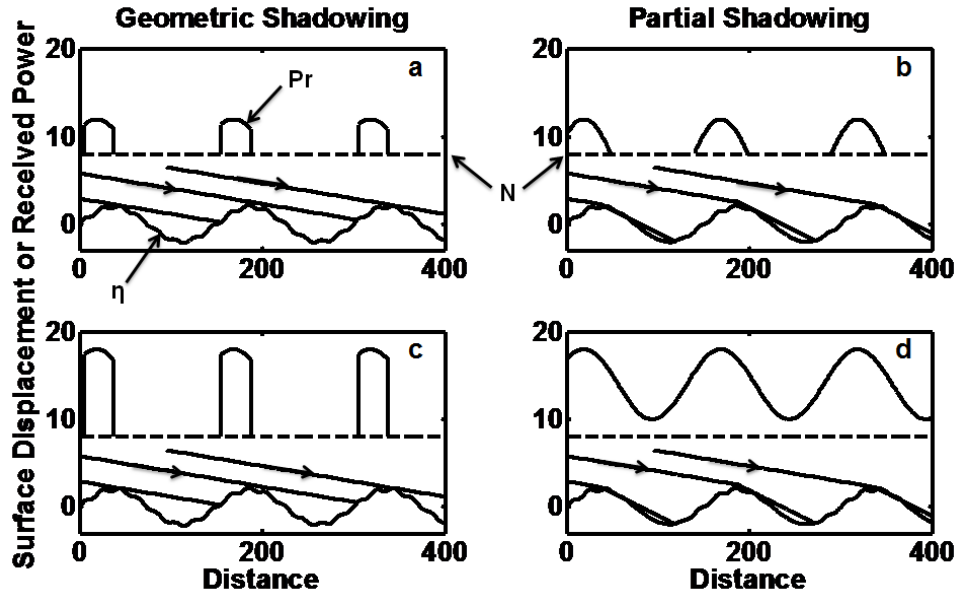


Figure 1. Diagrams of geometric and partial shadowing at low and high incident power levels. P_r is received power, N is the radar noise level indicated by the dashed line, and η is the sea surface. a) geometric shadowing, low incident power; b) partial shadowing, low incident power; c) geometric shadowing, high incident power; d) partial shadowing, high incident power.

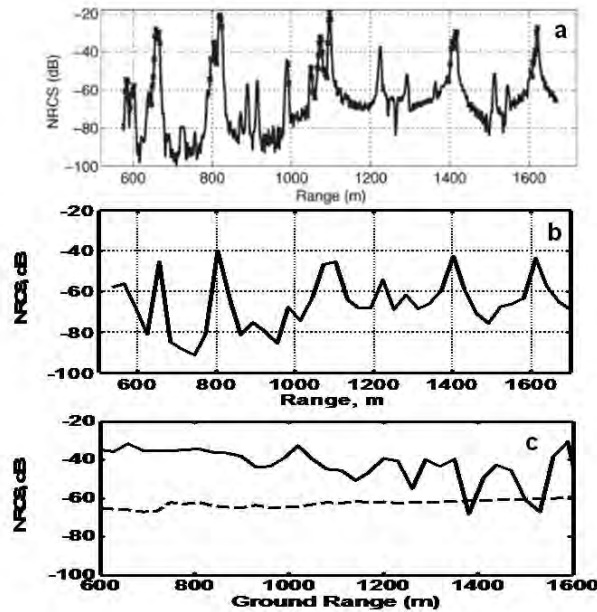


Figure 2. a) Backscatter from a simulated sea surface at X-band and HH polarization with a 10 m/s wind speed looking upwind (from Johnson et al., 2009). Range resolution is 2.34 m. b) The same simulation averaged to a 30 m resolution. c) Return observed in this study at X-band and HH polarization with a 11.7 m/s wind speed and the antenna looking 26° from upwind. Range resolution is 30 m. Solid lines in both panels are normalized radar cross sections (NRCS) while the dotted line in the lower panel is the noise-equivalent NRCS for the radar.

In the absence of shadowing, at moderate grazing angles, the modulation of microwave backscatter has long been viewed as an effect of the orbital velocities of long ocean waves on the received phase, power, and scatterer velocity. In this standard composite surface theory, these orbital velocities are considered to advect, tilt, and modulate freely propagating, wind-generated waves of a few centimeters in length (Keller and Wright, 1975; Alpers and Hasselmann, 1978). More recently Plant (1997) has shown that some features of microwave backscatter cannot be explained by this theory, namely the difference in mean Doppler shifts in HH and VV polarized backscatter, and the observation that ocean wave height variance spectra can be derived from high-incidence-angle microwave backscatter at VV polarization but not from HH polarized backscatter. He proposed that breaking or crumpling of meter-length waves modulated by longer waves could account for these effects. Here we will attempt to determine whether these ideas can be applied at low grazing angles or whether shadowing effects must be added.

We will use a series of data sets that we have collected over several years with coherent, X-band radars to investigate wave-induced shadowing and modulation of radar backscatter from the sea. Because our radars are coherent, we can investigate modulations in both the received power and the scatterer velocities obtained from Doppler spectra but the data were monostatic so the phase of the received signal cannot be investigated. We will use the difference in dependence of geometric and partial shadowing on incident power level and polarization to attempt to determine which occurs in practice. We examine the probability that the signal received from the sea surface is at or near the noise level. We do this for several cases with both VV and HH polarizations. During our measurements the wind and waves varied and the antenna boresite changed. We compare these results with predictions from geometric shadowing theories for the fraction of the surface that is shadowed. We will find that geometric shadowing does not explain the observations. We will then go on to examine the coherence function between received power and scatterer velocity. We will show that the phase difference between these two quantities depends on polarization and antenna look direction in ways that can be modeled by bound wave/free wave concepts (Plant, 1997; Plant et al, 1999a,b; Plant et al, 2004; Gade et al., 1998; Rosenberg et al., 1999). Shadowing does not appear to be necessary to explain the observed phase differences.

2. Radars and Experiments

Three similar coherent, X-band radars were used in this study. All processed the raw received fields, linearly detected, into received power, Doppler offset, and Doppler bandwidth in real time. All three radars coherently averaged about 20 pulse returns to increase the signal-to-noise ratio. One radar, designed and built at the Applied Physics Laboratory of the University of Washington, APL/UW, operated on an airship (the US-LTA 138S) and collected the data to be shown here in 1995 (See Figure 3a). A description of this radar and its specifications are given in Weissman et al, 2002. This is the only one of the radars that did not use a parabolic, or pencil-beam, antenna. Rather its antenna was a single, slotted waveguide antenna eight feet long that operated in a fixed or windshield-wiper (oscillating) mode with HH polarization. Data shown here were collected in deep water off the Oregon coast with the antenna fixed and the airship nearly stationary. A range resolution of 7.5 m was used.

The second radar called RiverRad was also developed at APL/UW and was originally intended to measure flow in rivers. In this study, RiverRad was operated on a Taiwanese ship, the R/V Ocean Researcher 1 (OR1), in deep water in the South China Sea and on the beach at the

Corp of Engineers Field Research Facility in Duck, North Carolina, where it observed the coastal zone.

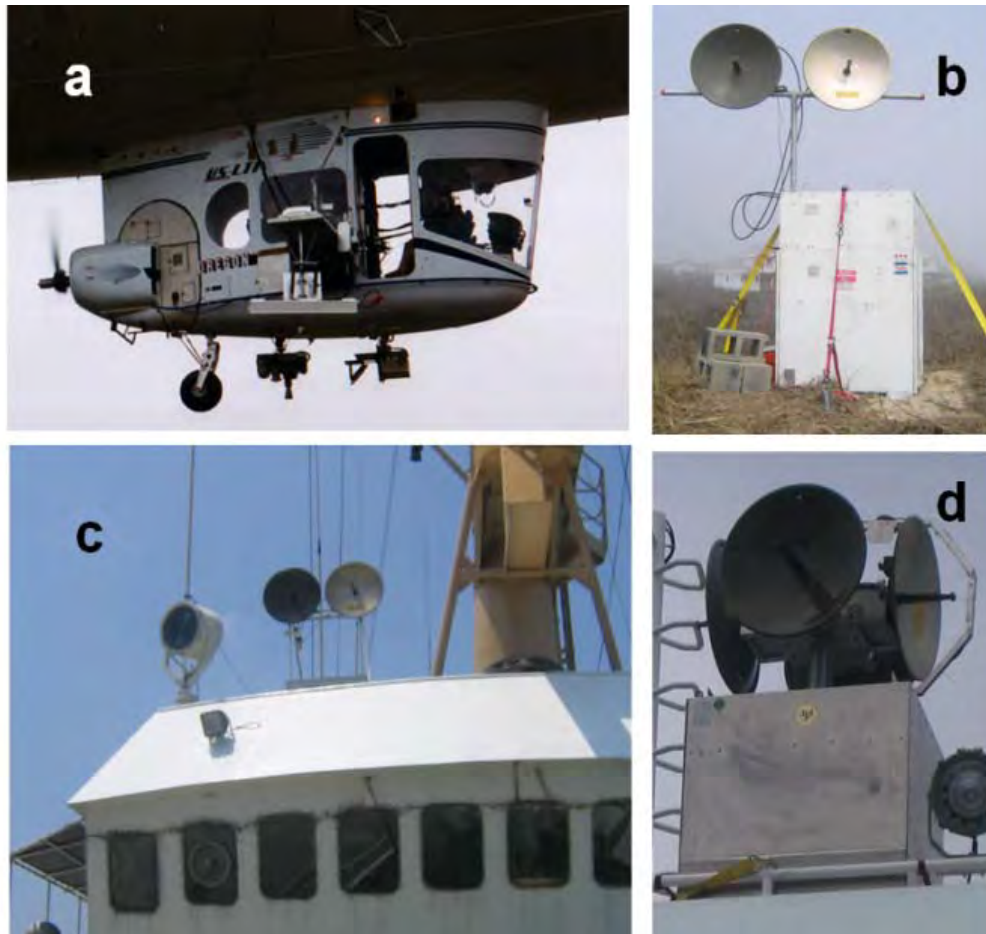


Figure 3. a) The white waveguide antenna of the coherent radar on the US-LTA 138S airship, b) RiverRad set up on the beach at the Corp of Engineers Field Research Facility in Duck, NC, c) RiverRad on the R/V Ocean Researcher1 d) CORAR on the R/V Thompson.

RiverRad transmits a series of pulses from one of its two parabolic antennas and receives backscattered signals through the same antenna. After 262 msec, RiverRad switches to its second antenna. One antenna operates with VV polarization and the other with HH. Detailed specifications for RiverRad are given in Table 1. RiverRad's range resolution was 30 m on Ocean Researcher 1 but 7.5 m at Duck. Figure 3b shows RiverRad set up on the beach at Duck while Figure 3c shows it on the Ocean Researcher 1 in the South China Sea. Note that on the ship, RiverRad's antennas were fixed looking toward the bow.

The final radar called CORAR (COherent Real Aperture Radar) differs from RiverRad primarily in supporting four rotating parabolic antennas, switching between two of them on a pulse-to-pulse basis then switching approximately every 41 msec to the second pair (See Figure 3d). CORAR was also constructed at APL/UW. In this study, CORAR was operated from the deck of the R/V Thompson during a cruise along the US west coast with VV polarization on all antennas. Table 1 also gives the specifications of CORAR.

Characteristic	RiverRad	CORAR
Frequency (GHz)	9.36	9.375
Polarization	HH and VV	VV
Pulse Width (nsec)	50 or 200	50
Pulse Width (MHz)	20 or 5	20
Pulse Width (m)	7.5 (Duck) or 30 (SCS)	7.5
Pulse Rate (Hz)	39062.5	50000
Rate per Antenna (Hz)	39062.5	25000
Time between pulses (μsec)	25.6	20.0
Max possible number of range bins	512 or 256	400
Number of range bins used	256	252
Number of Pulses Collected	10240	1024
Number of Pulses Averaged	20	16
Time to Collect Samples (msec)	262.1	41.0
Time for Calculations (msec)	102	0
FFT Size	512	64
Sample Rate (Hz)	1953.1	1562.5
Freq Resolution (Hz)	3.8	24.4
Nyquist Freq (Hz)	976.6	781.3
Rotation Period (sec)	Not rotating	13
Rotation Rate (deg/sec)	Not rotating	27.7
Rotation Az Res (deg)	Not rotating	1.1
Antenna Length (feet)	2.0	2.0
2-Way Hor Ant Beamwidth (deg)	2.6	2.6
Antenna Width (feet)	2.0	2.0
2-Way Vert Ant Beamwidth (deg)	2.6	2.6
Antenna Gain (dB)	34.9	34.9
Total Az Resolution (deg)	2.6	3.7
Max Range (km)	1.9	1.9
Az Resolution at Max Range (m)	87	123

Table 1. Specifications of two of the coherent X-band radars used in this study, RiverRad and CORAR.

Since the variation of incident power, and therefore received power, as a function of range is of primary importance in this study, we show in Figure 4a the pattern of received power for a constant NRCS for our radars with pencil-beam antennas. Figure 4b shows the comparable pattern for a typical marine radar with a 23° vertical beamwidth. These patterns were computed using the radar equation:

$$P_r = \frac{P_t \lambda^2 G^2 \sigma_s}{(4\pi)^3 R^4}$$

where P_r is the power received from the sea surface, P_t is the total transmitted power, λ is microwave length, G is the antenna pattern, R is range, and σ_s is the cross section of the sea. Here we used

$$G = G_o \exp \left\{ -\frac{(\theta_g - \theta_o)^2}{(\Delta\theta)^2} \right\}$$

where θ_g is grazing angle, negative corresponding to an upward-looking antenna, θ_o is the nominal grazing angle (the antenna boresite),

$$G_o = 4\pi/(\Phi_v\Phi_h)$$

and

$$\Delta\theta = \Phi_v/(2\sqrt{\ln 2}).$$

Φ_v and Φ_h are the one-way, full, half-power, vertical and horizontal beam widths of the antenna. The cross section of the sea is given by

$$\sigma_s = \sigma_o(\sqrt{2}\rho R\Phi_h/\cos\theta_o)$$

where σ_o is the NRCS and ρ is the range resolution.

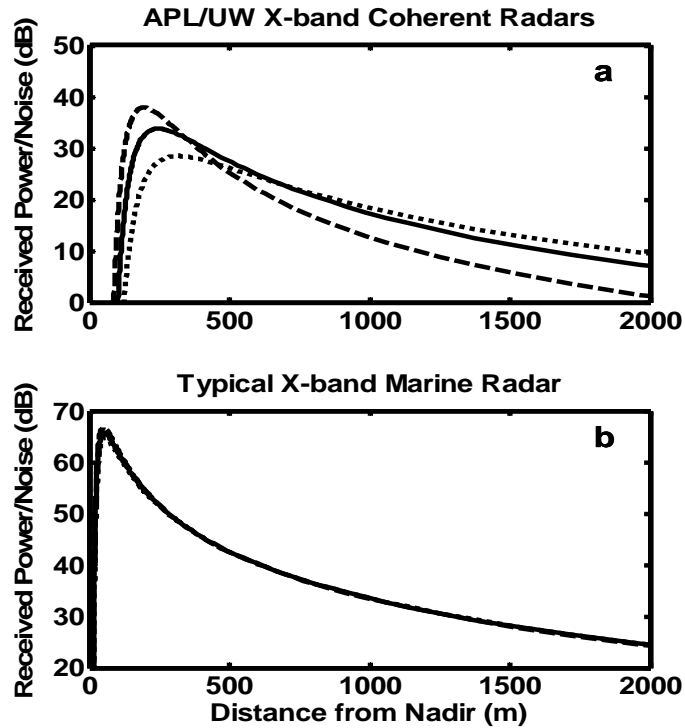


Figure 4. Power received from a sea surface with an NRCS of -30 dB divided by system noise versus ground range. a) pattern for the pencil-beam antennas used in these experiments. b) pattern for a typical marine radar. Dotted lines indicate an antenna boresite of 0.5° ; solid lines, 1.5° ; dashed lines, 2.5° .

To make the plots in Figure 4, we have normalized P_r by the noise level of the radar, N , and assumed a constant σ_o of 0.001 (-30 dB). Values of P_r/N shown in Figure 4a should be accurate for RiverRad but 7 dB should be added for CORAR. Both Figures 4a and b show plots of P_r/N for three values of antenna boresite, 0.5° , 1.5° and 2.5° . Note that for the APL/UW radars the pattern of received power changes significantly while for the marine radar, the change is barely detectable. The marine radar would require changes in boresite of 5° to 6° to produce changes in the received power pattern comparable to that seen in the APL/UW radars with a 1° change.

The noise level N was determined for the APL/UW radars by finding the lowest return power level during multiple runs looking at the ocean. This value was spot checked by determining the spectral density of Doppler spectra well away from the sea return spectrum and calibrating to yield the noise power level. The two methods of determining N were found to agree well.

3. Wave Shadowing Results

For all of the data collected with the three radars, we computed the signal-to-noise ratio, SNR:

$$\text{SNR} = \frac{P_r' - N}{N} = \frac{P_r}{N}$$

where P_r' is the received power from the sea surface plus noise. Note that SNR values can be directly compared with P_r/N given in Figure 4. We then determined the fraction of the data from various runs that had $\text{SNR} < 1$. We will call this fraction the concealed fraction since the signal, if any, is smaller than the system noise and therefore concealed from detection. Each sample of received power was averaged only over the time that the radars took to collect them, either 262 msec or 41 msec. Each data set contained in excess of 300 data points at each range bin, each of which yielded a value of SNR. The number of SNR values less than one was then determined and divided by the total number of samples for that range bin for that run.

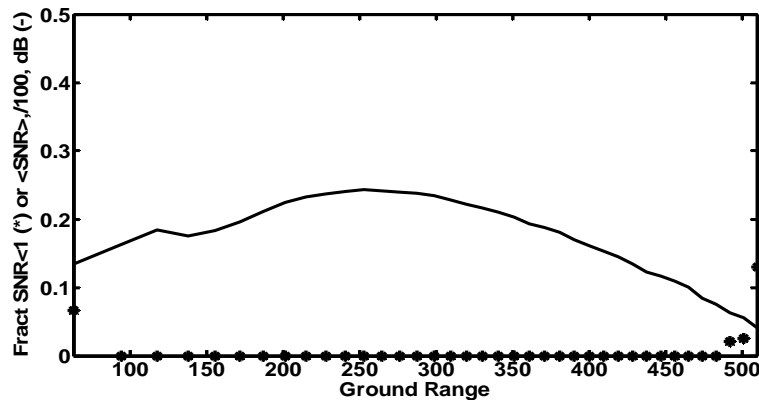


Figure 5. Data collected on the US-LTA 138S airship in 1995 with HH polarization for grazing angles between 24.8° and 78.2° . The solid curve is the average signal-to-noise ratio, SNR, in dB divided by 100 and the asterisks show the fraction of SNR values having $\text{SNR} < 1$, the concealed fraction. Wind 12.6 m/s from 173°T , antenna boresite 55° looking toward 180°T . Range resolution in 7.5 m .

Average SNR values in dB divided by 100 and the concealed fractions at various ranges for the data set collected on the airship are shown in Figure 5. The antenna height was 240 m so the grazing angles for the ranges shown are from 24.8° to 78.2° . In this range of grazing angles, shadowing is not expected and the concealed fraction becomes non-zero only where the incident power is low. This shows that, as expected, weak scatterers can produce very low backscatter even in the absence of shadowing if the incident power level is low.

Figure 6 shows plots of the same quantities at both HH and VV polarizations for data taken on the Ocean Researcher 1 in 2007. The wind speed was relatively low, 5 m/s, and the antenna look direction was 37° from upwind. Under these conditions, not much shadowing seems to occur and where it does, it must be partial shadowing, since the concealed fraction becomes appreciable primarily where the incident power level is low. Differences between HH and VV polarizations are difficult to discern at far ranges where the incident field has dropped well below its maximum value. However, at ranges around 900 m, where the incident field has dropped but not so far, concealed fractions at HH are larger than those at VV. This is probably due to the fact that HH scatterers are weaker than those at VV when breaking is not involved (see Section 4) so HH scatterers will be hidden by system noise before VV scatterers. Once weaker scatterers at both polarizations are hidden by noise, at the farther ranges, then concealed fractions would be expected to be more nearly equal.

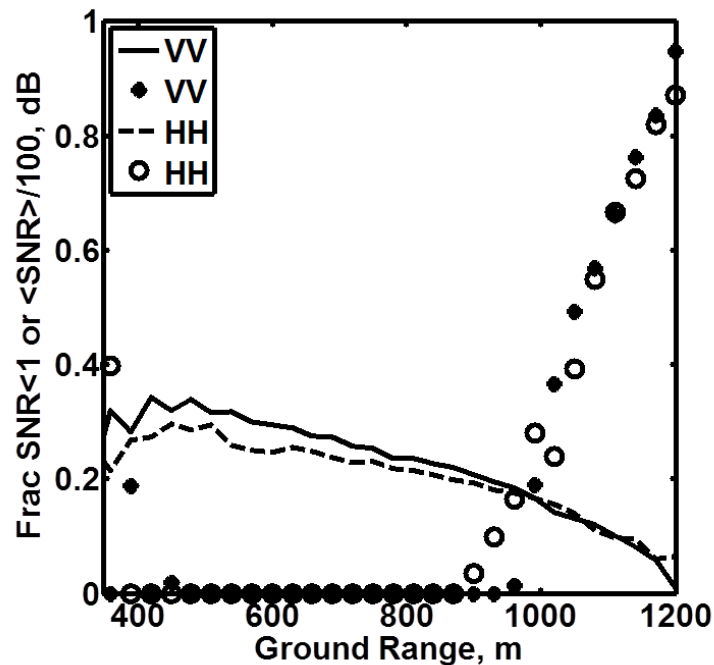


Figure 6. Average SNR in dB divided by 100 (curves) and concealed fraction (symbols) for data collected on the Ocean Researcher 1 in 2007. Wind 5 m/s from 317° T, antenna boresite 0° to 0.25° looking toward 280° T. Range resolution is 30 m.

Figure 7 shows data (VV only) taken on the R/V Thompson at higher wind speeds. Now the concealed fraction is significant even where the incident power is high. This could indicate that some geometric shadowing is taking place. However, the concealed fraction exhibits much different behavior than predicted by Milder (2004) whose result is shown as the dashed line in Figure 7. This was computed as the fraction shadowed

where f is Milder's fraction illuminated, which he gives in his Eq.3.7 as

where α is the tangent of the grazing angle and σ is the rms slope of the rough surface. Milder says that this result is valid when $\alpha \gg \sigma$. We show values when $\alpha \approx \sigma$. For σ we have used the wind-speed dependent results of Cox and Munk (1954) for a slick-covered surface, which makes σ as small as possible and therefore f_s as small as possible. We see that even using this small rms slope, the predicted fraction shadowed is generally larger than observed concealed fraction except at grazing angles in the near range where the theory says that geometrical shadowing should not occur. Furthermore, in the data, the concealed fraction decreases with increasing wind speed while the theory predicts the opposite. If the theory is correct, and other theories of geometric shadowing are very similar, then again geometrical shadowing does not appear to explain the observations.

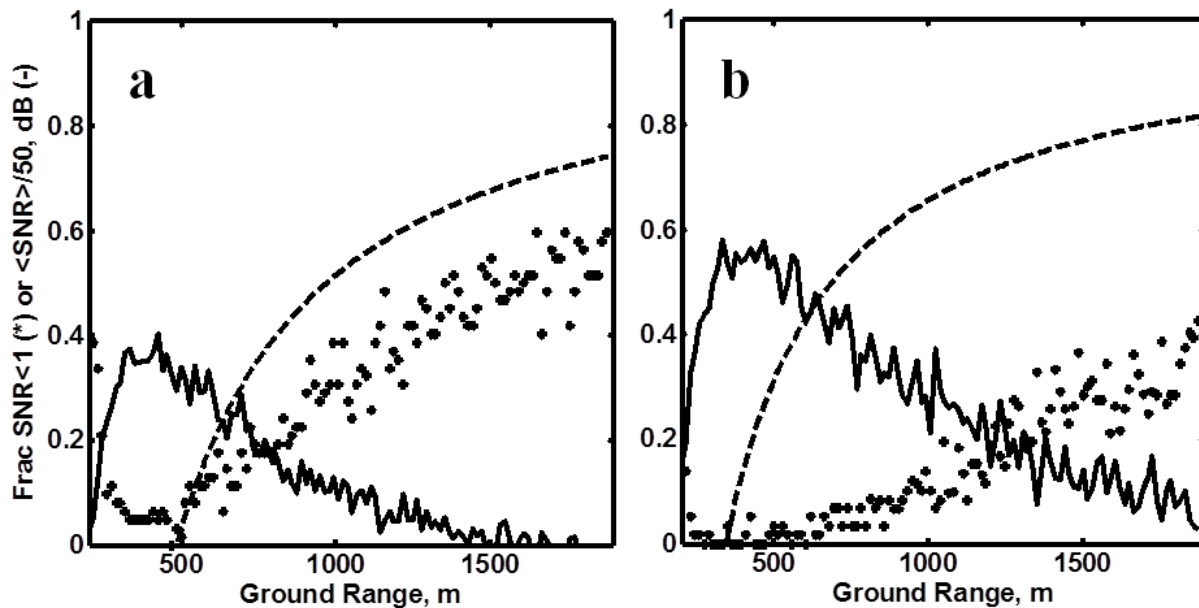


Figure 7. Average SNR in dB divided by 50 (solid curve) and concealed fractions (asterisks) as function of range for data taken on the R/V Thompson at VV polarization. The dashed curves are the predictions of Milder's geometrical shadowing theory discussed in the text. a) Wind 7.3 m/s from 9°T, antenna boresite 1° to 2° looking toward 7.5°T. b) Wind 16.9 m/s from 341°T, antenna boresite 1° to 2° looking toward 342.5°T. Range resolution is 7.5 m

In the data discussed so far, the decrease in incident power for any particular set of environmental and radar parameters was always correlated with a decrease in grazing angle. Thus it could be argued that the increase in concealed fraction at far ranges could be due to the decreasing grazing angle, and subsequent increasing shadowing, rather than to the decreasing incident power. To investigate this possibility, we look for changes in concealed fraction as a function of antenna boresight angle due to the motion of the ship. Changes in boresight angle

will change the amount of incident power on the surface at a particular range (see Figure 4a). However, at a particular range the grazing angle is always the same. Thus, if we see a change in concealed fraction at a particular range for different boresight angles, we know that the change must be due to a change in incident power, rather than due to shadowing at low grazing angles.

To carry out this analysis, we examined data taken on the Ocean Researcher 1 at a wind speed of 11.7 m/s. The pitching of the ship varied the boresite of the antennas. In order to determine the boresite during data collection, we smoothed the received power in range and found the range at which it maximized. Modeling the backscatter using the radar equation and estimates of the NRCS (similar to Figure 4) allowed us to determine the antenna boresite from the range at maximum received power. Figure 8 shows the result of binning the backscatter into two boresite ranges that were 1° apart. In the boresite range 0° to 0.5° (Figure 8a), the average SNR was higher and the concealed fraction was lower than in the boresite range 1° to 1.5° (Figure 8b) for every range above 1000 m. Yet the grazing angle at any particular range was the same for both boresites. This shows that the increase in concealed fraction is due to the decreased incident power for larger boresites and not due to a change in grazing angle. This again indicates partial shadowing, not geometric shadowing.

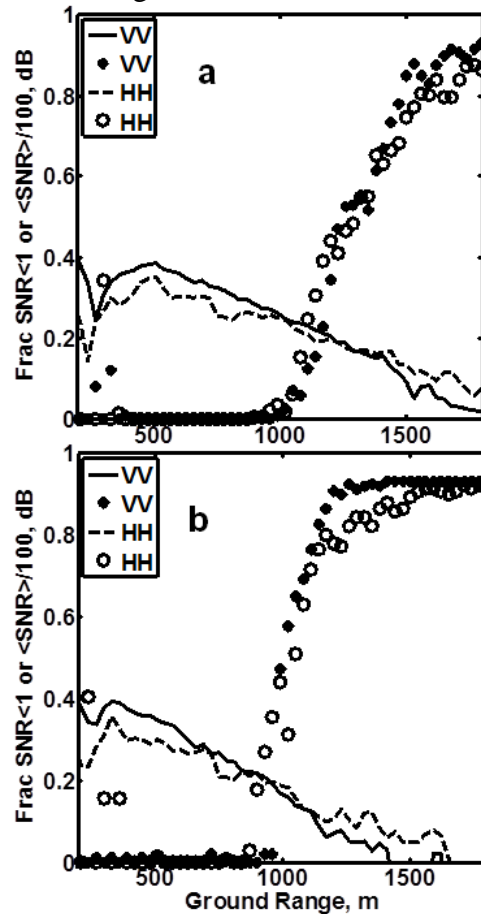


Figure 8. Average SNR in dB divided by 100 and concealed fractions for two different boresite angles (top and bottom) for data taken on the OR1 in 2007. Wind: 11.7 m/s from 25° T. a) Boresite = 0.0° to 0.5° looking toward 51° T. b) Boresite = 1.0° to 1.5° looking toward 51° T. Range resolution is 30 m.

Note that concealed fractions for HH and VV polarizations are very similar, as we also found in Figure 6. However, HH concealed fractions again seem to rise faster than those at VV when the incident power has not fallen too far (ranges around 900 – 1000 m). This would be expected if HH scatterers are weaker than VV ones. When incident power levels have fallen farther but SNR values are comparable (ranges 1000 m to 1250 m), concealed fractions at the two polarizations are comparable, probably because weak scatterers at both polarizations have fallen to the noise level. However, in this data set at ranges beyond about 1250 m, the SNR for VV falls below the HH values while VV concealed fractions rise above the HH ones. This is understandable if the reduction in SNR at VV below that at HH is due to the V pol incident field being weaker than the H pol one. All of this gives little reason to believe that there is significant shadowing for either HH or VV.

Finally, we examine the data taken by RiverRad in the coastal zone at Duck, NC when the antennas were pointing perpendicular to the shoreline. Figure 9 shows the data obtained under three very different wind and wave conditions. In all cases, the concealed fraction increases with

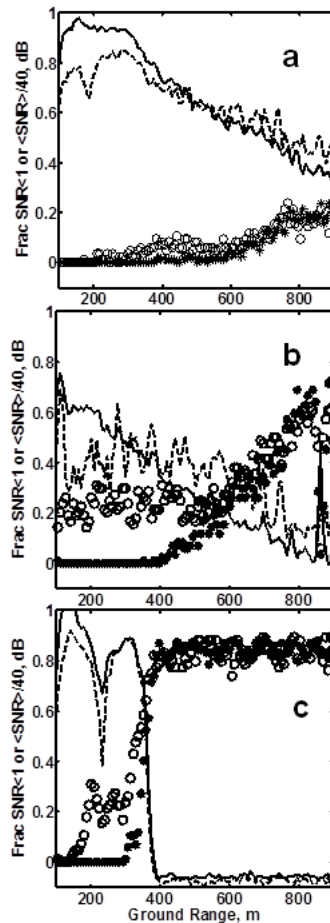


Figure 9. Average SNR in dB divided by 40 (curves) and concealed fractions (symbols) obtained from signals received by RiverRad from the coastal zone at Duck, NC. Solid lines and asterisks are for VV polarization, dashed lines and circles are for HH polarization. The antennas were directed perpendicular to the shoreline toward 20°T at a boresite of 1.5°. a) Wind 14.0 m/s from 16°T (onshore), b) Wind 5.8 m/s from 353°T (alongshore), c) Wind 3.0 m/s from 83°T (onshore).

decreasing incident power, as usual. For the lowest wind case, 3.0 m/s, however, the increase is rather obviously due to the weak scatterers for ranges larger than 400 m. In all three cases, the concealed fraction is larger for HH polarization than for VV when the incident power is high, ie, for ranges between 200 and 500 m in Figures 9a and 9b and for ranges between 200 and 400 m in Figure 9c. This polarization difference clearly indicates that the shadowing is not geometric. It may also indicate that more power is incident on geometrically shadowed regions for VV polarization than for HH. The difference is difficult to estimate because it is not clear whether the cross sections at the two polarizations are the same. If they are, then the ratio of concealed fractions indicate that the VV-to-HH ratio of incident power in geometrically shadowed regions is in general greater than 2 or 3. If, however, cross sections at HH are lower than those at VV, as is likely, then the VV-to-HH ratios of incident power in shadowed regions could be considerably larger.

4. Wave Modulation Results

Ocean surface waves modulate both the power received by the radar and the Doppler shifts of the return signal. This modulation may be caused by orbital velocities of long surface waves, their tilting of the centimetric waves that cause microwave backscatter, wave breaking, or shadowing. We investigated wave modulation of microwave backscatter by determining the phase of the coherence function between wave-induced modulations in the received power and scatterer velocities. Scatterer velocities, V_s , were determined from the first moment, f_1 , of the Doppler spectrum through the standard equation

$$V_s = \frac{\lambda f_1}{2 \cos \theta_g}.$$

These V_s values were then corrected for SNR (Plant et al.,1998). Since we measure power and velocity as functions of range, the coherence function is a function of wavenumber. It is given by

$$\gamma(k) = \frac{\langle P_r(k) V_s^*(k) \rangle}{\sqrt{\langle |P_r(k)|^2 \rangle \langle |V_s(k)|^2 \rangle}}$$

where $P_r(k)$ and $V_s(k)$ are Fourier transforms of the spatial variations of received power, $P_r(x)$, and scatterer velocity, $V_s(x)$, which have been detrended. The asterisk indicates the complex conjugate. Detrending was done by subtracting power or velocity filtered over four range bins; powers were in decibels. Angle brackets indicate averages over a number of realizations. In order to reduce the uncertainty in the measurement of the phase of the coherence function (the phase difference between wave-induced power and velocity modulations), a large number of realizations of these spectra must be averaged. The 95% confidence interval for the measured mean phase, ϕ_m , of γ is $\pm \epsilon$ where

$$\cos^2 \epsilon = |\gamma|^{-2} - 20 \frac{2}{N} (|\gamma|^{-2} - 1)$$

and N is the number of individual cross spectra averaged (Bendat and Pierson, 1966). For the examples to be presented below, $N \geq 480$.

Figure 10 shows the magnitude and phase of the coherence functions for HH and VV polarization looking upwind and downwind for data taken in the South China Sea. This data set was collected with a 30 m range resolution so only modulation by waves longer than 60 m ($k < 0.105$ rad/m) can be observed in the coherence function. We consider up/down wave to be up/down wind. Some problems existed with wind directions produced by the anemometer on the ship so we have used QuikSCAT data at the location of the ship to determine wind direction. Wind speeds from the shipboard anemometer seemed to be in agreement with QuikSCAT wind speeds. In the figure, positive phases indicate that maxima of received power modulations occur closer to the radar than maxima of scatterer velocity modulations. The figure shows a clear dependence of the phase between received power and scatterer velocity on both look direction and polarization.

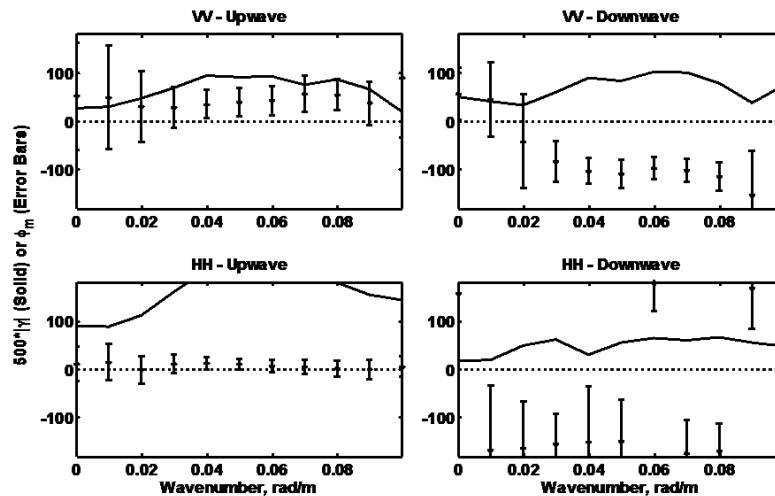


Figure 10. Magnitude and phase of the coherence function between wave-induced variations in received power and scatterer velocity. Magnitudes are solid lines and phases are asterisks with 95% intervals shown. Upwave and downwave measurements were made within three hours of each other. The wind speed was 10.6 m/s from 45 °T and the antenna looked toward 45 °T during the upwave measurements. The wind had not changed but the antenna looked toward 225 °T during the downwave measurements.

For VV polarization, the phase at wavenumbers where waves exist is about +45° looking upwave while it is about -100° looking downwave. For HH polarization, the situation is different since the phase between the received power and the scatterer velocity is near 0° looking upwind and near 180° looking downwind. We can check to see if the scatterer velocity changes signs when the antenna changes from looking upwind to looking downwind at HH polarization by looking at long-time averaged Doppler spectra of the backscatter looking upwave and downwave. It is well known that due to breaking wave effects at large incidence angles, Doppler spectra at HH polarization occur at higher frequencies than those at VV polarization when looking upwind if positive frequencies correspond to velocities toward the antenna as they do here (Plant, 1997). Therefore, one would expect HH Doppler spectra to be shifted to lower frequencies than VV spectra when looking downwave if water velocities produced by breaking waves were in the direction of wave travel. Figure 11 shows that this is indeed the case. The figure shows mean Doppler spectra for the same data as shown in Figure 10. The relative frequency shift between HH and VV spectra is in the opposite direction looking downwind than

it is looking upwind, as expected. Note that the mean offset of all spectra is due to the ship's motion through the water (The antennas were always looking toward the bow.)

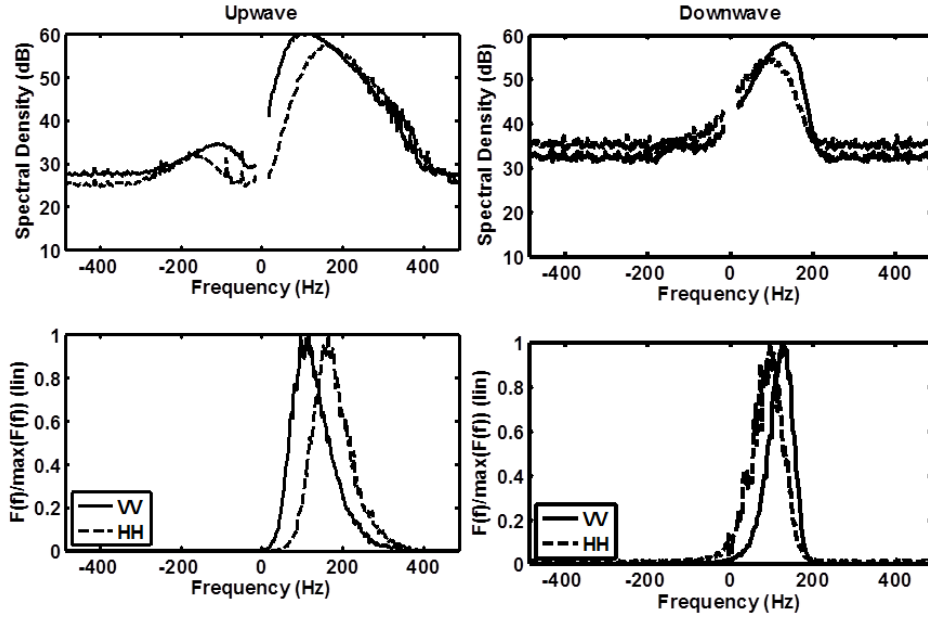


Figure 11. Mean Doppler spectra for the data shown in Figure 10. Positive frequencies indicate velocities toward the antenna. The mean offset is due to the ship's velocity. The upper row shows calibrated spectra such that their integral over frequency yields the NRCS, on dB scales. The lower row shows spectra normalized by their maximum values, on linear scales.

We can model the expected result of wave modulation on a bound wave/free wave picture similar to that invoked earlier in both open ocean and wave tank studies (Plant, 1997; Plant et al., 1999a, 1999b, 2004). The idea is that long waves on the ocean both modulate free, wind-generated capillaries, as the standard composite surface model postulates, and cause intermediate scale waves to break, producing bound or breaking waves. The resultant backscatter is the sum of these processes. Both processes vary with position on the long wave and we simplify the problem by considering these variations only to first order in long wave slope. Then for a sinusoidal long ocean wave,

$$\eta = A \exp\{-i(\mathbf{k}\cdot\mathbf{R}-\omega t)\}$$

we write the (detrended) wave-modulated power and velocities as

$$P_r = \langle P_r \rangle \{F_f [m_h + m_t] + F_b m_b\} k \eta$$

$$V_s = \{F_f + F_b m_v\} \mathbf{\kappa} \cdot \mathbf{C} k \eta$$

where \mathbf{C} is the long wave phase speed, $\mathbf{\kappa}$ is a unit vector in the antenna-look direction, $\langle \rangle$ again indicates an average, here over the time series, F_f is the fraction of backscatter due to free waves, F_b is the fraction of backscatter due to bound/breaking waves, and $k = 2\pi/L$ where L is long-wave length. Note that $F_f + F_b = 1$. The different types of modulation transfer functions are m_h , the hydrodynamic MTF of the free waves; m_t , the tilt MTF of the free waves; m_b , the

bound/breaking wave MTF. The free waves are advected by the long wave orbital velocity, which is written $Ck\eta$. The transfer function m_v accounts for the fact that the amplitude and phase of the bound wave velocity variation is not the same as the long wave orbital velocity. The amplitude of the bound wave velocity is the phase speed of the parent wave producing the bound waves. Phases of the modulations are with respect to the long wave crest and are positive in the direction of wave travel.

The hydrodynamic MTF includes both the modulation of the freely propagating short wave amplitudes and range changes caused by the long wave amplitudes; both are in phase with the long wave. The orbital velocity is also in phase with the long wave. The tilt mtf is always 90° out of phase with the long wave and occurs on the side of the crest toward which the antenna is looking. Finally, Plant (1997) found that the maximum of m_b occurred approximately 130° in front of the long wave crest. We therefore model these MTFs as follows:

$$\begin{aligned}
 m_h &= 2+3/(hk) \\
 m_t &= 15 \exp[+i\pi/2], && \text{upwave} \\
 m_t &= 15 \exp[-i\pi/2], && \text{downwave} \\
 m_b &= 2 \exp[i2\pi(130/180)] \\
 C &= \sqrt{g/k} \\
 m_v &= (2.5/C) \exp[i2\pi(130/180)]
 \end{aligned}$$

where h is the height of the antenna.

We may now determine the behavior of the phase of the correlation function for different polarizations and look directions. Figure 11 shows that bound waves play a little role in VV backscatter since we see no features in its Doppler spectrum at frequencies corresponding to breaking wave velocities. Therefore, we take $F_f = 0.9$ looking upwind and $F_f = 1$ looking downwind. For HH polarization the bound/breaking waves are dominant but a small feature at free wave frequencies can be seen upon close inspection. Therefore, we take $F_f = 0.15$ looking upwind and $F_f = 0.3$ looking downwind. We illustrate the modulation process using a long wave with $A = 1$ m and $L = 100$ m.

Figure 12 shows the result of this simple, first-order simulation. The sea surface is shown by the circles and asterisks, circles representing wind waves and asterisks representing bound/breaking waves. We show the bound waves to cover a phase extent of 60° , in rough agreement with Plant (1997). The sizes of the symbols indicate the importance of free and bound waves in the backscatter at the two polarizations. Even though a first-order model is surely too simple, especially for the bound/breaking waves, the phase differences between received power and scatterer velocity modulations are close to those shown in Figure 10 in all cases. One can see that power and velocities maximize in most cases in regions where geometric shadowing would predict no backscatter (see Figure 1). For VV polarization, the bound/breaking waves make only a minor difference, the shift from $\pm 90^\circ$ phases upwind and downwind being mostly due to the hydrodynamic modulation of the free waves. For HH polarization, on the other hand, bound/breaking waves are crucial.

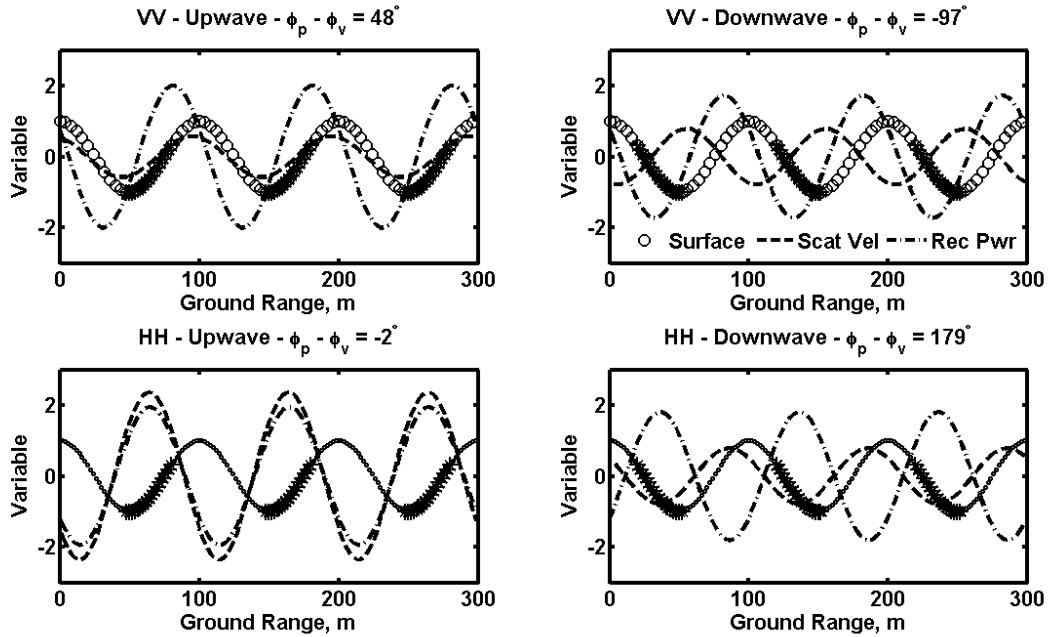


Figure 12. Simulated modulations of received power and scatterer velocity by a sinusoidal long wave of 1 m amplitude and 100 m wavelength. The circles and asterisks are located on the sea surface, circles indicating wind waves and asterisks indicating breaking waves. The relative size of the circles and asterisks indicates their importance in HH and VV backscatter. The dashed curve shows the modulated velocity, and the dash-dotted curve shows the modulated power. Waves in the left panels move to the left, toward the radar, while those in the right panels move to the right, away from radar. The phase differences between power and velocity, $\phi_p - \phi_v$, shown in the figure agree with the measurements shown in Figure 10 to within about 10° .

5. Conclusion

We have shown based on both the probability of finding X-band backscatter near the radar noise level and on the behavior of the wave-induced modulations of backscattered power and scatterer velocities that geometric shadowing is a poor description of data dropouts in low-grazing-angle microwave backscatter from the ocean. The fraction of radar range cells that backscatter at levels equal to the radar noise level we called the concealed fraction and showed that it did not behave as expected based on a geometric shadowing model. It increased much more slowly with decreasing grazing angle than Milder's 2003 predictions, decreased with wind speed rather than increasing as the model predicts, and it always depended on the amount of power incident on the surface. If the shadowing is partial, then the data give little reason to believe that more shadowing of incident power occurs for HH than for VV except in the coastal zone where concealed fractions behaved differently for HH and VV polarizations. The phase difference between the wave-modulated power and velocity was always nonzero for VV polarization and reversed its sign for upwave and downwave antenna pointing directions. For HH polarization, the phase difference was near zero for the upwave antenna look direction but reversed to be near 180° in the downwave case. We were able to give a simple non-shadowing model of wave modulation for which the phase difference between power and velocity modulations matched the observations to within about 10° . A simplified view of this model is

that wave modulation at VV polarization is dominated by the modulation and advection of wind waves as the standard composite surface theory suggests. Power modulations are caused by hydrodynamic, range-change, and tilt modulation but primarily by tilt modulation. Scatterer velocities are in the direction of long wave orbital velocities, maximizing at the crest of the long wave. Therefore they change signs when the antenna changes from upwind to downwind. For HH polarization, on the other hand, breaking wave effects dominate. Thus the maximum backscattered power is located at the same place on the long wave as the maximum scatterer speed. Thus looking upwave, they are in phase but since scatterer velocity changes sign when the antenna changes to downwind, the phase reverses by 180° . These effects account well for the observed phase of the coherence function between wave-modulated power and scatterer velocity.

All of these observations lead us to conclude that geometric shadowing does not play a role in microwave backscatter from the ocean at low grazing angles. A much more likely scenario is that revealed by theoretical studies such as those of Barrick (1995) and Holiday et al. (1995) where the incident microwaves set up surface currents on all parts of the sea surface. This leads to backscattered fields from all parts of the surface, as numerical models show (Sturm and West, 1998; Johnson et al., 2009). The theoretical studies agreed that little shadowing existed for VV polarization but that for HH polarization, incident fields may be significantly reduced, though not to zero, in geometrically shadowed regions of the surface. Barrick summarized his conclusions this way: "The present work shows that on/off (or binary) shadowing descriptions are meaningless for the sea up through the microwave region, especially for vertical polarization." Our experimental evidence supports his conclusion and furthermore suggests that significant shadowing at HH polarization occurs only for steep waves, such as those found in the coastal zone. This conclusion has important implications for the problem of measuring phase-resolved wave fields using shipboard radars. We are pursuing these implications now.

Acknowledgments

This study was made possible by several grants originating in the Office of Naval Research (ONR) including N00014-10-10318, F012919, and APS-11-12. Grant # A100747 from the Bureau of Ocean Energy Management, Regulation and Enforcement (BOEMRE) enabled the study to be completed.

References

- Alpers, W. and K. Hasselmann, The two-frequency microwave technique for measuring ocean-wave spectra from an airplane or satellite, *Bdry Layer Met*, 13, 215-230, 1978.
- Barrick, D.E., Near-grazing illumination and shadowing of rough surfaces, *Radio Sci.*, 30, 563-580. 1995.
- Beckmann, P., Shadowing of random rough surfaces, *IEEE Trans. Ant. Prop.*, AP-13, 384-388, 1965.
- Bendat, J. S., and A. G. Piersol, *Measurement and Analysis of Random Data*, pp. 209-216, John Wiley, New York, 1966.

Bourlier, C., G. Bergin and J. Saillard, Monostatic and bistatic statistical shadowing functions from a one-dimensional stationary randomly rough surface: II. Multiple scattering, *Waves Random Media* 12, 175–200, 2002.

Brown, G.S., Shadowing by non-Gaussian random surfaces, *IEEE Trans. Ant. Prop.*, AP-28, 788-790, 1980.

Cox, C. and W. Munk, Statistics of the sea surface derived from sun glitter, *J. Marine Res.*, 13, 199-227, 1954.

Gade, M., W. Alpers, S. Ermakov, H. Huehnerfuss, and P. Lange, Wind-wave tank measurements of bound and freely propagating short gravity-capillary waves, *J. Geophys. Res.*, 103(C10), 21697-21709, 1998.

Holliday, D., L.L. DeRaad, and G.J.S. Cyr, Volterra approximation for low grazing angle shadowing on smooth ocean-like surfaces, *IEEE Trans. Ant. Prop.*, 43, 1199-1206, 1995.

Johnson, J.T., R.J. Burkholder, J.V. Toporkov, D.R. Lyzengo, and W.J. Plant, A numerical study of the retrieval of sea surface height profiles from low grazing angle radar data, *IEEE Trans. Geosci. Rem. Sensing*, 47(6), 1641-1650, 2009.

Keller, W.C., and J.W. Wright, Microwave scattering and the straining of wind-generated waves, *Radio Sci.*, 10, 139-147, 1975.

Milder, D.M., Surface shadowing at small grazing angles, *Waves Random Media*, 13, 89-94, 2003.

Plant, W.J., The modulation transfer function: Concept and applications, in *Radar Scattering From Modulated Wind Waves*, edited by G. J. Komen and W.A. Oost, 155-172, Kluwer Academic, Boston, Mass., 1989.

Plant, W.J., A model for microwave Doppler sea return at high incidence angles: Bragg scattering from bound, tilted waves, *J. Geophys. Res.*, 102(C9), 21131-21146, 1997.

Plant, W.J., W.C. Keller, V. Hesany, and K. Hayes, Measurements of the marine boundary layer from an airship, *J. Atmos. Ocean. Tech.* 15, 1433-1458, 1998.

Plant, W.J., W.C. Keller, V. Hesany, T. Hara, E. Bock, and M. Donelan. Bound waves and Bragg scattering in a wind wavetank, *J. Geophys. Res.*, 104(C2), 3243-3263, 1999a.

Plant, W.J., “Crumpling” wave effects in backscatter from the air-sea interface, in *The Wind-Driven Air-Sea Interface*, edited by M.L. Banner, Univ. New South Wales, 409-416, 1999b.

Plant, W.J., P.H. Dahl, J.P. Giovanangeli, H. Branger, Bound and free surface waves in a large wind-wave tank, *J. Geophys. Res.*, 109, C10002, doi:10.1029/2004JC002342, 2004.

Poulter, E.M., M. J. Smith, and J . A. McGregor, Microwave backscatter from the sea surface: Bragg scattering by short gravity waves, *J. Geophys. Res.*, 99(C4), 7929-7943, 1994.

Rozenberg, A.D., M.J. Ritter, W.K. Melville, C.C. Gottschall, and A.V. Smirnov, Free and bound capillary waves as microwave scatterers: laboratory studies, *IEEE TGRS*, 37(2), 1052-1065, 1999.

Sturm, J.M., and J.C. West, Numerical study of shadowing in electromagnetic scattering from rough dielectric surfaces, *IEEE Trans. Geosci. Rem. Sensing*, 36(5), 1477-1484, 1998.

Smith, B.G., Geometrical shadowing of a random rough surface, *IEEE Trans. Ant. Prop.*, AP-15, 668-671, 1967.

Weissman, D.E., W.J. Plant, W.C. Keller, and V.G. Irisov, Comparison of scatterometer and radiometer wind vector measurements, *J. Atmos. Ocean Tech.*, 19, 100-113, 2002.

Origins of Features in Wavenumber-Frequency Spectra of Space-Time Images of the Ocean

William J. Plant and Gordon Farquharson

Applied Physics Laboratory, University of Washington, Seattle, WA, USA

plant@apl.washington.edu, gordon@apl.washington.edu

Abstract Wavenumber-frequency spectra from remote sensing systems generally energy along the ocean wave dispersion relation and additional features that lie above and below this relation. At low frequencies a linear feature passing through zero is normally observed while one or more high-frequency features generally exhibit substantial curvature. Such features can be caused by incorrect data processing, such as clipping. In this work, however, we assume that the data have been processed correctly. Then we show that the strongest features above and below the first-order dispersion relation are not primarily due to second-order interactions or wind turbulent eddies. They may possibly be caused by shadowing (mostly at HH polarization) but the most probable cause of these features is wave breaking. The behavior of the features can be explained by the interference of long ocean waves, which causes breaking near local maxima of surface slope. We used X-band Doppler radars in this study. Doppler spectra observed by the radars indicate that the maximum speed reached by water particles on the sea surface (away from coastlines) is almost always less than 5 m/sec with its most likely value being around 3 m/s. Since this is much less than the phase speeds of either dominant wind waves or swell, this indicates that neither of these long waves is the breaking wave. Rather, the superposition of these long waves either steepens or generates short gravity waves on the surface, which then break and produce water parcels travelling near their phase speed, the speed observed by the radar. We show that the most likely speed of these parcels is close to the speed of the linear feature in the wavenumber-frequency spectrum. We therefore suggest that the short gravity wave most likely to break is the one whose phase speed nearly matches the speed of the slow interference pattern that causes the linear spectral feature.

1. Introduction

Data from the ocean surface as a function of both space and time can be obtained by various remote sensing techniques with sufficiently high resolution to produce wavenumber-frequency spectra with little aliasing. Such spectra can be produced either by computing the two-dimensional Fourier transform of a space-time image along a given direction (usually averaged over some perpendicular distance) or by computing three-dimensional Fourier transforms of a time stack of two-dimensional spatial images. When either of these techniques is used, features at frequencies higher than the first-order dispersion relation and linear features running through zero can be seen in the spectra in addition to the feature along the first-order dispersion relation. Data can be obtained at optical, infrared, or microwave frequencies (Frazier and McIntosh, 1996; Smith et al., 1996; Stevens et al., 1999; Dugan, 2001, 2003). While the high-frequency features have generally been attributed to nonlinear wave-wave interaction effects, the linear features have been explained by various means in addition to nonlinear wave effects. The explanations include a jet ski in the image (Dugan, 2001), turbulent wind effects (Dugan, private communication), fronts and foam patches advected by the current (Dugan, 2003) breaking waves (Frazier and McIntosh, 1996; Stevens et al., 1999), and nonlinear scattering effects (Frazier and

McIntosh, 1996; Rino et al., 1997; Stevens et al., 1999) In this paper we investigate the origin of these features as observed by a coherent, X-band microwave radar that was mounted on the R/V Thompson in the summer of 2008. We will assume that no nonlinearities have been introduced into the data by incorrect processing (no clipping or other distortions).

We will first look at the possibility that the linear feature in the spectrum is due to second-order nonlinear wave/wave interaction. Since the pioneering work of Phillips, Longuet-Higgins, and Hasselmann, the importance of nonlinear wave/wave interactions in the nature of surface water waves has been realized (Phillips, 1960; Longuet-Higgins, 1962; Hasselmann, 1962). Most work on nonlinear wave/wave interactions since then has concentrated on third-order (four-wave) interactions because they result in wave products that lie on the first-order dispersion relation in the wavenumber/frequency. Therefore these interactions cause energy to be transferred among spectral components and shift the phase speed of these components slightly from the first-order values (Longuet-Higgins and Phillips, 1962; Hasselmann, 1963; Barrick and Weber, 1977). However, second-order wave/wave interactions also exist and are pointed out in these works. These lie off the first-order dispersion relation in wavenumber-frequency space, and therefore do not cause energy transfer. They do, however, cause detectable effects on the surface displacement (Weber and Barrick, 1977). Since the second-order products lie above and below the first-order dispersion relation in a wavenumber/frequency spectrum, and the low-frequency one can pass through zero, we investigate here whether these interactions can explain features that we have observed with the antennas of our radar directed up and downwind. We will conclude that they cannot both because they are too weak and because the resulting second-order spectral features are not located in the same position in wavenumber-frequency space as the observed features. Furthermore, we will document features observed when looking nearly cross wind that cannot be reproduced by second-order wave-wave interactions. Based on these cross wind data and the observed mislocation of predicted second-order features, we will conclude that no second-order phenomenon, whether hydrodynamic or electromagnetic, can explain the features.

We will then look at other phenomena that could possibly account for the features. We will examine the possibility that shadowing causes the features of interest. We will show that these features exist in microwave data collected at grazing angles well above those at which shadowing can exist. Thus shadowing cannot be the only cause of the features. In light of recent experimental results on the existence of geometric shadowing, we will argue that shadowing is unlikely to be the cause of the features for data taken on the open ocean even at low-grazing angles (Plant and Farquharson, 2011). We will also show that the slope of the linear feature in the spectrum implies that it is caused by something on the ocean surface moving much slower than the wind speed, which shows that turbulent eddies traveling with the mean wind speed cannot cause the features.

Since swell and wind waves coexisted on the ocean at the time of the measurements, we will propose that their interference pattern with each other and within the wind-wave system produce breaking waves that are responsible for both the linear features and the other features that exist at frequencies higher than the first-order dispersion relation. We will show that the interference of the swell and wind waves and within the wind wave system produce features in space/time images that match those seen in our radar imagery. Furthermore, the slower of the features, the linear one, travels at speeds that are comparable to the maximum speeds of water particles that

show up in our Doppler spectra. Since these maximum speeds are well below the phase speeds of either the dominant wind waves or swell, we propose that they are produced by short gravity waves that travel with the interference pattern, are steepened by it, and break to produce water parcels that travel at very nearly their phase speeds.

2. The Experiment

In August 2008, APL/UW operated its coherent, X-band radar, CORAR, onboard the R/V Thompson on a cruise along the northwest coast of the US. In the shipboard configuration, CORAR had four parabolic antennas mounted on a partially stabilized, rotating mount and set at an incidence angle between 88° and 89° . The four antennas were directed 90° apart in azimuth and opposite pairs collected data on alternate pulses at a rate of 25 kHz for each antenna. A switch changed the pair of antennas being used every 41 msec. All antennas were vertically polarized on both transmit and receive. They were parabolic antennas with 3.5° half-power, one-way beamwidths, yielding a two-way pattern 2.5° wide. The radar sampled backscatter sufficiently rapidly that complete Doppler spectra could be obtained at each of 256 range bins, which were 7.5 m wide in these experiments. From these Doppler spectra, zeroth, first and second moments were computed; the zeroth moments were converted to normalized radar cross sections through calibration (Plant et al., 1998) while the first moments were converted to scatterer velocities and second moments yielded the spread of scatterer velocities.. For each look direction, space/time images of both the normalized radar cross section and the scatterer velocity were formed.

Most data on this cruise were collected with the mount rotating. However near the end of the cruise, the antennas were operated without rotation (or stabilization) for nearly a day and these are the data on which we concentrate in this paper. Under these circumstances space/time images could be collected with minimal aliasing so that their wavenumber/frequency spectra were very clean. Figure 1 shows an example of an image and spectrum of surface velocity collected during the cruise with the antenna pointed into the wind at grazing angles near 1° . The first-order dispersion relation containing the clear spectral peak at a frequency of 0.162 Hz and a wavenumber of 0.0915 rad/m is obvious in Figure 1b. Our convention is that features lying in the first and third quadrants represent waves travelling toward the antenna. Therefore the dominant wave is a 6.19 sec wave, 68.6 m long travelling at 11.1 m/s toward the antenna. Since a 68.6 m wave would have a period of 6.63 sec and a speed of 10.35 m/s in the absence of current, these measurements indicate that a component of apparent current of about 0.75 m/s existed in the direction of wave, opposite the direction of ship travel. Since the ship moved at about 0.5 m/s, this implies a current component of about 0.25 m/s in the opposite the direction of ship travel, that is, to the south.

Waves of the dominant period and frequency are also obvious in Figure 1a. A clear modulation of these waves is evident in this space/time image. The modulation pattern has a speed of 3.6 m/s, which is not the group speed of the dominant wave, 5.2 m/s. Figure 1b shows two other features of interest, the feature lying above the first-order dispersion and the nearly linear feature that goes through zero. The linear feature has a speed of 3.6 m/s, consistent with the speed of the modulation pattern in the space/time image but much smaller than the wind speed. This shows that this feature is not related to turbulent eddies in the wind traveling at the mean wind speed.

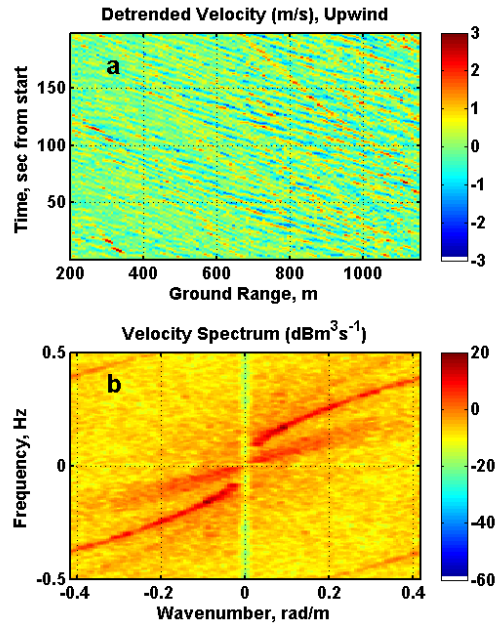


Figure 1. a) Image of horizontal surface velocities obtained from a shipboard, coherent, X-band radar starting at 22:21:21 UTC on August 16, 2008. The polarization was VV. b) The spectrum of this image showing first and possible second-order wave effects. The data have been detrended, as evidenced by the low spectral densities in b at zero wavenumber. The wind velocity was 7.5 m/s from 333°T, the ship velocity was 0.5 m/s to 346°T, and the antenna was looking toward 333°T, upwind. The slope of the linear feature through zero corresponds to a speed of 3.6 m/s

The data presented here can be considered to be nearly one-dimensional spatially for the following reasons. First, ocean wave spectra are well known to have a rather narrow angular spread at wavenumbers near the dominant wave (Donelan et al., 1985). Second, the horizontal component of orbital wave velocity has a cosine fall-off with azimuth angle. Finally, the long, thin cell illuminated by the radar at each range bin discriminates against waves travelling away from the line of sight for all but the longest waves. For instance, this cell is 7.5 m in the range direction and 22 m long in the azimuth direction at a range of 500 m. Using standard equations, the half-width at the 1/e point of the angular resolution of the antennas to a wave 68 m long is shown in Figure 2 as a function of range (Plant et al., 1987). Given this antenna response, we will compare our measured spectra to theoretical, one-dimensional, second-order wave/wave interactions.

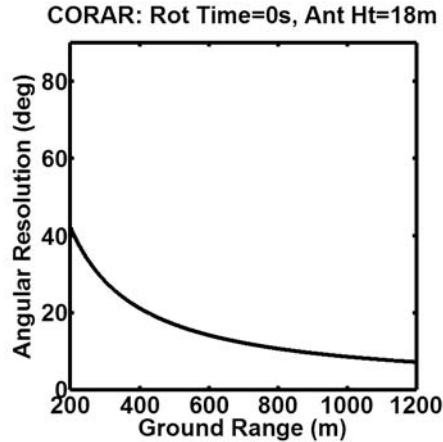


Figure 2. Angular resolution (half-width at 1/e point) of the CORAR parabolic antennas to a surface water wave 68 m long. The antennas are two feet in diameter and 18 meters above the mean surface.

3. Second-Order Water Waves

Perturbation Expansion

To calculate second-order wave effects here, we will follow the work of Weber and Barrick (1977). Creamer et al. (1989) pointed out that Weber and Barrick omitted a second-order term from their equations. However the term that was omitted lies on the first-order dispersion curve and lowers the first-order spectral density by a small amount. Our object here is to interpret the spectral features that do not lie on the first order dispersion curve and here Weber and Barrick's result is correct.

As with all perturbation calculations of surface wave displacements, the calculations begin with the conservation, Navier-Stokes, and surface continuity equations. Following Weber and Barrick, wind and viscous effects are neglected. Then the three fundamental equations are

$$\text{Conservation of mass} \tag{1}$$

$$\text{Navier-Stokes} \tag{2}$$

$$\text{Surface continuity} \tag{3}$$

Here g is gravitational acceleration and the equations are evaluated at the surface since our interest is in the velocity and displacement of the surface. The surface displacement is represented by η in the above equations and ϕ is the velocity potential which is related to the velocity through $\mathbf{v} = \nabla \phi$.

To proceed, η and ϕ are expanded in Fourier series and a perturbation expansion is applied to the Fourier coefficients. Thus,

$$\tag{4}$$

$$\varphi(\mathbf{r}, z, t) = \int \varphi(\mathbf{k}, \omega) e^{[kz + i(\mathbf{k} \cdot \mathbf{r} - \omega t)]} d\mathbf{k} d\omega \quad (5)$$

The variables $\eta(\mathbf{k}, \omega)$, $\varphi(\mathbf{k}, \omega)$, and ω are now expanded to third order. Thus $\eta = \eta_1 + \eta_2 + \eta_3$, $\varphi = \varphi_1 + \varphi_2 + \varphi_3$, and $\omega = \omega_0 + \omega_1 + \omega_2$. Then Weber and Barrick solve Eqs 1-3 to various orders. To first order, they find

$$k\varphi_1(\mathbf{k}, \omega) = -i\omega_0\eta_1(\mathbf{k}, \omega) \quad (6)$$

and

$$-i\omega_0\varphi_1(\mathbf{k}, \omega) = -g\eta_1(\mathbf{k}, \omega) \quad (7)$$

which implies that

$$\mathbf{v}_1 = (\mathbf{a}_k - i\mathbf{a}_z)\omega_0\eta_1(\mathbf{k}, \omega) \quad (8)$$

where \mathbf{a}_k and \mathbf{a}_z are unit vectors in the \mathbf{k} and z directions, respectively, and that

$$(\omega_0^2 - gk)\eta_1(\mathbf{k}, \omega) = 0 \quad (9)$$

If η_1 is not to be identically zero, then the waves must lie on the first-order dispersion relation:

$$\omega_0^2 = gk \quad (10)$$

In the region of ω/k space away from this first order dispersion curve, η_1 is zero but higher-order terms can exist. To avoid confusion, we define the wavenumber and angular frequency in this region to be \mathbf{K} and Ω , as did Weber and Barrick

The second-order solutions are given by Weber and Barrick's Eqs 20 and 21, which may be combined to yield

$$\eta_2(\mathbf{K}, \Omega) = \int A \eta_1(\mathbf{k}, \omega) \eta_1(\mathbf{K} - \mathbf{k}, \Omega - \omega) d\mathbf{k} d\omega \quad (8)$$

where

$$A = \frac{-\Omega_0\omega_0k(\mathbf{a}_k \cdot \mathbf{a}_k) + \omega_0^2 k + 0.5\omega_0 k(\Omega_0 - \omega_0)(1 - \mathbf{a}_k \cdot \mathbf{a}_k)}{gK - \Omega_0^2} \quad (9)$$

and

$$\mathbf{v}_2(\mathbf{K}, \Omega) = (\mathbf{a}_K + i\mathbf{a}_z) \int B \mathbf{v}_1(\mathbf{k}, \omega) \mathbf{v}_1(\mathbf{K} - \mathbf{k}, \Omega - \omega) d\mathbf{k} d\omega \quad (10)$$

where B is

$$B = \frac{gK^2(\mathbf{a}_k \cdot \mathbf{a}_K) - \Omega_0\omega_0K - 0.5\Omega_0(\Omega_0 - \omega_0)K(1 - \mathbf{a}_k \cdot \mathbf{a}_k)}{(\Omega_0 - \omega_0)(gK - \Omega_0^2)} \quad (11)$$

where $\mathbf{a}_{kK} = (\mathbf{K} - \mathbf{k})/|\mathbf{K} - \mathbf{k}|$. Note that, Ω_0^2 and Ω^2 are not equal to gK in the second order equations. However, since $\eta_1(\mathbf{k}, \omega)$ and $\mathbf{v}_1(\mathbf{k}, \omega)$ only exist on the first-order dispersion relation, we must still satisfy $\omega^2 = gk$ and $(\Omega - \omega)^2 = g|\mathbf{K} - \mathbf{k}|$.

Specialization to One Dimension

The above equations are easier to interpret if we specialize to one dimension. Then $\mathbf{a}_k \cdot \mathbf{a}_k = 1$ and

$$\eta(k, \omega) = \eta_1(k, \omega) + \frac{K}{2} \int \eta_1(k, \Omega) \eta_1(K - k, \Omega - \omega) dk d\omega + \eta_3(k, \omega) \quad (12)$$

$$\mathbf{v}(k, \omega) = \mathbf{v}_1(k, \omega) + (\mathbf{a}_k + i\mathbf{a}_z) \frac{K}{2} \int B v_1(k, \omega) v_1(K - k, \Omega - \omega) dk d\omega + \mathbf{v}_3(k, \omega) \quad (13)$$

where

$$B = \frac{1}{\Omega_0 - \omega_0} + \frac{\Omega_0}{gK - \Omega_0^2} \quad (14)$$

The terms $\eta_3(k, \omega)$ and $\mathbf{v}_3(k, \omega)$ represent third-order interaction terms, one example of which is an integral over a product of three first-order terms. When spectra of η and \mathbf{v} are computed, these terms multiplied by η_1 are the same order as the square of η_2 , the convolution terms above. They therefore yield a second-order correction to the spectrum which lies on the first-order dispersion curve. Spectra of the surface displacement, F , and of the horizontal component of surface velocity, V , therefore are given by

$$F(k, \omega) = (1 - k^2 \langle \eta_1^2 \rangle) F_1(k, \omega) + \frac{K^2}{2} \int F_1(k, \omega) F_1(K - k, \Omega - \omega) dk d\omega \quad (15)$$

$$V(k, \omega) = (1 - k^2 \langle \eta_1^2 \rangle) V_1(k, \omega) + \frac{K^2}{2} \int B^2 V_1(k, \omega) V_1(K - k, \Omega - \omega) dk d\omega \quad (16)$$

where orthogonality of the Fourier components has been invoked and the terms involving $\langle \eta_1^2 \rangle$ result from the third-order term given by Creamer et al., 1989. Eq. 16 can now be used to check these results against the radar data.

4. Comparisons with Radar Spectra

If we filter the spectrum shown in Figure 1b so that only the first-order spectrum remains, we can divide it by the factor $(1 - k^2 \langle \eta_1^2 \rangle)$ to get $V_1(k, \omega)$. This can then be used in the convolution of Eq. 16 to obtain the theoretically predicted second-order spectrum, which can then be compared with the second-order part of the spectrum shown in Figure 1. Also, since the current and ship speed were not zero during the measurements, we now have

$$\omega = \pm [\sqrt{gk} + kU] \text{ and } \Omega - \omega = \pm [\sqrt{g|K - k|} + |K - k|U] \quad (17)$$

where U incorporates both the current and ship speed.

Then if we carry out the squaring of B , the convolution in Eq. 16 can be written

$$\begin{aligned}
V_2(K, \Omega) &= \frac{K^2}{2} \int B^2 V_1(k, \omega) V_1(K - k, \Omega - \omega) dk d\omega \\
&= \frac{K^2}{2} \int V_1(k, \omega) \left\{ \frac{V_1(K - k, \Omega - \omega)}{[\sqrt{g|K - k|} + |K - k|U]^2} \right\} dk d\omega \\
&\quad + \frac{K^2 \Omega_0}{gK - \Omega_0^2} \int V_1(k, \omega) \left\{ \frac{V_1(K - k, \Omega - \omega)}{\sqrt{g|K - k|} + |K - k|U} \right\} dk d\omega \\
&\quad + \frac{K^2}{2} \left\{ \frac{\Omega_0}{gK - \Omega_0^2} \right\}^2 \int V_1(k, \omega) V_1(K - k, \Omega - \omega) dk d\omega,
\end{aligned} \tag{18}$$

which can now be evaluated. We note that the spectra computed from the radar data are $V(k, f)$ where $f = \omega/(2\pi)$. Thus the spectrum shown in Figure 1 is related to $V(k, \omega)$ by $V(k, f) = 2\pi V(k, \omega)$. Then,

$$V(k, f) = (1 - k^2 \langle \eta_1^2 \rangle) V_1(k, f) + V_2 \left(K, \frac{\Omega}{2\pi} \right) \tag{19}$$

is the spectrum to be compared with the radar spectrum. Following Weber and Barrick, K and Ω are zero in the region of the wavenumber/frequency plane where $V_1 \neq 0$.

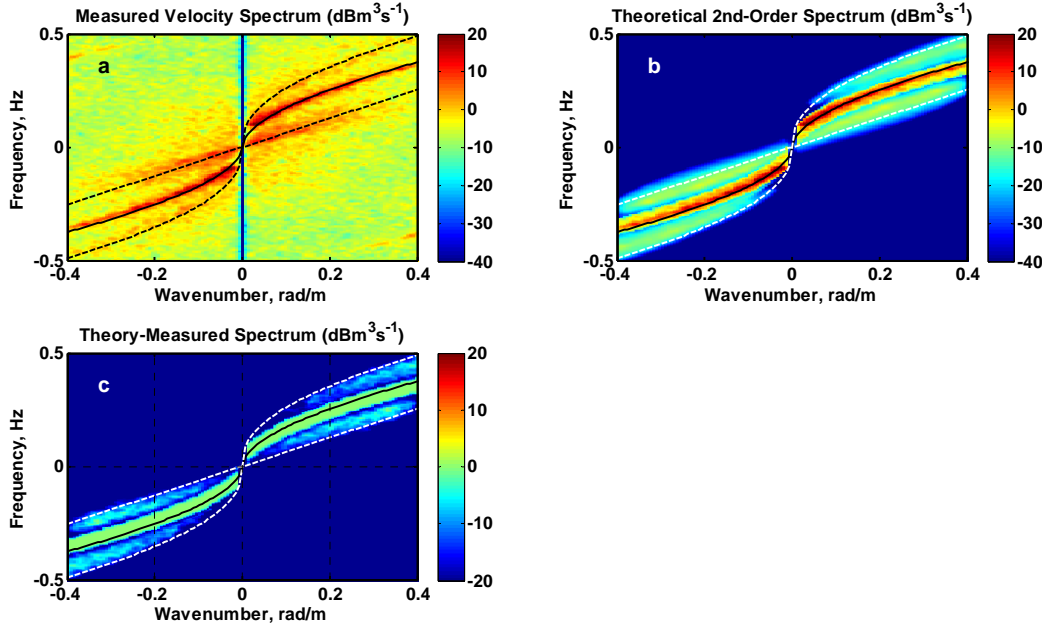


Figure 3. a) The same measured frequency/wavenumber spectrum of scatterer velocity as shown in Figure 1a. b) Second-order spectra computed using the first-order part of a and Eq. 18. c) The ratio (difference on a log scale) of the second-order spectra shown in panels a and b, measured divided by computed. Solid lines show the first-order dispersion relation while dashed lines show the location of the measured features above and below the first-order relation.

Figure 3 shows the result of this operation compared with the measured second-order spectra. The computed spectra are clearly much smaller than the measured ones. Furthermore, the dashed lines in Figure 3b, which are the locations of the center of the measured features, show

that the computed spectra lie closer to the first-order dispersion relation than is measured and that no straight line can be fit through them. Thus it appears that the predicted second-order spectra do not agree with the data.

Another indication that second-order wave-wave interactions do not explain the linear feature is the fact that we observed such a feature when looking nearly crosswind. Figure 4 shows a frequency/wavenumber spectrum from the radar when the antenna was pointing toward the east, nearly perpendicular to the wind, which was from 329°T at 10 m/s. Two features of this spectrum are particularly interesting. First, the remnants of an earlier wind sea are seen propagating toward the east. This swell has a wavelength around 95 m. Also observed in the spectrum is a linear feature similar to those seen looking upwind (Figure 1a) but with smaller slope (lower speed) and propagating to the west, opposite the direction of the swell. Since the look direction is nearly perpendicular to the wind waves, their amplitude is so small that they do not show up along the first order dispersion relation.

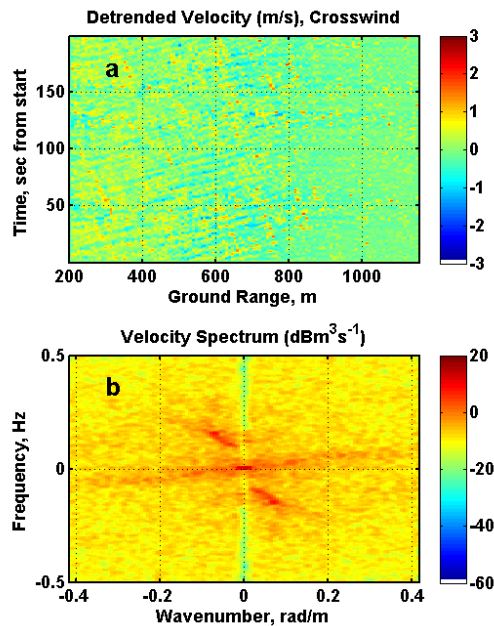


Figure 4. a) Image of horizontal surface velocities obtained from a shipboard, coherent, X-band radar starting at 00:05:57 UTC on August 17, 2008. The polarization was VV. b) The spectrum of this image showing swell travelling away from the radar and a linear feature traveling toward it. The data have been detrended. The wind velocity was 10.0 m/s from 329°T , the ship velocity was 0.6 m/s to 314°T , and the antenna was looking toward 45°T , nearly crosswind. The speed of the linear feature is 1.6 m/s. The peak of the swell spectrum is at $k = 0.0676$ rad/m, or a wavelength of 93 m. Its frequency is 0.134 Hz for a period of 7.5 sec. Thus it was travelling at 12.4 m/s.

We therefore conclude that second-order wave/wave interactions cannot explain the observations either when the antennas are directed nearly upwind or crosswind. Furthermore, since second-order scattering effects will have the same convolution form, they will also be located in the wrong place in the wavenumber/frequency spectrum and also cannot explain the observations.

6. Possible Shadowing Effects

It seems likely that any nonlinear process such as clipping during data processing or shadowing could cause features in the spectrum that lie off the first-order dispersion relation. We took care with our data to make sure that clipping was not an issue. We now consider whether shadowing is the cause of these features. To investigate this we used a data set not taken in the experiment described above but carried out with a very similar radar. These data were collected in 1995 on the US-LTA 138S airship using an X-band Doppler radar operated at HH polarization; the radar and experiment are described in detail by Weissman et al., 2002. The airship flew at an altitude of 240 m so the range of grazing angles for this data set was 25.6° to 53.1° . Shadowing, of course, cannot occur at these grazing angles. For the data presented here, the radar antenna was fixed looking toward the front of the airship (which was moving backward). Space-time images of the detrended line-of-sight velocity measured by the radar, along with corresponding wavenumber-frequency spectra are shown in Figure 5.

Clearly the linear feature is observed in this spectrum even though shadowing does not occur. The speed of the linear feature is about 2.3 m/s in the frame of reference moving with the airship. The speed of the airship was 1.1 m/s in a downwind direction. Thus in the ground frame the linear feature is moving at about 3.5 m/s, similar to that of the data in Figure 1. The wind wave spectral peak is at $k = 0.114$ rad/m, or a wavelength of 55 m. Its frequency is 0.166 Hz for a period of 6 sec. Therefore its velocity is 9.1 m/s in the airship frame of reference or about 10.2 m/s in the ground frame. The expected phase speed of a 55 m long wave is 9.3 m/s so a current component of about 0.9 m/s in the wind direction is indicated.

The fact that the linear feature is present even when shadowing cannot occur clearly indicates that shadowing cannot be the only cause of this feature at lower grazing angles. In fact, Plant and Farquharson (2011) have shown that shadowing is unlikely to occur at all for VV polarization (as used in the shipboard measurements) and is questionable at best for HH polarization on the open ocean. We therefore discount shadowing as a source of the linear feature.

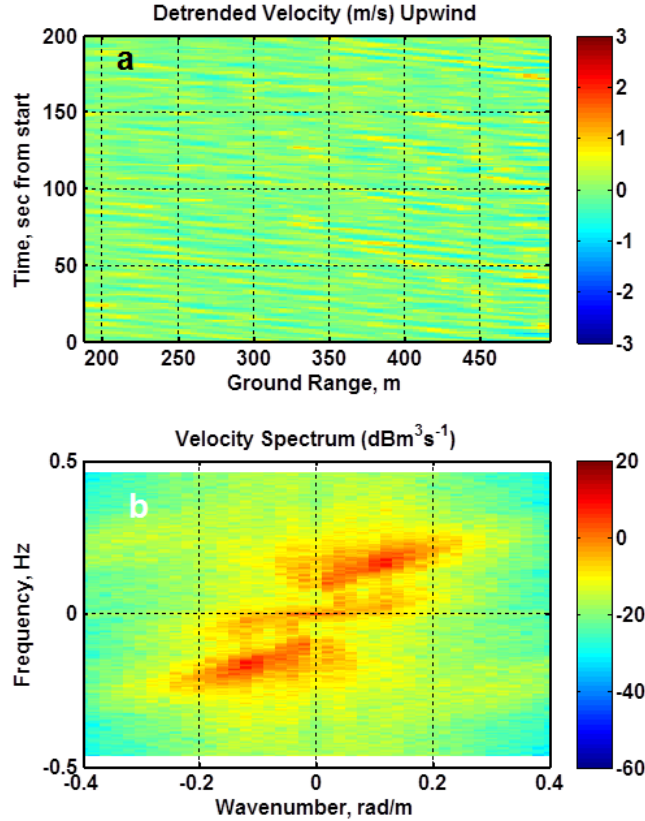


Figure 4. Coherent X-band radar data collected on an airship at grazing angles from 25.6° to 53.1° . a) Image of line-of-sight surface velocities starting at 18:28:39 UTC on September 26, 1995. b) The spectrum of this image. The wind velocity was 12.7 m/s from 176°T , the airship velocity was 1.1 m/s toward 320°T , and the antenna was looking toward 183°T , upwind. The airship heading was toward 176°T so the airship was being blown backward. HH polarization was used. The speed of the linear feature is 2.3 m/s in the airship's frame of reference or 3.5 m/s in ground coordinates.

5. Interference Patterns

Since neither wind turbulent eddies moving over the ocean surface at the mean wind speed nor second-order interactions can account for the observed features of the images and spectra, and shadowing effects are questionable at best, especially at VV polarization, we must search elsewhere for the cause of the features observed in our VV polarized data. Wind waves in the area of our measurements coexisted with swell coming from the west. We therefore consider a scenario where the wind waves and swell interfere and produce breaking near the points where the surface slope is particularly large.

We simulate the surface displacements on the sea surface by first converting the ocean wave variance spectra of Donelan et al. (1985) from frequency to wavenumber as done by Plant (2002) to get $F(k, \varphi)$. The wavenumber range was limited to 0.0184 to 0.362 rad/m in steps $dk = 0.0061$ rad/m. The azimuth angle φ from the wind direction went from $-\pi$ to π in steps $d\varphi = 0.0982$ rad. Wind-wave amplitudes were computed from

$$A(\mathbf{k}, \varphi) = 7\Gamma_1 * \sqrt{F(\mathbf{k}, \varphi - \varphi_o)kdkd\varphi}$$

where φ_o is the angle of the wind with respect to north, Γ_1 is a Gaussian random variable with mean equal to 1 and variance equal to 0.2 and the factor of 7 was required to make wave amplitudes correspond to those observed. We took the wind speed to be 7.5 m/s as in the data of Figure 1 and the fetch to be 500 km, which gave a peak wavelength of 68 m in good agreement with that observed in the data. Then two-dimensional wind-wave surfaces were generated for 128 times separated by one second from the equations

$$\gamma_i(\mathbf{x}, t_i) = \sum_j A(\mathbf{k}_j) \cos(\mathbf{k}_j \cdot \mathbf{x} - \omega t_i + \varphi_r(\mathbf{k}_j))$$

where φ_r is a random variable uniformly distributed between $-\pi$ and π . In a similar manner, vertical and horizontal velocities of the wave field were computed from the equations

$$\begin{aligned} u_i(\mathbf{x}, t) &= \sum_j \omega(\mathbf{k}_j) A(\mathbf{k}_j) \cos(\mathbf{k}_j \cdot \mathbf{x} - \omega t_i + \varphi_r(\mathbf{k}_j)) \\ v_i(\mathbf{x}, t) &= \sum_j \omega(\mathbf{k}_j) A(\mathbf{k}_j) \sin(\mathbf{k}_j \cdot \mathbf{x} - \omega t_i + \varphi_r(\mathbf{k}_j)) \end{aligned}$$

and the line-of-sight components in the north and east directions were computed:

$$\begin{aligned} V_{los}^i &= \cos\varphi \sin\theta u_i(\mathbf{x}, t) + \cos\theta v_i(\mathbf{x}, t) \\ U_{los}^i &= \sin\varphi \sin\theta u_i(\mathbf{x}, t) + \cos\theta v_i(\mathbf{x}, t) \end{aligned}$$

The swell amplitude was taken to be a narrow-band, Gaussian, $2dk$ wide distributed around the swell wavelength. It was considered to be unidirectional and its amplitude was multiplied by a Gaussian random variable with mean equal to 1 and variance equal to 0.1. Then two-dimensional swell surfaces for the amplitude, A_{si} , and two line-of-sight velocities, U_s^i and V_s^i , were generated for 128 times separated by one second.

Finally complete surfaces were generated by adding wind-wave and swell components together:

$$\begin{aligned} \gamma_{tot}^i &= \gamma_i + \gamma_{si} \\ V_{tot}^i &= V_{los}^i + V_s^i \\ U_{tot}^i &= U_{los}^i + U_s^i \end{aligned}$$

From each γ_{tot}^i , the derivatives in the north and east directions were computed and pixels where this slope was below $-\tan 13^\circ$ were found. We then added $3.5\Gamma_2$ to V_{tot}^i or U_{tot}^i if the north or east slope exceeded this threshold. Here Γ_2 is a Gaussian random variable with mean equal to 1 and variance equal to 1. In this manner, we attempted to account for breaking of short gravity waves where the magnitude of the slope of the larger scale surface on their front faces was large.

Figure 7 shows the results of these simulations. We let the dominant wind wave come from 330 degT, the wind speed be 7.5 m/s, the swell come from 280 degT, and the incidence angle be 88° . Figure 7a shows the space-time image for a cut through the image stack in the northerly direction with the antenna nearly looking into the wind waves. The cut through the image was 352 m wide and the spatial variation in the look direction was an average over this perpendicular distance. The figure clearly shows the dominant wind waves with a modulation pattern superimposed on them. Pattern maxima move at about 3.2 m/s, very similar to the speeds of the

modulation pattern shown in the actual data of Figure 1. Figure 7c shows the wavenumber-frequency spectrum of the space-time image of Figure 1a. The features of interest may be observed above and below the first-order dispersion relation. The low-frequency feature is linear with a slope indicating the same speed of 3.2 m/s as the modulation pattern in the space-time image. Furthermore, the intensity of this feature relative to the energy on the first-order dispersion relation is about the same as that shown in Figure 1b for the data. Figure 7b shows a cut through the image stack in the easterly direction with the antenna looking east but with the wind from 30 degT. Again wave features are visible, this time from the swell, as evidenced by the direction of propagation. A modulation pattern is also seen in Figure 7b that is steeper and less intense than the pattern in Figure 7a. Its slope yields a speed of 1.5 m/s. Figure 7d shows the wavenumber-frequency spectrum of the data of Figure 7b. The swell is now clearly seen on the first-order dispersion relation propagating away from the antenna but no trace of the wind-wave system is seen. The modulation pattern moves toward the antenna at a speed of 1.5 m/s. This wavenumber-frequency spectrum is very similar to that shown in Figure 4b, which was calculated from the data.

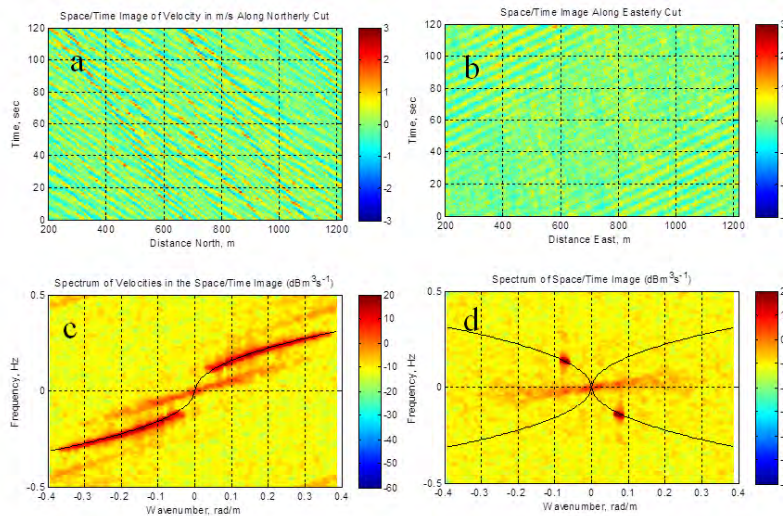


Figure 7. Results of simulating line-of-sight velocities observed by Doppler radars. a) Space-time image of a cut through the image stack in the northerly direction. Antenna looks north, wind from 330 degT, swell from 280 degT. The speed of the modulation pattern is 3.2 m/s. b) Space-time image of a cut through the image stack in the easterly direction. Antenna looks east, wind from 30 degT, swell from 280 degT. The speed of the modulation pattern is 1.5 m/s. c) Wavenumber-frequency spectrum of the space-time image of a). The slope of the linear, low-frequency feature indicates a speed of 3.2 m/s. d) Wavenumber-frequency spectrum of the space-time image of b). The slope of the low-frequency linear feature indicates a speed of 1.5 m/s and a propagation direction opposite that of the swell.

We have investigated the cause of the modulation patterns observed in the space-time images and the corresponding low-frequency features in the wavenumber-frequency spectrum. If the wind direction is changed to 330 degT, the slope of the linear feature changes sign. If no wave breaking is added to the velocity images, the modulation patterns are still observed in the space-time images due to the interference of the long waves. As expected, however, no linear feature is seen in the wavenumber-frequency spectrum because no nonlinear interactions are taking place.

If the swell amplitude is set to zero, both the modulation pattern and the low-frequency linear feature are still observed, although at a slightly reduced intensity. All of this leads us to conclude that the most likely cause of features observed in wavenumber-frequency spectra of ocean image stacks at locations other than those of the first-order dispersion relation is the breaking of waves caused by interference of wind waves either with themselves or with swell. Thus these features should be nearly universal at sufficiently high wind speeds. In the next section we show why we believe that short gravity waves rather than the wind waves or swell are the breaking waves.

Doppler Velocities

To attempt to determine whether Doppler shifts corresponding to breaking dominant wind waves occurred on the ocean, we looked at recorded Doppler spectra taken with the antenna looking upwind and downwind. Stansell and MacFarlane (2002) have recently shown in laboratory experiments that water parcel velocities produced by breaking waves are somewhat smaller than the linear phase speed of the breaking waves. They found mean parcel velocities to be between 0.81 and 0.95 times the phase speed, depending on the type of breaking. Thus, if dominant ocean waves were indeed the breaking waves, they would produce Doppler shifts corresponding to velocities that were within 80% of the dominant wave phase speed.

During our data collection we computed and stored complete Doppler spectra at 14 range bins for each of the 1000 scans that were collected into individual files. For all of these spectra, we determined the highest frequency at which the spectral density of the Doppler spectra exceeded the noise level by 10 dB or more. Our Nyquist frequency corresponded to a velocity of 12.5 m/s so we could unambiguously identify scatterers travelling at line-of-sight velocities up to this value. Figure 8 shows histograms of the maximum horizontal velocities obtained from our maximum line-of-sight velocities for each of the 14000 spectra collected looking upwind and downwind with our VV polarized antennas. The largest horizontal velocity observed was 6 m/s while only 0.5% of the spectra showed horizontal velocities above 5 m/s. Thus the fastest scatterer would have been produced by a breaking wave whose linear phase speed was less than 7.5 m/s. The frequency of the peak of the surface wave spectrum during the measurements was 0.14 Hz, which corresponds to a surface wave whose linear phase speed is 11.7 m/s. Furthermore, note in Figure 8 that the peak of the upwind histogram agrees well with the speed of the linear feature in the wavenumber-frequency spectrum shown in Figures 1b and 7c. Thus the waves that are breaking cannot be the dominant waves but must be shorter surface gravity waves that are steepened by currents set up by the interference patterns within the wind wave system.

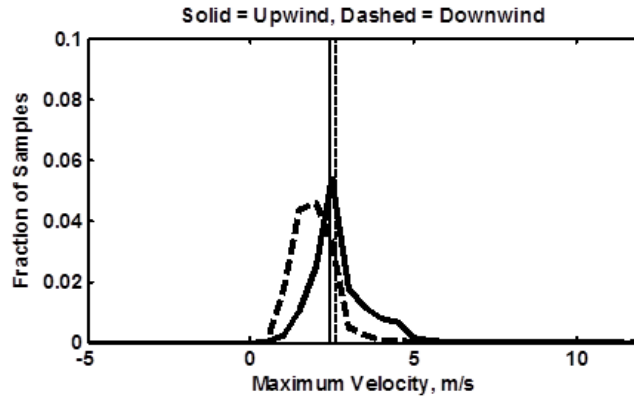


Figure 8. Histogram of the velocities of scatterers that were the fastest scatterers in Doppler spectra observed with antennas looking upwind or downwind. The solid line is the histogram looking upwind while the dashed line is the histogram looking downwind. Solid and dashed vertical lines show the speeds of linear features observed in wavenumber frequency spectra of space-time images from the radar. The wind speed was 9.8 m/s. The vertical lines show the speeds of the linear features in figures 1b and 7c.

Conclusions

We have shown that neither turbulent eddies in the wind traveling at the mean wind speed nor second-order interactions due to either hydrodynamic or electromagnetic nonlinearities can cause the linear, low-frequency feature found in wavenumber-frequency spectra of remotely sensed ocean images. Shadowing, if it exists, can cause such features but cannot be the only cause since the feature exists in spectra obtained at high grazing angles. In any case, evidence that shadowing is the cause is questionable. On the other hand, simulations of wave surfaces that include wave breaking at maxima of the wind-wave interference pattern produce both the linear, low-frequency feature and the higher-frequency features often observed above the first-order dispersion curve. Furthermore, such interference-induced wave breaking can also account for the linear feature observed in our measured wavenumber-frequency spectra that travels in the opposite direction to the swell. Doppler spectra recorded by our X-band Doppler radar showed no evidence of scatterers travelling faster than 6 m/s even though the dominant wave linear phase speed was 11.7 m/s. Our conclusion is that the most common origin of features seen off the first-order dispersion relation in wavenumber-frequency spectra of remotely sensed space-time images is the breaking of short gravity waves on the surface due to large current gradients or slopes caused by the interference of dominant surface waves. This conclusion agrees well with that of Irisov and Voronovich (2011) who found in a numerical study that short gravity waves on the ocean break due to local maxima of current convergence or steepness.

Acknowledgments

This study was made possible by several grants originating in the Office of Naval Research (ONR) including N00014-10-10318, F012919, and APS-11-12. Grant # A100747 from the Bureau of Ocean Energy Management, Regulation and Enforcement (BOEMRE) enabled the study to be completed.

References

- Barrick D.E., and Weber B.L., On the nonlinear theory for gravity waves on the ocean's surface. Part 2. Interpretation and Applications. *J. Phys. Oceanog.* 7, 11-22, 1977.
- Donelan, M. A., J. Hamilton, and W. H. Hui, Directional spectra of wind generated waves, *Philos. Trans. R. Soc. London, Ser. A*, 315, 509–562, 1985.
- Dugan, J.P., C.C. Piotrowski, and J. Z. Williams, Water depth and surface current retrievals from airborne optical measurements of surface gravity wave dispersion, *J. Geophys. Res.*, 106(C8), 16903-16915, 2001.
- Dugan, J.P., and C.C. Piotrowski, Surface current measurements using airborne visible image time series, *Rem. Sens. Env.*, 84, 309–319, 2003.
- Hasselmann, K., On the nonlinear energy transfer in a gravity-wave field spectrum. Part 1. General theory. *J. Fluid Mech.* 12, 481-500, 1962.
- Irisov, V., and A. Voronovich, Numerical simulation of wave breaking, *J. Phys. Ocean.*, 41, 346-364, 2011.
- Frasier, S.J., and R.E. Mcintosh, Observed wavenumber-frequency properties of microwave backscatter from the ocean surface at near-grazing angles, *J. Geophys. Res.*, 101(C8), 18391-18407, 1996.
- Longuet-Higgins, M.S., Resonant interactions between two trains of gravity waves, *J. Fluid Mech.*, 12m 321-332, 1962.
- Phillips, O.M ., On the dynamics of unsteady gravity waves of finite amplitudes. Part 1. The elementary interactions. *J. Fluid Mech.* 9, 193-217, 1960.
- Plant, W.J., W.C. Keller, A.B. Reeves, E. Uliana, and J.W. Johnson, Airborne microwave Doppler measurement of ocean wave directional spectra, *Intl. J. Remote Sensing*, 8 (C3), p. 315-300, 1987.
- Plant, W.J., W.C. Keller, V. Hesany, and K. Hayes, Measurements of the marine boundary layer from an airship, *J. Atmos. Ocean. Tech.*, 15, 1433-1458, 1998.
- Plant, W.J., A stochastic, multiscale model of microwave backscatter from the ocean, *J. Geophys. Res.*, 107(C9), 3120, doi:10.1029/2001JC000909, 2002.
- Plant, W.J., and G. Farquharson, Wave shadowing and modulation of microwave backscatter from the ocean, in preparation, 2011.

Rino, C.L., E. Eckert, A. Siegel, T. Webster, A. O Chadlick, M. Rankin, and J. Davis, X-Band low-grazing-angle ocean backscatter obtained during LOGAN 1993, *IEEE J. Ocean. Eng.*, 22(1), 18-26, 1997.

Smith, M.J., E. M. Poulter, and J. A. McGregor, Doppler radar measurements of and breaking waves wave groups, *J. Geophys. Res.*, 101(C6),14269-14282, 1996.

Stansell, P., and C. MacFarlane, Experimental investigation of wave breaking criteria based on wave phase speeds, *J. Phys. Ocean.*, 32, 1269-1283, 2002.

Stevens, C.L., E. M. Poulter, M.J. Smith, and J. A. McGregor, Nonlinear Features in Wave-Resolving Microwave Radar Observations of Ocean Waves, *IEEE J. Ocean. Eng.*, 24(4), 470-480, 1999.

Weber, B.L., and D.E. Barrick, On the nonlinear theory for gravity waves on the ocean's surface. Part 1. Derivations. *J. Phys. Oceanog.* 7, 3-10, 1977.

Weissman, D.E., W.J. Plant, W.C. Keller, and V.G. Irisov, Comparison of scatterometer and radiometer wind vector measurements, *J. Atmos. Ocean. Tech.*, 19, 100-113, 2002.